Recording media dynamics using a multi-timescale micromagnetic model with atomistic parameterisation

Samuel Ewan Rannala

Doctor of Philosophy

University of York
Physics

May 2022

Abstract

The current state of the art technology for ultra-high density magnetic storage is based on heat assisted magnetic recording (HAMR). As the demand for greater storage density increases the optimisation and improvement of HAMR technologies is crucial. The nature of HAMR requires models capable of correctly describing the magnetisation over temperatures up to and exceeding the material's Curie point. Additionally, the ability to study long term behaviours, such as data storage stability, requires that these models are capable of very large timesteps ranging from seconds to years. An open-source code called MARS incorporating three key solvers has been developed. MARS is capable of modelling systems over all required temperatures via a Landau-Lifshitz-Bloch (LLB) solver as well as over long time periods via a kinetic Monte Carlo (kMC) solver. The source code is available at **https://bitbucket.org/EwanRannala/mars**.

Using MARS, investigations into numerous key aspects of HAMR systems have been performed: the presence of Curie point distributions, which limit the effectiveness of HAMR performance by inducing variations in the obtained bit positions; the influence of adjacent track erasure and temporal decay on HAMR performance; and the presence of decreasing ferromagnetic resonance (FMR) linewidth at temperatures close to the Curie point which has been attributed to a potential decrease in the system's damping which can influence HAMR performance significantly. The first investigation has resulted in the development of a semi-analytical model capable of extracting the Curie point distribution from experimental thermoremanence measurements. The second has revealed that adjacent track erasure is significant compared to temporal decay for a system with an energy barrier of $80\,k_BT$ with no additional signal degradation when adjacent track writes occur after long periods of data storage. The final investigation has shown that the linewidth reduction is due to in-homogeneous line broadening and that the system damping increases as temperatures approach the Curie point.

Table of contents

List of tables

List of figures

Acknowledgements

I would like to express my sincere gratitude to Professor Roy Chantrell for his constant help and support. Thank you for the numerous insightful discussions and the great number of opportunities you have provided me.

My sincere thanks to Professors Jessada Chureemart and Phanwadee Chureemart for welcoming me into their research group (MINT) and enabling me to visit Thailand numerous times as well as providing me with invaluable support in determining my career desires going forward.

I would like to thank Ganping Ju and Pin-Wei Huang from Seagate Media Research, Fremont for providing experimental data and assistance.

I would like to thank Sergiu Ruta and Andrea Meo for their continuous assistance and advice along with my past and present colleagues Mara, Tim, Paul, Sam, Razvan, Roberto, Daniel and Christina for the many useful discussions and enjoyable moments they helped create. I am grateful to the members of the MINT group for being extremely welcoming and also collaborating with me. My time spent with the group has provided me with many great friendships and I am grateful to Wasan, Natty, Tong, Pet and Wut for their support and friendship.

Finally, I would like to express sincere gratitude to my parents, Gale and Erwin and my brother Magnus who have all provided me with exceptional support throughout my entire academic career. I would not have been able to progress to this stage without their constant love, help and support.

Declaration

I hereby declare that except where specific reference is made to the work of others, the contents of this dissertation are original and have not been submitted in whole or in part for consideration for any other degree or qualification in this, or any other university. The majority of this thesis has been presented at various conferences by the author, some chapters being based on the following publications:

- A. Meo, W. Pantasri, W. Daeng-am, **S. E. Rannala**, S. I. Ruta, R. W. Chantrell, P. Chureemart, J. Chureemart (2020). Magnetization dynamics of granular head-assisted magnetic recording media by means of a multiscale model Physical Review B, 102, 174419 10.1103/PhysRevB.102.174419
- **S. E. Rannala**, A. Meo, S. Ruta, W. Pantasri, R. W. Chantrell, P. Chureemart, J. Chureemart (2022). Models of Advance Recording Systems: A Multi-timescale Micromagnetic code for granular thin film magnetic recording systems. arXiv preprint arXiv:2205.05263 (in final review for Computer Physics Communications, response submitted.)

1

Introduction

1.1 History of magnetic recording media

Magnetic recording technology dates back to the 19th century when Valdemar Poulsen developed the telegraphone in 1898, a device capable of registering human speech by alternating the magnetisation of a steel wire [1]. The principle of magnetic recording is simple and relies on two principles: 1) Magnets produce strong magnetic fields at the poles which can be used to store information. 2) The polarity of the magnets can be changed by applying external magnetic fields, providing the ability to write information. Both these principles remain as true today as they did at the start of magnetic recording technology.

After numerous technological advancements and the increasing necessity to store, process and send data, driven significantly by the Second World War, magnetic tape was developed. Magnetic tape works by coating a film with magnetic particles (commonly iron oxide particles) and then applying electrical signals through a recording head to magnetise the iron oxide and record the desired information. The data is then read by passing the tape over a playback head with the magnetisation of the tape inducing electrical signals in the head enabling output of the recorded information. The initial method of using magnetic tape consisted of storing it on reels and transferring the tape from one reel to another with the data written or read by a recording head placed between the two reels. Later in the 1960s, magnetic tape become common in the home due to audio cassettes. These cassettes were later followed by video cassettes in the 1970s. Cassettes work in a similar manner to reels with the tape stored on one end of the cassette and transferred to the other end during recording or playback. Magnetic tape is still in use today for archival or cold-storage purposes in businesses. In 2014 Sony and IBM announced the development of a magnetic tape capable of storing $148\,\mathrm{GB}/\mathrm{in}^2$ enabling capacities of up to 185 TB per cartridge [2]. Furthermore the Information Storage Industry Consortium predicts magnetic tape will surpass $200\,\mathrm{GB}/\mathrm{in}^2$ by

2028 [3]. The benefits of magnetic tape are its relatively low cost per GB, longevity (when appropriately stored), high reliability and security. However, the inability to perform fast random access to the data makes magnetic tape applications in personal computing and home media delivery unsuitable for modern day requirements. As such magnetic tape has become uncommon on standard day-to-day usage replaced by much more dense magnetic hard disk drives and more recently flash storage.

In 1956 the first commercial magnetic hard drive was the IBM 350 disk storage unit developed by IBM [4]; consisting of fifty 53 cm disks with a total storage capacity of 3.75 MB. The shift away from a continuous storage medium to a rotating platter enabled random access to the stored data. This behaviour was crucial in order to fulfil the requirements of real time accounting for businesses. The hard disc drive design consists of multiple platters containing a magnetic layer placed on a spindle with a read head and write head placed on an articulating arm enabling access to all sections of the platters. This initial technology utilised longitudinal magnetic recording whereby the magnetisation is aligned parallel to the platter, Fig. 1.1 illustrates the longitudinal magnetic recording setup.

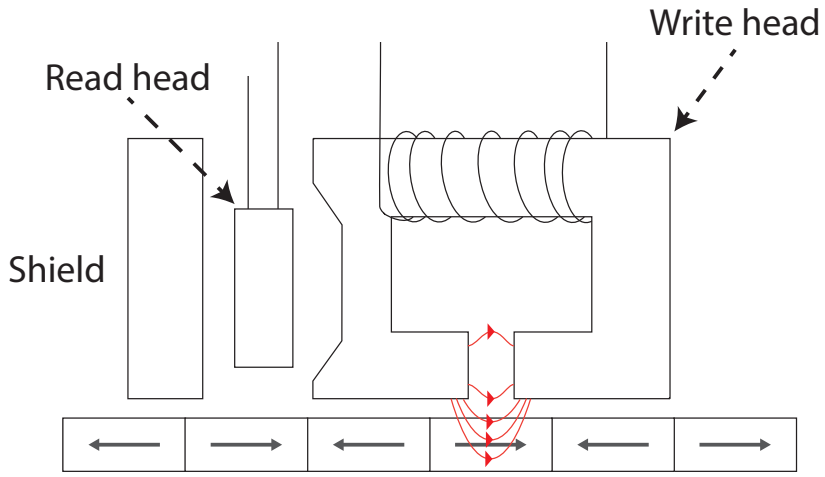

Fig. 1.1 Illustration of longitudinal magnetic recording. The solid arrows represent the magnetisation of the bits within the storage layer.

In 1977 S. Iwasaki and Y. Nakamura proposed perpendicular magnetic recording (PMR) [5]. By rotating the direction of the magnetisation the bits could be more closely packed enabling greater areal densities than those possible by longitudinal magnetic recording. However, the development of such devices was not a trivial task and as such it took almost three decades for the first perpendicular magnetic recording device to come to market. By shifting to perpendicular magnetic recording bit sizes were able to decrease below the superparamagnetic limit of longitudinal recording media. The superparamagnetic limit indicates the point at which the grains become small enough that thermal fluctuations are

sufficient to induce magnetisation reversal before the desired storage time has elapsed causing data loss. Figure 1.2 illustrates perpendicular magnetic recording, a significant additional feature of PMR devices is the presence of the soft magnetic underlayer. The write head produces a highly concentrated field in the gap between the pole and the underlayer, placing the storage layer in this gap enables the writing of the bits. Throughout the last almost twenty years numerous developments and advancements have been made in order to improve the areal density of PMR to keep up with the ever-growing demand for greater data storage both for personal and enterprise use. However, in recent years the ability to increase the areal density of PMR devices has reached its limit dictated by the so-called magnetic recording trilemma.

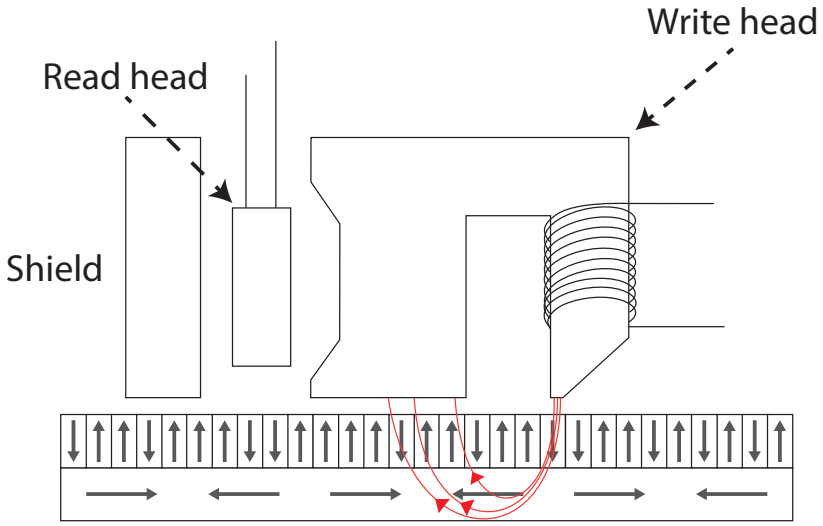

Fig. 1.2 Illustration of perpendicular magnetic recording. The data is stored in the top layer with the magnetisation aligned perpendicular to the recording medium's surface. Below is the soft magnetic underlayer.

1.2 Magnetic recording trilemma

The magnetic recording trilemma describes the interplay between three fundamental limitations of magnetic recording media. This trilemma is illustrated in Fig. 1.3. In order to reduce the areal density two methods can be used: reduce the number of grains within a bit or reduce the size of the grains. The first method leads to Bit Patterned Media (BPM) where a bit consists of just a single grain. If one chooses to instead decrease the size of the grains we remain in the realm of perpendicular magnetic recording however we must now face the difficulties associated with reduced thermal stability. The reduced grain sizes result in reduced energy

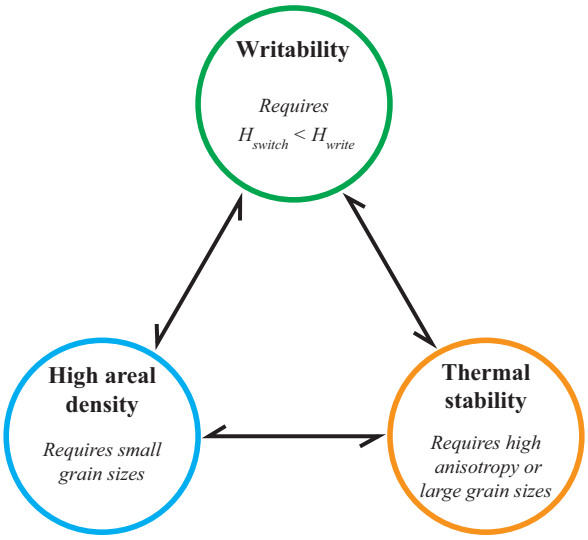

Fig. 1.3 Illustration of the magnetic recording trilemma.

barriers described by the ratio $\frac{KV}{k_B T}$, where K is the anisotropy energy density, V is the volume of the grain, k_B is the Boltzmann constant and T is the temperature. Smaller energy barriers lead to lower thermal stability. For long term data storage this ratio needs to be kept to a minimum of around 60 [6, 7]. In order to maintain a sufficient thermal stability the anisotropy of the recording medium, K, can be increased. However, higher anisotropy grains require greater writing fields to enable switching. The typical write field strength is 10 kOe which is insufficient to switch high anisotropy materials such as FePt, which has a switching field as high as 50 kOe [7]. There are two available methods to overcome this write limitation: Exchange coupled composite (ECC) media, whereby the exchange spring mechanism is used to aid the magnetic reversal mechanism and heat assisted magnetic recording (HAMR) where the coercivity of the recording medium is reduced by the application of heat.

1.3 Heat assisted magnetic recording

Heat assisted magnetic recording is the current state of the art magnetic recording technology. HAMR is a key part of the push to continuously improve data storage capacities of magnetic recording media as is evident in the Advanced Storage Technology Consortium (ASTC) technology roadmap shown in Fig. 1.4 [8]. Heat assisted magnetic recording overcomes the grain size limit by utilising high coercivity materials such as FePt providing thermal stability at much smaller grain sizes. In order to write to such a material the coercivity must be reduced and this is achieved by heating a region of the recording medium close to or above its Curie point before applying the write field. This heating element must be incorporated

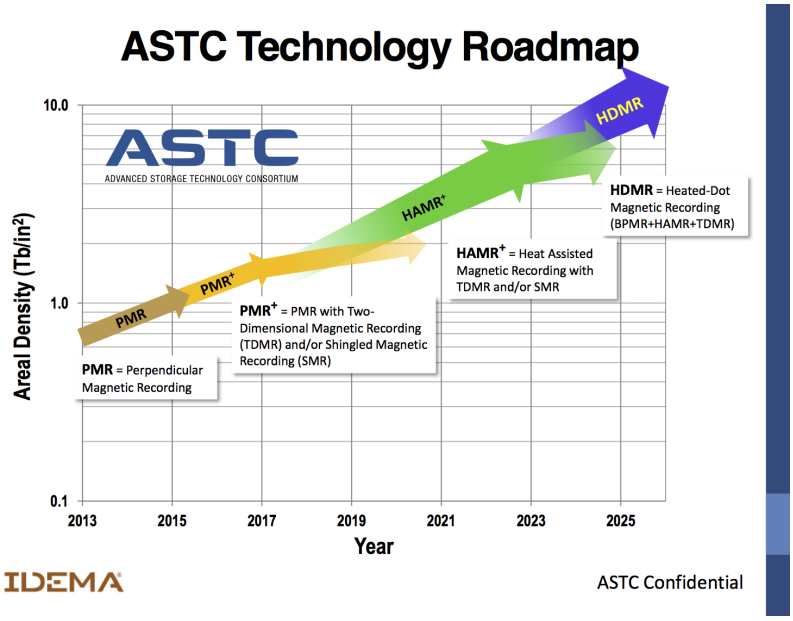

Fig. 1.4 Technology roadmap published by the ASTC. [8]

into the extremely small write head and must also be capable of producing heat spots near to and below the diffraction limit. If the heated spot is too large there will be significant damage to the adjacent tracks due to the overlap of the heated spot. This issue has been overcome through the use of a near-field transducer (NFT). A near field transducer is a type of plasmonic nanoscale antenna, which in HAMR devices is typically made of gold [9]. When the NFT is driven at resonance the surface charge oscillates producing an electric field which couples energy into the recording medium. In order to provide energy to the NFT a laser and waveguide are used. One design places a 'lollipop' transducer at the focus of a planar solid immersion mirror. A plasmonic metal is placed below the recording layer and acts as both a heat sink and an image plane for the electric field as is illustrated in Fig. 1.5. The requirement of the heating element in the HAMR recording head significantly increases the complexity of the device. Figure 1.6 shows a schematic of a HAMR recording head, which includes the read and write poles as in the PMR head along with the NFT, waveguide and laser.

1.4 Complexities of HAMR systems

The process of heating the recording media in order to reduce the coercivity and enable writing creates additional complexity in the media design. Variations in the temperature dependencies between grains can result in the reduction of the performance of HAMR

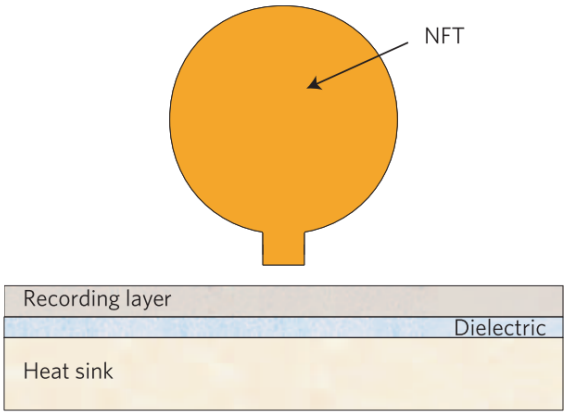

Fig. 1.5 Illustration of the lollipop NFT showing its position with respect to the recording media along with the additional required recording media layers. [10]

devices. As a result, recording media must be suitable across the entire operating system temperature range, from the slightly warmer than room temperature, drive interior up to the high temperature region under the NFT. At the Curie point a ferromagnetic object loses its order and becomes paramagnetic, thus many of the temperature dependent material properties are dependent on the Curie point of the grain. A variation in the Curie point will result in a variation in the material property's temperature dependence. As an example these variations can result in the anisotropy of some grains becoming too low causing instability in the write process for those grains. Additionally it has been shown that the Curie point of granular media is dependent on the grain size, thus the presence of grain size distributions inevitably leads to Curie point distributions. In general, for HAMR devices the fabrication of the recording media, determination of parameter distributions, control of parameter variations and understanding of the inter-dependencies of such variations is key to the development of high performance devices.

1.5 Modelling magnetic recording systems

Magnetism cannot be described via a single length and time scale as magnetism itself in a quantum phenomenon and yet quantities such as magnetisation are macroscopic. The properties of magnetic materials are influenced by atomistic defects, such as vacancies and lattice structures. Additionally macroscopic properties also influence the magnetic properties, one such example is that the grain size has been shown to influence the Curie point [11]. In order to ensure reliable and accurate descriptions of magnetic recording devices a multiscale approach is required. Atomistic spin dynamics are used to parameterise the materials used in the recording medium. This atomistic parameterisation enables a highly accurate description

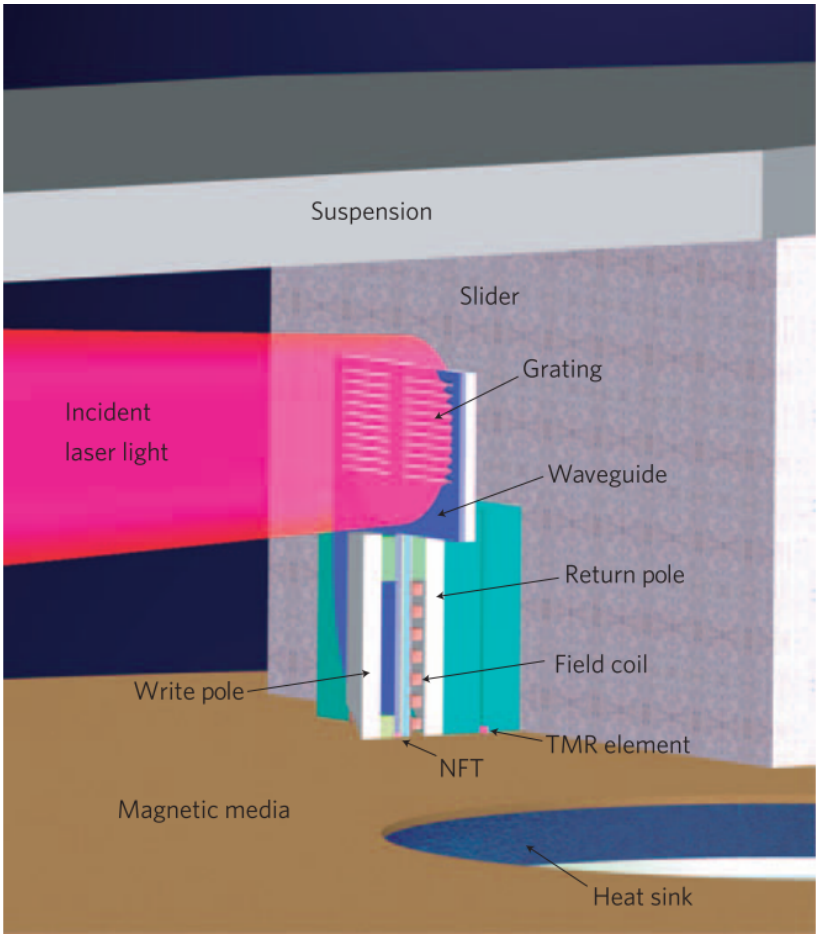

Fig. 1.6 HAMR recording head schematic consisting of a waveguide, lollipop NFT, write pole, tunnel magnetoresistance read sensor. [10]

of the material parameters over the desired temperature scales. Furthermore the complexity of the micromagnetic modelling can be reduced by enabling granular simulations with features such as the segregant accounted for within the atomistic parameterisation.

The complexity of atomistic simulations results in them being computationally expensive and as such it is not possible to simulate the large systems used in recording media investigations via atomistic spin dynamics alone. Micromagnetic modelling enables access to these larger length scales but the time scales for these simulations are still limited to the microsecond range. However, these time scales can be extended via energy minimisation techniques. Using these techniques the timescales can be expanded to thousands of years.

Recording media is a prime example of a system which requires a multiscale approach. As previously explained the materials used for the recording media require atomistic parameterisation in order to produce accurate descriptions of their behaviours, especially when temperature dependencies are important as is the case with HAMR. However, the

length scales used for data storage quickly exceed those possible via atomistic simulation, for example with an average bit length of around 20 nm [12] the system reaches micrometres in length in only 50 bits. Thus, micromagnetic simulations are a requirement to provide useful simulations of the numerous aspects of magnetic recording media design. The long timescale nature of data storage is also an extremely important aspect of magnetic recording devices, where typically a ten year lifespan is expected [6, 13]. As a result, in order to comprehensively cover recording media devices through simulation both short and long timescales must be accounted for providing further support for the use of micromagnetics as a key tool for these systems.

1.6 Accessibility of magnetic models

As the complexity of magnetic recording media devices increases so too does the complexity of the models required to simulate them. Prior to HAMR the relatively simple Landau-Lifshitz-Gilbert (LLG) equation could be used to model most aspects of the recording process. The introduction of temperature variations to the fundamental working processes of the device require more complex models such as a the Landau-Lifshitz-Bloch (LLB). This increasing complexity creates a greater barrier for entry for one to start modelling and investigating magnetic recording systems through simulation. Additionally due to the multiscale nature of magnetism it is crucial to investigate system behaviours through experimental and simulation as together one can access all of the necessary length and time scales.

In order to reduce the entry requirements for magnetic simulation easy to access simulation packages are a necessity. Such packages enable researchers from a wide range of backgrounds to access and make use of computational modelling and simulation to further their research. While it is not impossible for a researcher to develop and implement a software package from scratch when required it is cost and time prohibitive in many cases. Thus having access to an open-source easily adjustable software package greatly decreases the time required for researchers to be able to perform simulations useful to their area of research. This in turn should greatly improve the progress of research in both theoretical and experimental endeavours.

1.7 Thesis outline

The thesis focuses on the development of an open source multi-timescale micromagnetic code called Models of advanced recording systems (MARS), written using C++, for applications

in simulations of magnetic recording systems. This code has the functionality to perform both short and long timescale simulations in order to more completely cover the scenarios important to recording media investigations and simulations. Additionally the developed code is then used to investigate numerous important aspects of HAMR systems to aid in the improvement of the technology. While the simulations presented in this work focus on HAMR the developed code has been designed such that it can be used for simulation of any granular thin film system. Furthermore the open source nature of the code allows for future adjustments and improvements to keep MARS up to date with cutting edge magnetic recording media needs and requirements.

Chapter 2 describes the background for each of the three key micromagnetic solvers which provide the key functionality of the MARS code. The chapter starts by providing background context to the field of micromagnetic modelling from its conception up to the modern day standards. Following this the Gibbs free energy for a ferromagnetic granular system is derived providing the required information to model the desired ferromagnetic systems. The LLG micromagnetic solver is then introduced starting from its precursor the Landau-Lifshitz (LL) equation of motion. The limits of the LLG are then discussed and the more versatile LLB is introduced. Finally the long timescale solver, the kinetic Monte Carlo (kMC) is detailed starting from its basis using the Stoner-Wohlfarth model of a single domain ferromagnetic particle. The models described within this chapter are implemented within the MARS code which is described in Chapter 3.

Chapter 3 describes the development of the MARS code. The key functionality of the code is provided by the combination of solvers present within in a single C++ class. The granular systems used in magnetic recording media are modelled via a Laguerre-Voronoi tessellation as opposed to the standard centroidal Voronoi tessellation commonly used. The two tessellation methods are compared and the benefits of the Laguerre-Voronoi are described and shown. Next the implementation of the various terms present in the Gibbs free energy from Chapter 2 are detailed. The energy terms are implemented as fields applied to the macrospins of the granular media. The method used to model the exchange field is described followed by the demagnetisation field. Then the anisotropy field is described including the importance of selecting the appropriate description with regards to the micromagnetic solver being used. Afterwards atomistic parameterisation is discussed. Atomistic parameterisation is used by MARS to provide the required input material parameters. The atomistic simulations used to parameterise the materials used within this work were performed using the VAMPIRE software package [14]. Finally the validation of the MARS code is detailed. Numerous simulations have been performed to test the validity and implementation of the models used within MARS. Each solver has been tested and compared to analytic solutions. The

material temperature dependent behaviours have been compared to atomistic simulations and finally HAMR dynamics simulations have been performed using MARS and VAMPIRE and compared to show excellent agreement between the two software packages.

Chapter 4 investigates the process of extracting Curie point distributions from experimental thermoremanence results. Curie point distributions present in recording media present significant issues for the performance of HAMR drives. Variations in the thermal behaviour of the grains within the recording media result in shifts in the position of the written bits due to variations in the recording temperature of the grains. Determining the Curie point distribution of a material is non-trivial thus numerous attempts have been made to develop a process by which these distributions can be determined. The proposed approach in this work uses a semi-analytical model of thermoremanence to act as a fitting function for experimental data. By simulating numerous parameter sets via a grid search it is possible to identify the underlying Curie point distribution which best describes the experimental results providing a useful method of extracting Curie point distributions from experiment. Using the developed semi-analytical model a predicted Curie point distribution has been obtained from experimental data provided by Seagate. The obtained results appear to be reasonable based on other works and provide strong evidence that the grain size distribution is the main contributing factor to the Curie point distribution and therefore efforts to minimise the Curie point distribution should focus on the reduction of the grain size distribution.

Chapter 5 covers the effect of adjacent track erasure (ATE) on the signal-to-noise ratio (SNR) of a previously written central track. Due to the closely packed nature of the data tracks on modern recording media there is a risk that the write process of one track will cause damage to a previously written adjacent track. In HAMR devices this is caused by the heated spot covering an area larger than the track width. The investigation starts with the characterisation of the ATE for repeated writes of the same pseudo-random bit sequence (PRBS) and of a random PRBS each write. These results show clearly the importance of varying the PRBS each write in order to prevent under-characterisation of the effects of the ATE. The investigation is then expanded by including the effect of time decay on the central track and comparing this effect to that of the ATE. It is shown that the strength of the effect caused by the ATE is non-negligible with respect to that of the time decay when a different PRBS is used for each adjacent track write. Finally, simulations are performed which include time spaced adjacent track writes in order to model a realistic data storage use case whereby data is originally written and then stored for a long period of time while data on the adjacent track is rewritten at monthly and yearly spaced intervals. This combination of ATE and time decay enables a clear comparison of the strength of both effects as well as providing insight

into the possibility of interplay between the effects. The obtained results show no change in the rate of SNR reduction over time due to an increasing number of adjacent track writes.

Chapter 6 discusses the experimentally observed decrease of the linewidth of the FMR power spectrum at temperatures near the Curie point [15]. This decrease has been related to a possible reduction in damping. The damping of the recording medium is important for HAMR applications due to its influence on the rate of reversal. As all switching is required to occur within a narrow temperature and time window due to the heating process any reduction in the damping can result in reduced write performance as the magnetisation cannot reverse prior to the grain cooling. A semi-analytical model has been developed and used to propose that inhomogeneous line broadening is the cause for the decreased linewidth [16]. Furthermore this decrease of the linewidth was not indicative of a reduction in the grain damping. Using MARS a more complete model of FMR of granular systems has been created. The effects of inhomogeneous line broadening over a range of temperatures close to the system's Curie point are investigated. Here we have identified the reduction of the linewidth within 40 K of the Curie point and verified inhomogeneous line broadening as the root cause. Using system parameters similar to those found in recording media we have further shown that this inhomogeneous line broadening is driven by the grain size distribution which forms concomitant distributions of the Curie point and hence the anisotropy. Next the effects of thermal broadening, a feature absent from the semi-analytical model, are investigated. Thermal broadening is shown to produce near constant linewidth at temperatures within 100 K and 40 K of the Curie point with the decrease in linewidth again observed once the temperature reaches within 40 K of the Curie point. Finally the effect of magnetostatic interactions on the FMR power spectra for a range of temperatures is investigated. These results show the convergence of the results accounting for and neglecting magnetostatics due to an increasing number of grains entering the paramagnetic regime as temperatures approach the Curie point.

2

Modelling magnetic systems

Magnetic materials exhibit complex behaviour which requires numerous descriptions based on the appropriate length and time scales for the system. As a result of this complexity there are numerous modelling methods available which each utilise varying degrees of approximation. The most ambitious models exist at the atomic scale where a discrete description is utilised. At this scale it is possible to calculate magnetic properties via the electronic structure provided by *ab initio* density functional theory simulations. While these models provide unparalleled insight into the properties of magnetic materials they are severely length scale limited being capable of only thousands of atoms when run using massively parallel computer platforms [17]. This length scale limitation leads on to the development of atomistic models for magnetic materials. By leveraging the information provided via *ab initio* simulations such as: atomic structures, inter-atomic exchange, anisotropies and magnetic moments it is possible to model the individual atoms via higher order approximations. Such atomic models are capable of simulating systems spanning hundreds of nanometres consisting of millions of atoms [14]. However even atomistic modelling is incapable of reproducing multi-micrometre or larger systems especially over timescales ranging into the microseconds. At these length scales the atomic structure can be ignored in favour of a continuous model.

The first such continuum model, micromagnetics, was developed by Brown in 1963 [18] in order to bridge the gap between Maxwell's equations and the quantum mechanical treatment of exchange as first described by Heisenberg [19]. Micromagnetics is capable of describing large systems of multi-micrometre dimensions over timescales up to microseconds depending on the specific modelling method used [20–24]. Micromagnetic theory resides at length scales which are large enough to enable the classical representation of atomic spins but still small enough to resolve magnetic domains. This classical treatment leads to the use of a continuous vector field to describe the magnetisation. In order to numerically solve these systems and describe this continuous vector field discretisation methods are implemented.

The method by which this vector field is discretised differs based on the implementation of the model. Finite difference models discretise the systems into a finite mesh of cuboids while finite element models discretise the system into differently sized 'elements' typically tetrahedral or triangular in shape [25]. There is also the macrospin approximation which identifies irreducible single-domain regions and describes them as a macrospin. These macrospins have uniform magnetisation and thus the dynamics of each macrospin can be described with a single magnetisation vector which obeys the Stoner-Wohlfarth behaviour. For modern granular media, used in heat assisted magnetic recording, the grain sizes have become sufficiently small to prevent the formation of domains. This enables these systems to be simulated using the macrospin approach with each grain being represented by a single macrospin. Figure 2.1 compares the meshes used for finite difference and finite element methods.

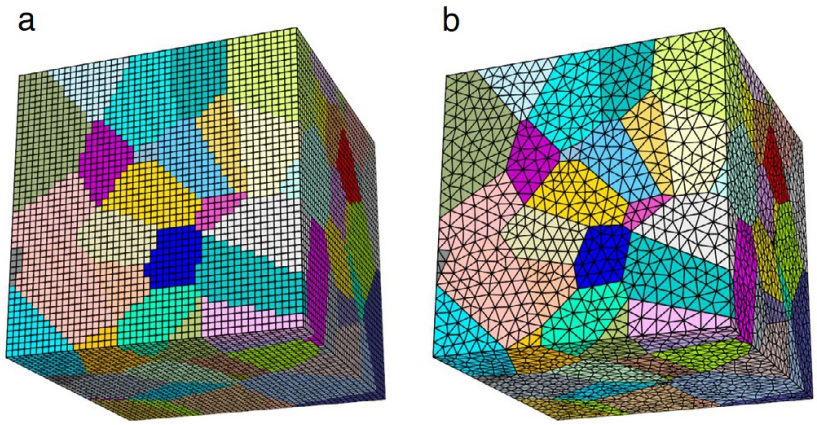

Fig. 2.1 Comparison of finite difference (a) and finite element (b) meshes. [25]

The two main methods of micromagnetic modelling are split between the description of dynamic behaviours and energy minimisation techniques. Once again, due to the complexity of magnetic materials there does not exist a single comprehensive micromagnetic model which can account for all time and length scales. The most ubiquitous model is the Landau-Lifshitz-Gilbert (LLG) equation of motion which is used to describe the dynamics of a macrospin. This model was developed by Gilbert in 1955 where he reformulated the Landau-Lifshitz equation of motion using the Lagrangian form of the undamped precessional motion and introduced a Rayleigh dissipation function to represent the damping [26]. While the LLG is a highly powerful model for the description of ferromagnetic materials it is limited with respect to temperature. At high temperatures the ferromagnetic order breaks down resulting in the loss of magnetisation of the macrospin, as the LLG assumes that the magnetisation length is conserved it cannot account for this loss of ferromagnetic order. This limitation was overcome by Garanin in 1996 where he derived the closed equation of motion for

magnetisation which interpolated between the Landau-Lifshitz (LL) and Bloch equations at low and high temperatures respectively [27]. This equation of motion is known as the Landau-Lifshitz-Bloch (LLB) equation and it enables the modelling of ferromagnetic materials for all temperatures. While there now exist two very capable dynamic micromagnetic models due to computational cost the issue of long timescale modelling still remains [20–24, 28]. Due to the time stepping nature of dynamic models it is unfeasible to reproduce long timescale effects with these models. It is at this stage where energy minimisation techniques become necessary. One such technique is the kinetic Monte Carlo (kMC), this model accounts for the energy landscape and utilises the switching probability to model magnetic materials over large timescales up to thousands of years. As a result the kMC is ideally suited to two state magnetic systems such a magnetic recording media. Throughout this work all simulations performed have used finite element models utilising the LLG, LLB, kMC or a combination thereof.

The equations provided in this work are all derived using the International System of Units (SI). This is done to provide an easy comparison with contemporary works and follows the implementation used in the MARS code. However, due to industrial standard practices all values are provided in the Centimetre-Gram-Seconds (CGS) system of units. The relationship between these unit systems for some important parameters is provided in Table 2.1.

Table 2.1 Units from the CGS and SI unit system and the respective conversion from CGS to SI.

Quantity	CGS Units	SI Units	Conversion factor (CGS to SI)
Energy (E)	erg	J	10^{-7}
Energy Density (ε)	$\mathrm{erg/cm^3}$	$\mathrm{J/m^3}$	10^{-1}
Magnetic Induction (B)	G	T	10^{-4}
Applied Field (H)	Oe	$\mathrm{A/m}$	$10^3/4\pi$
Magnetic Moment (m)	emu	$\mathrm{J/T}$	10^{-3}
Magnetisation (M)	$\mathrm{emu/cm^3}$	$\mathrm{A/m}$	10^3
Magnetisation (4πM)	G	$\mathrm{A/m}$	$10^3/4\pi$
Susceptibility (χ)	$\mathrm{emu\ cm^{-3}\ Oe^{-1}}$	Dimensionless	4π
Permeability (μ)	Dimensionless	$\mathrm{H/m}$	$4\pi \times 10^{-7}$

2.1 Total Gibbs free energy

In micromagnetics the magnetisation is described by a continuous vector field $\mathbf{M}$. For most models the modulus of the magnetisation vector is assumed constant and thus the reduced magnetisation, $\hat{m} = \mathbf{M}/M_s$, where M_s is the saturation magnetisation, is constrained to unity

and is used to describe the direction of magnetisation at each point in space. The effective field experienced by each macrospin drives many of the behaviours of the system and is thus an extremely important parameter in micromagnetic models. The effective field, $\mathbf{H}_{\text{eff}}$ is written as the derivative of the energy densities with respect to the magnetisation

$$\mathbf{H}_{\text{eff}} = -\frac{1}{\mu_0}\frac{d\varepsilon}{d\mathbf{M}}, \tag{2.1}$$

where ε is the energy density and μ_0 is the permeability of free space. The energies, E, present are calculated as volume integrals of the local energy density over the total macrospin volume, V

$$\varepsilon = \frac{dE}{dV}. \tag{2.2}$$

The total Gibbs free energy is used to describe the most likely state for a system to reside in at thermodynamic equilibrium. This energy consists of numerous energy terms each relating to a specific magnetic phenomenon. There are four main energies considered here for ferromagnetic systems.

The Zeeman energy, E_{zee}, is the energy due to an externally applied magnetic field, $\mathbf{H}_{\text{app}}$. This energy is minimised when the magnetisation and applied field are aligned. The energy is given by

$$E_{zee} = -\mu_0 \int M_s(\hat{m}\cdot\mathbf{H}_{\text{app}})dV. \tag{2.3}$$

The exchange energy arises from the exchange interaction which tries to align neighbouring spins. The exchange interaction is quantum mechanical in origin [29] arising from the Pauli exclusion principle limiting the orbital placement of the electrons and the corresponding Coulomb repulsion. The energy can be derived from the Heisenberg exchange Hamiltonian

$$\hat{\mathcal{H}}_{exch} = -\sum_{i\neq j}\mathcal{J}\hat{S}_i\cdot\hat{S}_j, \tag{2.4}$$

where $\hat{S}_i$ and $\hat{S}_j$ are two neighbouring spins and $\mathcal{J}$ is the exchange interaction strength. For ferromagnetic materials $\mathcal{J}$ is positive. It is desirable to determine the exchange energy considering all spins within the system however this is a non-trivial task for the desired system sizes of micromagnetic models. $\mathcal{J}$ can be approximated such that it is constant for nearest neighbours and zero further away. If it is assumed that misalignment between neighbouring spins are small then the exchange energy can be written as

$$E_{exch} = \int A_{ex}(\nabla\hat{m})^2 dV. \tag{2.5}$$

A_{ex} is the exchange stiffness and is related to the exchange integral J, lattice constant a, spin quantum number S and the number of neighbours z. Thus the exchange stiffness is given by $A_{ex} = 2JS^2z/a$.

The magnetostatic energy arises from the long-range dipolar interactions between magnetic dipoles. According to Maxwell's equations while no external field acts

$$\nabla \cdot \mathbf{H}_{dmg} = -\nabla \cdot \mathbf{M}. \tag{2.6}$$

The demagnetising field is conservative thus its curl is zero. Since $\nabla \times \nabla f(r) = 0$ for any scalar, $\mathbf{H}_{dmg}$ can be expressed as

$$\mathbf{H}_{dmg} = -\nabla U, \tag{2.7}$$

In order to satisfy Poisson's equation

$$\nabla^2 U = \nabla \cdot \mathbf{M}, \tag{2.8}$$

From Gauss' law for magnetism all flux entering normal to a surface must be equal to all flux exiting normal to the surface of the magnet. Substituting $\mathbf{H}_{dmg} = -\nabla U$ into Eq. 2.6 it can be shown that

$$\mathbf{M} \cdot \mathbf{n} = (\nabla U_{in} - \nabla U_{out}) \cdot \mathbf{n}, \tag{2.9}$$

where $\mathbf{n}$ is the surface normal. The stray field energy can then be determined by the integral over the volume of the magnet

$$E_{stray} = \frac{\mu_0}{2} \int_{magnet} \nabla U \cdot \mathbf{M} dV. \tag{2.10}$$

The potential can be described as the sum of two potentials similar to electrostatics, one of a volumetric charge distribution, with associated density $\rho_m = -\nabla \cdot \mathbf{M}$ and the other as a surface charge distribution, $\sigma_m = \mathbf{n} \cdot \mathbf{M}$. In reality these charges do not exist however the mathematical description is similar that of electrostatics. For a magnetic body the integral must be performed over a closed volume, thus the potential can be written as follows:

$$U(\mathbf{r}) = \frac{1}{4\pi} \left(\int_{V'} \frac{\rho_m(\mathbf{r}')}{|\mathbf{r} - \mathbf{r}'|} dV' + \int_{S'} \frac{\sigma_m(\mathbf{r}')}{|\mathbf{r} - \mathbf{r}'|} dS' \right). \tag{2.11}$$

The anisotropy energy arises from the preferred direction of the magnetisation via spin-orbit coupling due to the crystal lattice structure. This direction is referred to as an easy axis when one-dimensional. For the simplest case of uniaxial anisotropy parallel orientation is the energetically favourable state. The anisotropic energy density, for the first two terms,can be

written as

$$\varepsilon_{uni} = K_1 sin^2(\theta) + K_2 sin^4(\theta) = K_1(1-m_z^2) + K_2(1-m_z^2)^2, \tag{2.12}$$

where θ denotes the angle between the magnetisation vector and easy axis direction. In general micromagnetic models forgo the K_2 term when it is significantly smaller in magnitude than K_1. Neglecting the second term and setting K_1 as the uniaxial anisotropy K_u the anisotropy energy for a ferromagnetic material with an easy axis denoted by $\hat{e}$ is

$$E_{ani} = -\int K_u(\hat{e}\cdot\hat{m})^2 dV. \tag{2.13}$$

Combined these four energies produce the total Gibbs free energy:

$$E_{tot} = -\int K_u(\hat{e}\cdot\hat{m})^2 dV + \frac{\mu_0}{2}\int_\Omega \nabla U\cdot\mathbf{M}dV + \int A_{ex}(\nabla\hat{m})^2 dV - \mu_0\int M_s(\hat{m}\cdot\mathbf{H}_{\text{app}})dV. \tag{2.14}$$

This energy equation provides sufficient information to model the ferromagnetic system. The derived fields and subsequent implementation are detailed in Chapter 3. To simplify the discussion of the key micromagnetic solvers the effective field will be used throughout the rest of this chapter.

2.2 Landau-Lifshitz-Gilbert equation of motion

In 1935 Landau and Lifshitz introduced a phenomenological model to described the dynamics of a ferromagnetic object under isothermal conditions at temperature below the Curie point, T_c, this model is now referred to as the Landau-Lifshitz equation. Landau and Lifshitz started with the well established Larmor equation

$$\frac{d\hat{m}}{dt} = -\gamma\hat{m}\times\mathbf{H}_{\text{eff}}, \tag{2.15}$$

where $\gamma = 1.7609\times10^7\ s^{-1}Oe^{-1}$ is the electron gyromagnetic ratio and $\mathbf{H}_{\text{eff}}$ is the effective magnetic field. The Larmor equation is unable to account for the observed rapid relaxation of the magnetisation towards an equilibrium direction. Landau and Lifshitz thus added a damping term to account for the relaxation of the magnetisation towards the effective field, this is the Landau-Lifshitz (LL) equation:

$$\frac{d\hat{m}}{dt} = -\gamma\hat{m}\times\mathbf{H}_{\text{eff}} - \Lambda\hat{m}\times(\hat{m}\times\mathbf{H}_{\text{eff}}), \tag{2.16}$$

Λ is the phenomenological damping parameter, which is an intrinsic property of the material. Experimental measurements of 4-79 Molybdenum permalloy by J. M. Kelly revealed much greater damping than accounted for by the Landau-Lifshitz equation [30]. T. L. Gilbert identified that, while a frequency dependent damping $\Lambda = \alpha\gamma$ could not describe the data, a fixed gyromagnetic ratio $\Lambda_G = \gamma/(1+\alpha_G^2)$ along with a frequency dependent α_G could. This development lead on to the formulation of the Landau-Lifshitz-Gilbert equation:

$$\frac{d\hat{m}}{dt} = -\frac{\gamma}{1+\alpha_G^2}\left(\hat{m}\times\mathbf{H}_{\text{eff}}\right) - \frac{\alpha_G\gamma}{1+\alpha_G^2}\hat{m}\times\left(\hat{m}\times\mathbf{H}_{\text{eff}}\right) . \tag{2.17}$$

In the limit of vanishing damping the LLG recovers the LL equation, however in the limit of infinite damping for the LLG equation, $d\hat{m}/dt \to 0$, whereas for the LL equation, $d\hat{m}/dt \to \infty$. It is expected that in the presence of very high damping the rate change of the magnetisation will be very slow.

In order to model systems at finite temperatures one must be able to account for thermal noise. For the LLG this is done via the inclusion of an additive noise term denoted as a thermal field, $\mathbf{H}_{\text{th}}$. The LLG, for each macrospin i, then becomes:

$$\frac{d\hat{m}^i}{dt} = -\frac{\gamma}{1+\alpha_G^2}\left(\hat{m}^i\times(\mathbf{H}^i_{\text{eff}}+\mathbf{H}^i_{\text{th}})\right) - \frac{\alpha_G\gamma}{1+\alpha_G^2}\hat{m}^i\times\left(\hat{m}^i\times(\mathbf{H}^i_{\text{eff}}+\mathbf{H}^i_{\text{th}})\right) . \tag{2.18}$$

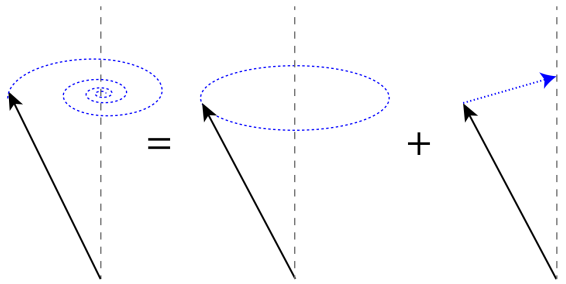

The first term describes the quantum mechanical precessional motion of the magnetisation around $\mathbf{H}^i_{\text{eff}}$, while the second represents the phenomenological relaxation of the magnetisation towards $\mathbf{H}^i_{\text{eff}}$ [31].

The Gilbert damping α_G couples the spin system with the environment, considered to act as the thermal bath, and determines how fast the system relaxes towards equilibrium. The

thermal field accounts is described by a non-correlated white noise Gaussian function.

$$\begin{aligned} \langle H_{\text{th}}^{i\alpha}(t)\rangle &= 0 \\ \langle H_{\text{th}}^{i\alpha}(t) H_{\text{th}}^{j\beta}(t')\rangle &= \frac{2\alpha k_B T}{\gamma_e M_s V}\delta_{ij}\delta_{\alpha\beta}\delta(t-t') \,, \end{aligned} \tag{2.19}$$

where i and j label the magnetisation on the respective sites; $\alpha,\beta = x,y,z$. T is the temperature, $k_{\text{B}} = 1.381\cdot 10^{-16}\,\text{ergK}^{-1}$ is the Boltzmann constant, $\delta_{\mu\gamma}$ is the Kronecker delta and $\delta(t-t')$ is the delta function. In this formulation the noise is considered to be spatially and temporally uncorrelated.

The key limitation of the LLG arises from its basis on the Larmor equation. The Larmor equation describes the derivative of the magnetisation to be perpendicular to the magnetisation thus the modulus of the magnetisation is preserved limiting the validity to magnetically saturated bodies only. At elevated temperatures the ferromagnetic order of the magnetisation is known to break down with the total loss of ferromagnetic order at the Curie point [32]. As a result at elevated temperatures near the Curie point the modulus of the magnetisation vector is not constant [33, 34]. In order to enable high temperature modelling of ferromagnetic materials a different model is required.

2.3 Landau-Lifshitz-Bloch equation of motion

In 1946 F. Bloch formulated a set of equations to describe the behaviour of a nuclear spin in a magnetic field under radio frequency (rf) pulses [35]. Bloch started by modifying Eq. 2.15 to account for the observed relaxation towards an equilibrium during application of the rf pulses. Bloch assumed a relaxation along the z-axis and xy-plane at different rates following first order kinetics. The phenomenological Bloch equation is given by:

$$\frac{d\mathbf{M}}{dt} = \gamma\mathbf{M}\times\mathbf{H}_{\text{eff}} - \mathbf{R}(\mathbf{M}-\mathbf{M_0}), \tag{2.20}$$

where $\mathbf{R}$ is the relaxation matrix. At T_c the magnetic ordering of a ferromagnet is lost and it becomes a paramagnet, at this point the Bloch equations are used to describe the object's behaviour. In 1996 Garanin developed a model to interpolate between the low temperature LL equation and the high temperature Bloch equation [27]. To start Garanin considered a magnetic atom as a classical spin vector, $\hat{S}$, of unit length interacting with a heat bath at temperature T and applied the stochastic Landau-Lifshitz equation:

$$\frac{d\hat{S}}{dt} = \gamma\hat{S}\times(\mathbf{H}_{\text{eff}}+\boldsymbol{\zeta}) - \gamma\lambda(\hat{S}\times(\hat{S}\times\mathbf{H}_{\text{eff}})), \tag{2.21}$$

where λ is the thermal bath coupling and $\boldsymbol{\zeta}$ is the Langevin field. The correlators of the $\alpha, \beta = x, y, z$ components of the Langevin field are given by:

$$\langle \zeta_\alpha(t)\zeta_\beta(t')\rangle = \frac{2\lambda T}{\gamma\mu_0}\delta_{\alpha\beta}\delta(t-t'), \tag{2.22}$$

Garanin formulated the the Fokker-Planck equation corresponding to Eq. 2.21 and derived the equation of motion for the spin polarisation of an ensemble of magnetic atoms. While including the spin-spin interactions, which give rise to ferromagnetism, Garanin derived within a mean-field approximation the equation which describes the dynamics of the macroscopic magnetisation, $\mathbf{M} = \mathbf{m}/v_0$, where v_0 is the unit-cell volume. This final result is known as the Landau-Lifshitz-Bloch equation:

$$\frac{d\mathbf{M}}{dt} = -\gamma[\mathbf{M}\times\mathbf{H}_{\text{eff}}] + \frac{L_1}{M^2}(\mathbf{M}\cdot\mathbf{H}_{\text{eff}})\mathbf{M} - \frac{L_2}{M^2}[\mathbf{M}\times[\mathbf{M}\times\mathbf{H}_{\text{eff}}]], \tag{2.23}$$

where L_1 and L_2 are the longitudinal and transverse kinetic coefficients,

$$L_{1,2} = \gamma M_e \alpha_{1,2} \tag{2.24}$$

$$\alpha = \lambda_{1,2}/m_e, \tag{2.25}$$

α_1 and α_2 are the corresponding Gilbert damping parameters, M_e and m_e are the equilibrium and reduced equilibrium magnetisations. These coefficients are dependent on the temperature such that for $T \ll T_c$, L_1 tends to zero, while at the Curie point $L_1 = L_2$.

To use the LLB at finite temperatures, as with the LLG, the implementation of thermal noise is required. This implementation was first performed by Garanin and Chubykalo-Fesenko in 2004 [33]. This implementation utilised an additional field with noise terms which were isotropic, multiplicative and differed for both longitudinal and transverse directions. As shown by Chubykalo et al. [34], the LLB equation gives excellent agreement with atomistic model calculations, essentially validating its use in simulations at and exceeding the Curie point. However in 2012 Evans et al. showed that this initial form of the stochastic LLB was unable to recover the correct Boltzmann distribution at elevated temperatures and proposed a new form for the stochastic LLB [36]. This stochastic LLB correctly reproduces the Boltzmann distribution at elevated temperatures, introduces additive noise and for a

macrospin i is given by:

$$\frac{d\mathbf{m}^i}{dt} = -\gamma\left(\mathbf{m}^i \times \mathbf{H}^i_{\text{eff}}\right) + \frac{\gamma\alpha_{\parallel}}{m^{i2}}\left(\mathbf{m}^i \cdot \mathbf{H}^i_{\text{eff}}\right)\mathbf{m}^i - \frac{\gamma\alpha_{\perp}}{m^{i2}}\left[\mathbf{m}^i \times \left(\mathbf{m}^i \times \left(\mathbf{H}^i_{\text{eff}} + \boldsymbol{\zeta}^i_{\perp}\right)\right)\right] + \boldsymbol{\zeta}^i_{ad}\,. \tag{2.26}$$

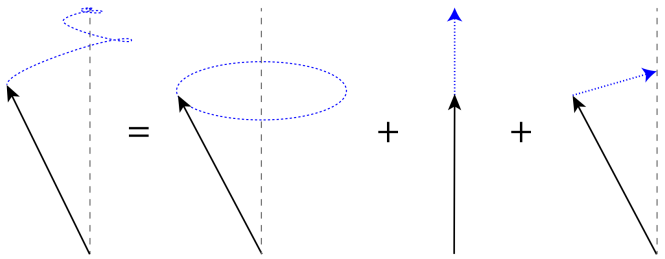

The first and third terms are the precessional and damping terms for the transverse component of the magnetisation, as in Eq. 2.17, while the second and fourth terms are introduced to account for the longitudinal relaxation of the magnetisation with temperature. $\boldsymbol{\zeta}_{\perp}$ and $\boldsymbol{\zeta}_{ad}$ are the diffusion coefficients that account for the thermal fluctuations. The thermal noise terms are described by Gaussian functions with zero average and a variance proportional to the strength of the fluctuations:

$$\begin{aligned} <\zeta^{i\alpha}_{\text{ad}}(t)\zeta^{j\beta}_{\text{ad}}(t')> &= \frac{2|\gamma|k_B T\alpha_{\parallel}}{M_s V}\delta_{ij}\delta_{\alpha\beta}\delta(t-t') \\ <\zeta^{i\alpha}_{\perp}(t)\zeta^{j\beta}_{\perp}(t')> &= \frac{2k_B T(\alpha_{\perp}-\alpha_{\parallel})}{|\gamma|M_s V\alpha^2_{\perp}}\delta_{ij}\delta_{\alpha\beta}\delta(t-t')\,. \end{aligned} \tag{2.27}$$

The damping of the magnetic moment is split into longitudinal $\alpha_{\parallel}$ and transverse $\alpha_{\perp}$ components given by:

$$\alpha_{\parallel} = \frac{2}{3}\frac{T}{T_c}\lambda \quad \text{and} \quad \begin{cases} \alpha_{\perp} = \lambda\left(1 - \dfrac{T}{3T_c}\right), & \text{if } T \leq T_c \\ \alpha_{\perp} = \alpha_{\parallel} = \dfrac{2}{3}\dfrac{T}{T_c}\lambda, & \text{otherwise,} \end{cases} \tag{2.28}$$

where λ is the thermal bath coupling, a temperature independent phenomenological parameter, that is the same as that used in atomistic spin dynamics. The transverse damping is related to

the Gilbert damping by the expression:

$$\alpha_G = \frac{\alpha_\perp}{m} \,, \tag{2.29}$$

In the case where $T \to 0$ the parallel damping tends to zero and the perpendicular tends to λ thus the equation reduces to the LLG equation. In the paramagnetic regime above the Curie point the longitudinal and transverse damping are equivalent and thus the equation reduces to the Bloch equation.

The LLB equation introduces an additional field term, $\mathbf{H}^i_{\text{intragrain}}$, within the effective field. This term accounts for the intragranular exchange and controls the length of the magnetisation and is given by

$$\mathbf{H}^i_{\text{intragrain}} = \begin{cases} \dfrac{1}{2\tilde{\chi}_\parallel}\left(1 - \dfrac{m^{i^2}}{m_e^2}\right)\mathbf{m}^i, & \text{if } T \leq T_c \\ -\dfrac{1}{\tilde{\chi}_\parallel}\left(1 + \dfrac{3}{5}\dfrac{T_\text{c}}{T - T_c} m^{i^2}\right)\mathbf{m}^i, & \text{otherwise.} \end{cases} \tag{2.30}$$

Here m^i is length of the reduced magnetisation $\mathbf{m}^i$ of grain i, and $m_e(T)$ is the equilibrium magnetisation. The term $\mathbf{H}_{\text{intragrain}}$ encapsulates the new physics introduced by the LLB equation. It incorporates the longitudinal fluctuations of the magnetisation while maintaining a mean value $m_e(T)$. It is important to note that the fluctuations diverge as $\tilde{\chi}_\parallel$ diverges close to T_c. This is responsible for the onset of the linear reversal model close to T_c, which will be considered in detail later.

2.4 Kinetic Monte Carlo

Using the LLG and LLB equations it is possible to simulate ferromagnetic systems for all temperatures. These two equations form the basis of the dynamic solvers used within this work. However, in order to simulate long time scale processes and behaviours a fundamental change of method is required. This is achieved by starting with the Stoner-Wohlfarth (SW) model. Developed by E. C. Stoner and E. P. Wohlfarth in 1948 the model describes the behaviour of a mono-domain particle of volume, V, with a saturation magnetisation, M_s, and uniaxial anisotropy under the influence of an applied field assuming a system temperature of 0 K [37]. In the SW model the behaviour of the particle is described via energy minimisation.

The free energy of a SW particle is given by

$$E = K_u V(\hat{\mathbf{e}} \cdot \hat{m})^2 - \mu \mathbf{H} \cdot \hat{m} \,. \tag{2.31}$$

where $\hat{\mathbf{e}}$ is the easy axis direction. For a particle with an easy axis parallel to the z-axis under an applied field at an angle θ_0, the magnetic moment will correspond to the minimum energy configuration which can be proven to exist in the plane defined by the easy axis and applied field. The energy of the particle can therefore be described by

$$E = -K_u V \cos^2(\theta) - M_s H_{app} \cos(\theta_0 - \theta). \tag{2.32}$$

In an applied field there are two possible energy minima at $\theta = \theta_0$ and $\theta = \theta_0 + \pi$ separated by a maximum energy at $\theta = \theta_0 + \pi/2$. The conditions at which switching can occur are when the two energy minima merge or one is removed. The field at which these conditions occur is the critical field

$$H_{cr} = \frac{H_k}{g(\theta_0)}, \tag{2.33}$$

where $H_k = 2K_u/M_s$ is the anisotropy field and $g(\theta_0) = [\sin^{2/3}(\theta_0) + \cos^{2/3}(\theta_0)]^{3/2}$. The energy barrier for a particle with easy axis parallel to the applied field is determined by

$$\Delta E_{12,21} = K_u V \left(1 \pm \frac{H_{app}}{H_k}\right)^2, \tag{2.34}$$

where the plus and minus correspond to the direction of the transition between minima. It is common for systems of particles to have distributed easy axis directions, for recording media these differences arise from the fabrication process. The total energy barrier including anisotropy dispersion is given by

$$\Delta E_{12,21}(\mathbf{H}_{eff}, \theta) = K_u V \left[1 \pm \frac{\mathbf{H}_{eff}}{g(\theta)}\right]^{\kappa(\theta)}, \tag{2.35}$$

where $\kappa(\theta) = 0.86 + 1.14 g(\theta)$ is the Pfeiffer approximation [38].

The direction and energy barrier have now been determined, however this has been undertaken in the absence of thermal noise. For a finite temperature the particle will experience a random walk around the equilibrium direction due to the stochastic forces acting upon it. For sufficient noise it is possible for the particle to overcome the energy barrier and reverse, this phenomenon is known as thermally activated reversal. W. F. Brown investigated the thermally activated reversal using the Fokker-Planck equation in 1963 [39]. This work resulted in the determination that dynamical behaviour is characterised by short timescales around the nanosecond regime with long timescale behaviour described by the

Arrhenius-Néel law [40]. For a two state system the Arrhenius-Néel law is

$$\tau^{-1} = f_0\Big(\exp\Big[-\frac{\Delta E_{12}}{k_B T}\Big] + \exp\Big[-\frac{\Delta E_{21}}{k_B T}\Big]\Big), \tag{2.36}$$

where τ is the relaxation time and f_0 is the attempt frequency, usually assumed to beof the order of GHz.

The kMC approach utilises the Arrhenius-Néel law to determine the switching probability of a particle [41]. The switching probability for a measurement time, t_m is given by

$$P_t = 1 - \exp\Big[-t_m/\tau\Big], \tag{2.37}$$

Combining Eq. 2.36 and Eq. 2.35 the kMC is capable of modelling the switching of a two-state particle at finite temperatures, the energy landscape for such a particle is illustrated in Fig. 2.2.

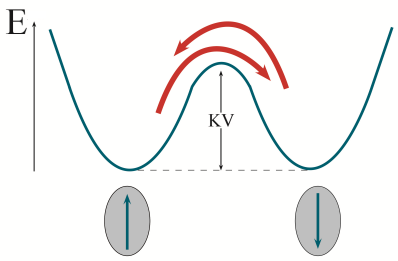

Fig. 2.2 Energy landscape of a SW particle in the absence of an external field. Two local minima exist representing the two possible alignments of the magnetisation. These minima are separated by an energy barrier. When there is sufficient thermal energy the magnetisation can flip.

In order to ensure that the populations of the energy minima obey Boltzmann statistics after switching the condition that reversal can occur in either direction is applied. The probability of the energy minima the particle will switch to is described by

$$p_i = \frac{\exp\Big[-E_i\Big]}{\exp\Big[-E_1\Big] + \exp\Big[-E_2\Big]}, \tag{2.38}$$

where i labels the minima. This probability ensures that the two states obey Boltzmann statistics in thermal equilibrium. Taking account of the distributions of both minima as well

as the 'back switching' the transition probability is determined by

$$P_2 = \left(1 - \exp\left[-\frac{t_m}{\tau}\right]\right)\left(1 + \exp\left[-\frac{(E_2 - E_1)}{k_B T}\right]\right)^{-1}, \tag{2.39}$$

where P_2 is the probability of the magnetic moment jumping to the second minimum and ΔE is the energy barrier separating the two minima. To determine if a switching event occurs a random number between zero and unity is generated and compared to P_2. If it is less than P_2 the magnetic moment orientation is assigned corresponding to the second minimum otherwise it is assigned to the first minimum. t_m is the measurement time. During the measurement time the external properties such as magnetic field and temperature are assumed constant, such that Eq. 2.39 can be applied.

With the addition of the kMC solver it is possible to model ferromagnetic systems for all temperatures as well as over short and long timescales. The combination of these three solver (LLG, LLB, kMC) form the basis of the developed MARS software package. The next chapter details the implementation and validation of the MARS code with subsequent chapters showing the work performed, made possible by the creation of the MARS software package.

3

MARS model development and validation

MARS is an open-source multi-timescale micromagnetic code combining three key solvers: Landau-Lifshitz-Gilbert (LLG); Landau-Lifshitz-Bloch (LLB); kinetic Monte Carlo (kMC). MARS is cross-platform, working on Linux, macOS and Windows, and is completely open-source. The source code can be downloaded at **bitbucket.org/EwanRannala/mars**. MARS is capable of accurately simulating the magnetisation dynamics in large and structurally complex single- and multi-layered granular systems. The short timescale simulations are achieved for systems far from and close to the Curie point via the implemented LLG and LLB solvers respectively. This enables read/write simulations for general perpendicular magnetic recording and also state of the art HAMR. The long timescale behaviour is simulated via the kMC solver, enabling investigations into signal-to-noise ratio and data longevity. Figure 3.1 illustrates the benefits of multi-timescale micromagnetic modelling over atomistic and standard micromagnetics. A multi-timescale model is capable of encompassing a far greater range of simulation types which can cover large ranges in both spatial and temporal dimensions.

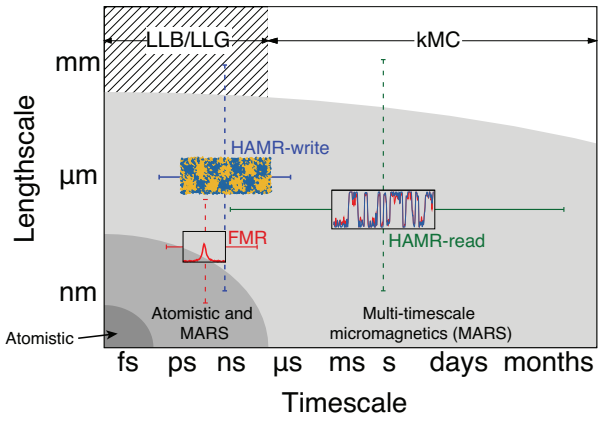

Fig. 3.1 Time and length scales required by common magnetic simulation types.

3.1 Solver class

The key feature of MARS is the combination of three micromagnetic solvers into a single C++ class. This class is then accessed by each simulation to perform the numerical integration. This abstraction enables simulations to be developed generally without specific focus on the desired solver. The solver utilised by MARS is then determined by configuration file input or automatically by MARS based on system parameters (i.e. simulation timescale and temperature). This methodology also enables MARS to dynamically switch between solvers during a simulation in order to improve computational efficiency or switch between timescales.

The details of the micromagnetic solvers employed by MARS were provided in Chapter 2. The implementation of both the LLG and LLB solvers utilises the Heun integration scheme. The benefits of the Heun scheme are two-fold. First it provides second order accuracy in Δt for the deterministic part, thus rendering it more numerically stable than Euler type schemes. Second, it yields the required Stratonovich solution of stochastic differential equations. Figure 3.2 illustrates the process used by the solver class to select the desired solver.

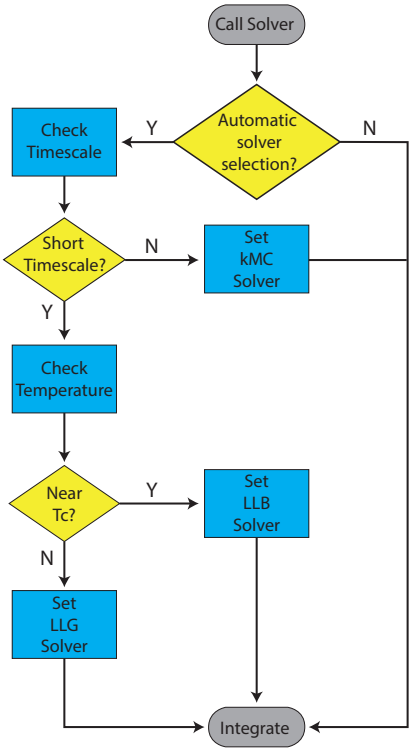

Fig. 3.2 Flowchart for the solver selection process within the solver class.

3.2 Granular model

To model granular systems it is crucial to generate accurate granular structures. The typical method for generating granular structures is via Voronoi tessellation [42–45]. The classical Voronoi algorithm starts with the creation of seed points throughout the system, cell walls are then created such that they lie halfway between two seed points. While the general process is the same there exist various methods to determine the initial locations of the seed points [46, 47].

A major drawback with the classical Voronoi construction is evident when a distribution of grain sizes is required. When there is a local increase in seed density the construction can generate unrealistically angular cells, this can be seen in Fig. 3.3a. This occurs due to the only constraint on cell construction being the requirement that the cell wall must be equidistant between seed points. To overcome this drawback, one can utilise centroidal Voronoi tessellation, this modified Voronoi process has been shown to be most effective when combined with Lloyd's algorithm [48, 49]. The process involves iterative relaxation of the constructed granular system by replacing the initial seed points with the centroids (typically known as the centre of mass) of the generated cells until convergence is achieved. Figure 3.3 shows the system generated via MARS using centroidal Voronoi tessellation followed by the changes produced by applying Lloyd's algorithm over three iterations.

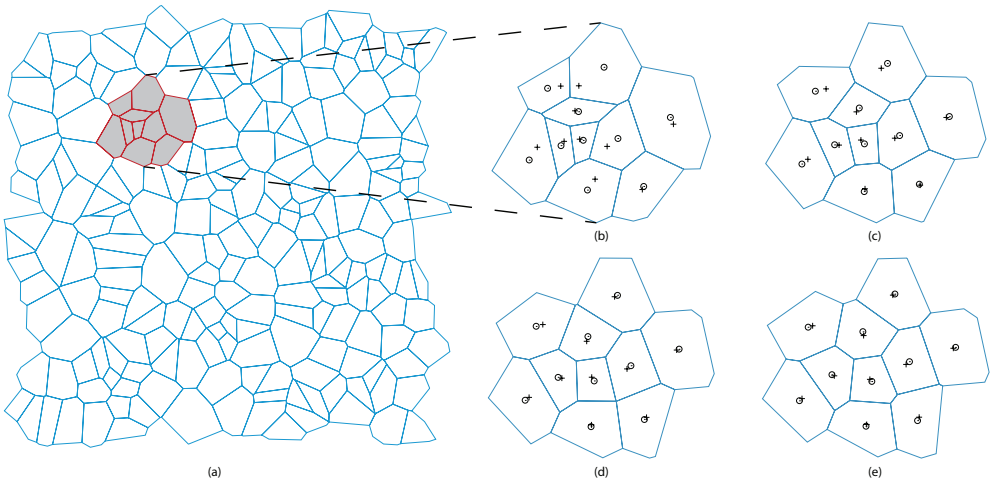

Fig. 3.3 Example of the granular structure obtained via the centroidal Voronoi tessellation (a). A subsection has been chosen to illustrate Lloyd's relaxation algorithm after: zero (b), one (c), two (d) and three (e) iterations. The seed points are indicated by the crosses with the centroids represented by the circles. As more iterations are performed the angular nature of the grains is reduced.

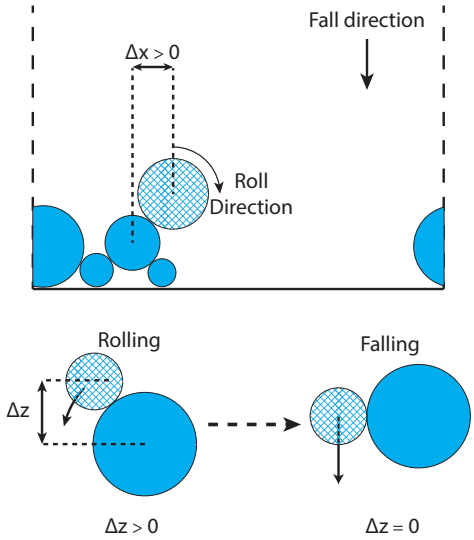

Fig. 3.4 Illustration of the Drop and Roll packing algorithm implemented in MARS (top). Placed discs are represented with filled circles, moving discs with patterned circles. The dashed lines indicate periodic boundaries while non-periodic boundaries are represented with solid lines. The bottom part shows the transition from rolling to falling, which is dependent on the z-displacement between the centres of the contacting discs.

A key limitation to all seed-based construction techniques is that they produce Gaussian cell size distributions [50, 51]. In reality the grain size distribution has been shown to be described best by log-normal or Gamma distributions [52–54]. To enable the construction of systems following these distributions a method for performing a Voronoi construction using 'hard discs' instead of seeds is available, called the Laguerre-Voronoi method. The presence of log-normal grain size distributions in recording media makes the Laguerre-Voronoi method a necessity. This method is implemented as follows: to begin the system is packed with hard discs following which the Laguerre-Voronoi tessellation is performed. The hard discs are generated such that their size is log-normally distributed. In order to pack the discs a custom "Drop and Roll" method has been implemented. This drop and roll method works by dropping the hard discs one at a time from the top of the system. These discs fall until they reach the bottom of the system or become trapped by collisions with previously placed discs. Periodic boundaries are used for the side walls in order to prevent the formation of large vacancies, which manifest as unrealistic large cells in the granular structure after tessellation. When a disc collides with a placed disc it begins to roll. During the rolling phase the disc is moved along the circumference of the other disc in either a clockwise or anti-clockwise direction depending upon the polarity of the x-displacement between the disc centres. If the z-displacement of the disc becomes zero then the rolling disc resumes falling. This process is repeated until the disc is trapped. The process of the drop and roll is illustrated in Fig. 3.4.

The Drop and Roll method in general provides a high level of contact between neighbouring discs resulting in a greater packing fraction while being computationally efficient [55]. Using this algorithm MARS is capable of filling over 80 % of the system with randomly sized discs. The tessellation is performed using the robust open source VORO++ package developed by Rycroft [56].

Figure 3.5 shows the difference between the structures generated via the centroidal Voronoi tessellation and the Laguerre-Voronoi tessellation, the corresponding grain size distributions are shown in Fig. 3.6. The implementation of the Laguerre-Voronoi tessellation method within MARS enables the generation of realistic granular systems with a high level of control over the grain size distributions. For micromagnetic simulations periodic boundary conditions are used for the Voronoi tessellation in order to remove edge effects, Fig. 3.7 shows a system created via a Laguerre-Voronoi tessellation with the periodic boundaries indicated by dashed lines.

Figure 3.8 shows the generation of a granular media via the Laguerre-Voronoi tessellation within MARS to model an $L1_0$ FePt system presented by D. Weller et al. [57]. The structure of the generated material matches extremely closely to that of the real world material, showing that the implemented construction method is well suited to the generation of realistic granular structures. Furthermore the grain size distribution of the simulated material also matches extremely well with the real world system.

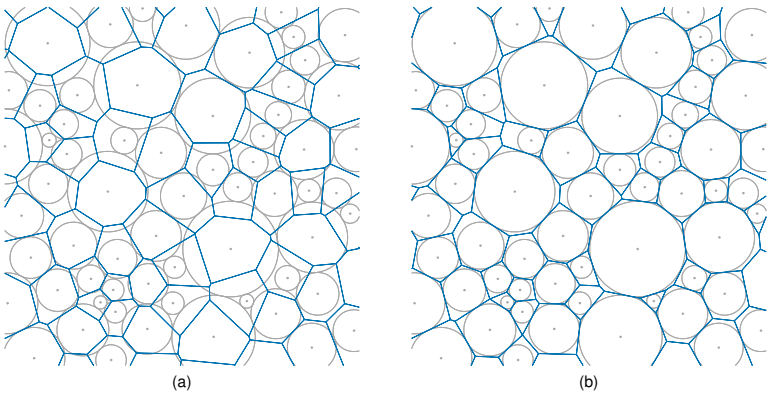

Fig. 3.5 Granular system generated from an single arrangement of hard discs via the centroidal Voronoi tessellation (a) and the Laguerre-Voronoi tessellation (b).

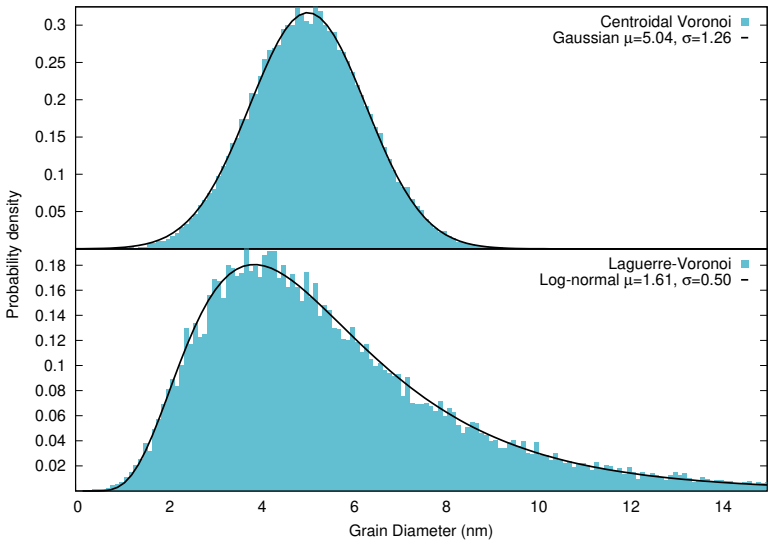

Fig. 3.6 Grain diameter distributions for centroidal Voronoi tessellation (top) and Laguerre-Voronoi tessellation (bottom). The input distribution was log-normal with $\mu = 1.65$ and $\sigma = 0.55$. The seed based Voronoi is unable to provide the desired distribution, instead providing a Gaussian. The Laguerre-Voronoi was able to produce the desired distribution type with only a small change of parameters, which is to be expected due to the random nature of the packing process.

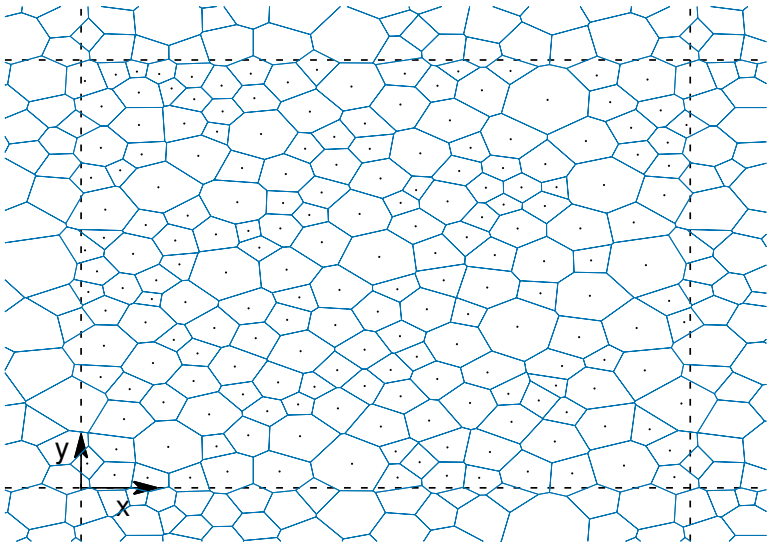

Fig. 3.7 Example of the periodic system generated via MARS using a Laguerre-Voronoi tessellation. The grains containing points are those generated, with the dashed lines indicating the periodic repetitions.

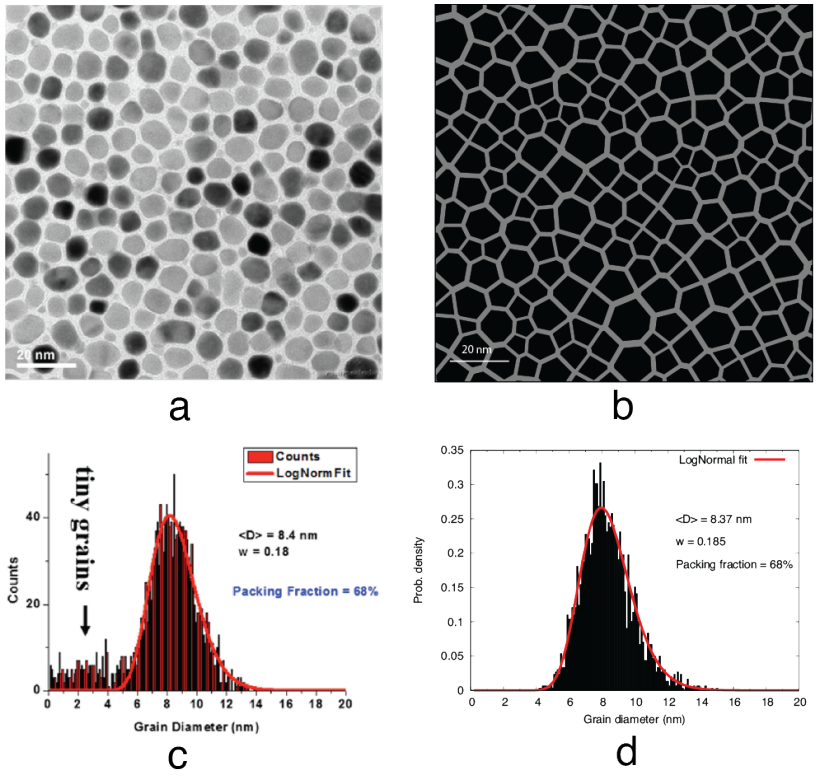

Fig. 3.8 Comparison between real world granular structure (a) and one generated via the implemented Laguerre-Voronoi tessellation (b). The corresponding grain size distributions for the real world (c) and simulated (d) systems are also provided for comparison. The measured mean diameter was 8.4 nm which was log-normally distributed with a dispersion of 18 %. The generated system produced a mean diameter of 8.37 nm which was also log-normally distributed with a dispersion of 18.5 %. Both systems have a packing fraction of 68 %. Both comparisons show excellent agreement with the real world system validating the tessellation method implemented within MARS. (a) and (c) are obtained from Weller et al. [57]

3.3 Implementation of the effective field

The effective field used in the LLG (Eq. 2.17) and LLB (Eq. 2.26) is obtained from the energy of the system (Eq. 2.14) and is given by:

$$\mathbf{H}^i_{\text{eff}} = \mathbf{H}_{\text{app}} + \mathbf{H}^i_{\text{ani}} + \mathbf{H}^i_{\text{exch}} + \mathbf{H}^i_{\text{dmg}} \,. \tag{3.1}$$

The individual terms are described and implemented as follows:

3.3.1 Exchange field

$\mathbf{H}^i_{\text{exch}}$ describes the coupling between different grains, belonging either to the same layer or to different layers as in the case of exchange-coupled composite (ECC) media. In the case of a granular medium the exchange results from the intergranular medium. Although this is engineered to ensure exchange decoupling, this is not necessarily complete: in fact in the case of media for perpendicular recording the exchange, which balances the effects of the magnetostatic field, is a part of the material design. Under the reasonable assumption that the intergranular exchange is proportional to the contact area between the grains, Peng et al. have shown that the exchange $\mathbf{H}^i_{\text{exch}}$ is given by [58]:

$$\mathbf{H}^i_{\text{exch}} = \sum_{j \in neigh\, i} H_{\text{sat}} J_{ij} \frac{\langle A \rangle}{A_i} \frac{L_{ij}}{\langle L \rangle} \mathbf{m}^j \,, \tag{3.2}$$

J_{ij} is the fractional exchange constant between the adjacent grains and L_{ij} is the contact length between grains i and j, A_i is the area of grain i, $\langle\ \rangle$ denotes the average value and H_{sat} is the exchange field strength at saturation, which is generally derived from experiment. Sokalski et al. [59] investigated experimentally the exchange coupling between thin layers of CoCrPt separated by an oxide, finding an exchange strength which decayed exponentially with oxide layer thickness. Ellis et al. [60] found a similar relation using an atomistic model based on the presence of ferromagnetic impurities in the oxide layer. This study also showed the presence of higher order (biquadratic) exchange and importantly demonstrated that the intergranular exchange decayed to zero rapidly with increasing temperature, suggesting that intergranular exchange does not play a major role in the HAMR recording process. It is important to note, given the likely origin of intergranular exchange arising from the presence of impurity magnetic spins in the intergranular layer, that J_{ij} could vary significantly. According to Peng et al. [58] this can lead to exchange weak links which act as pinning sites and reduce the size of clusters arising from magnetostatic interactions.

3.3.2 Demagnetisation field

$\mathbf{H}^i_{\text{dmg}}$ is calculated using the dipole approximation:

$$\mathbf{H}^i_{\text{dmg}} = \sum_{j \in neigh\, i} W_{ij} \mathbf{m}_j \,, \tag{3.3}$$

where W_{ij} is the demagnetisation tensor of the system:

$$W_{ij} = \frac{M_s V_j}{4\pi r_{ij}^3} \begin{bmatrix} \frac{3r_{ij_x}^2}{r_{ij}^2} - 1 & \frac{3r_{ij_x} r_{ij_y}}{r_{ij}^2} & \frac{3r_{ij_x} r_{ij_z}}{r_{ij}^2} \\ \frac{3r_{ij_y} r_{ij_x}}{r_{ij}^2} & \frac{3r_{ij_y}^2}{r_{ij}^2} - 1 & \frac{3r_{ij_y} r_{ij_z}}{r_{ij}^2} \\ \frac{3r_{ij_z} r_{ij_x}}{r_{ij}^2} & \frac{3r_{ij_z} r_{ij_y}}{r_{ij}^2} & \frac{3r_{ij_z}^2}{r_{ij}^2} - 1 \end{bmatrix} , \tag{3.4}$$

V is the volume of the grain, r_{ij_α} is the displacement between grains i and j, with the subscript $\alpha = x, y, z$ denoting the component of the displacement. As W_{ij} is dependent only on the position and size of the grains this matrix can be determined prior to simulation internally or via a separate external code. Improved methods to determine the W matrix are available but these produce additional computational cost. One such method is surface charge integration as discussed in [61]. MARS is capable of accepting the W matrix as an input enabling fast implementation of alternative methods for magnetostatic determination.

3.3.3 Anisotropy field

The temperature dependence of $\mathbf{H}_{\text{ani}}^i$ is described using the following expression:

$$\mathbf{H}_{\text{ani}}^i(T) = \frac{2K_u^i}{M_s^i}(m^i(T))^{\eta-1}\left(\mathbf{m}^i \cdot \hat{e}^i\right)\hat{e}^i \, , \tag{3.5}$$

where $\hat{e}^i$ is the unit vector aligned along the easy axis, K_u^i is the anisotropy and M_s^i is the zero temperature saturation magnetisation of grain i. Here we exploit the fact that we can express the temperature dependence of K_u via the dependence on the magnetisation m described via Callen-Callen scaling [62], which allows $K_u(T)$ to be expressed as:

$$K_u^i(T) = K_0^i(m^i(T))^\eta \, . \tag{3.6}$$

K_0 is the anisotropy energy density at 0 K and η is determined via experiment or atomistic parameterisation. Typically the exponent $\eta = 3$ for uniaxial anisotropy and $\eta = 2$ for 2-site anisotropy appropriate for FePt [63].

As temperatures approach and exceed the Curie point, Eq. 3.5 produces a fictitious longitudinal component of the anisotropy. This leads to a reduction in the longitudinal relaxation of the magnetisation as a function of temperature. To overcome this issue the anisotropy field can also be described as a function of the transverse susceptibility $\chi_\perp$ [27]:

$$\mathbf{H}_{\text{ani}}^i = \frac{-(m_x^i \hat{x} + m_y^i \hat{y})}{\chi_\perp} \, , \tag{3.7}$$

where m_x^i and m_y^i are the components of the reduced magnetisation vector and $\hat{x}$, $\hat{y}$ are the unit vector along these directions, respectively. Unlike Eq. 3.5 this form of the anisotropy assumes that the easy axis lies along the z-axis however it is valid for all temperature ranges and is therefore the most suitable description for LLB applications. For soft materials the determination of $\chi_\perp$ is extremely challenging and thus both forms of the anisotropy are available for use with the LLB solver to enable the simulation of both hard and soft materials.

3.4 Atomistic parameterisation

The granular model requires characterisation of the temperature dependence of the magnetisation, anisotropy and susceptibilities. These quantities are obtained via fitting of atomistic data, obtained using the VAMPIRE software package [14]. A key benefit of atomistic parameterisation is the improved accuracy of the modelled material's behaviours as well as the ability to simulate granular systems which include a segregant between the grains as is typically the case in recording media. There are two available methods for fitting the magnetisation. The first is fitted according to

$$m(T) = M(T)/M_s = (1 - T/T_c)^{\beta} \ , \tag{3.8}$$

where M_s is the spontaneous magnetisation and β is the critical exponent. The second is fitted via a more complex polynomial, with fitting parameters A and B, in powers of $(T - T_c)/T_c$:

$$m(T) = \begin{cases} \sum_{i=0}^{9} A_i \left(\frac{T_c - T}{T_c} \right)^i + A_{1/2} \left(\frac{T_c - T}{T_c} \right)^{\frac{1}{2}} & , \text{ if } T < T_c \\ \left[\sum_{i=1}^{2} B_i \left(\frac{T - T_c}{T_c} \right)^i + A_0^{-1} \right]^{-1} & , \text{ otherwise.} \end{cases} \tag{3.9}$$

Both methods are capable of producing the characteristic behaviour of the temperature dependent magnetisation. A comparison of these two methods is given in Fig. 3.9. For bulk systems a strong criticality is expected and the critical exponent fit reproduces the sharp transition to zero magnetisation at the Curie point. However, as grain sizes decrease finite size effects become significant which cause a reduction in the criticality of the transition. The result of finite size effects is a small but non-zero magnetisation above the Curie point. The polynomial fit is capable of reproducing this behaviour and provides greater agreement with atomistic data for small grains (i.e. 5 nm) than the critical exponent fit.

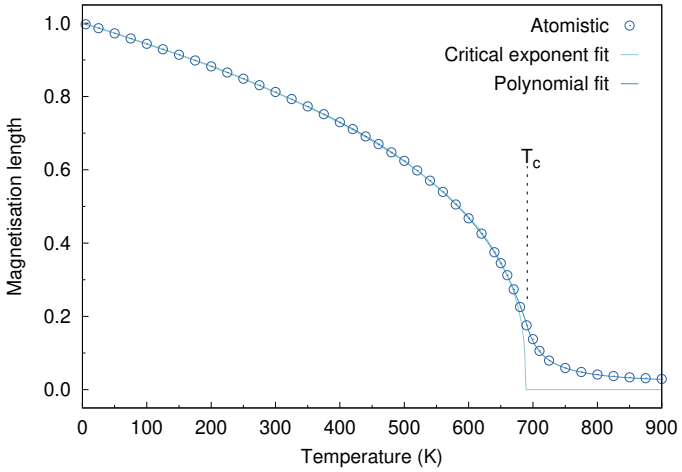

Fig. 3.9 Comparison of the fittings of the magnetisation achieved for a 5 nm grain via the two available methods implemented in MARS. The dots represent the atomistic data, while the lines show the fits.

The susceptibility χ is a measure of the strength of the fluctuations of the magnetisation. The components of the susceptibility, according to the spin fluctuation model, can be obtained by the fluctuations of the same magnetisation components as follows [64]:

$$\tilde{\chi}_\alpha = \frac{\mu_s N}{k_B T}\left(\langle m_\alpha^2\rangle - \langle m_\alpha\rangle^2\right), \tag{3.10}$$

where $\tilde{\chi}_\alpha = \chi_\alpha / M_s V$ is the reduced susceptibility and is in units of field^{-1}. N is the number of spins in the system with magnetic moment μ_s. Here $\langle m_\alpha\rangle$ is the ensemble average of the reduced magnetisation component $\alpha = x, y, z$ and longitudinal. Longitudinal describes the length of the magnetisation, while x, y, z are the spatial Cartesian components of the magnetisation. $\tilde{\chi}_\parallel$ describes the strength of the fluctuations of the magnetisation component along the easy-axis direction, which for our system is z. $\tilde{\chi}_\perp$ refers to the fluctuations orthogonal to the easy axis and thus on the x-y plane. For $\tilde{\chi}_\parallel$ and $\tilde{\chi}_\perp$, we use a similar approach to Ellis [64] and we fit the inverse of the susceptibility $1/\tilde{\chi}_{\parallel,\perp}$:

$$\frac{1}{\tilde{\chi}_{\parallel,\perp}} = \begin{cases} \sum_{i=0}^{9} C_i \left(\frac{T_c - T}{T_c}\right)^i + C_{1/2}\left(\frac{T_c - T}{T_c}\right)^{\frac{1}{2}} & \text{, if } T < T_c \\ \sum_{i=0}^{4} D_i \left(\frac{T - T_c}{T_c}\right)^i & \text{, otherwise,} \end{cases} \tag{3.11}$$

where C_i and D_i are the fitting parameters and T_c is the Curie point, obtained by determining the temperature at which the parallel susceptibility diverges. Figure 3.10 shows the susceptibilities

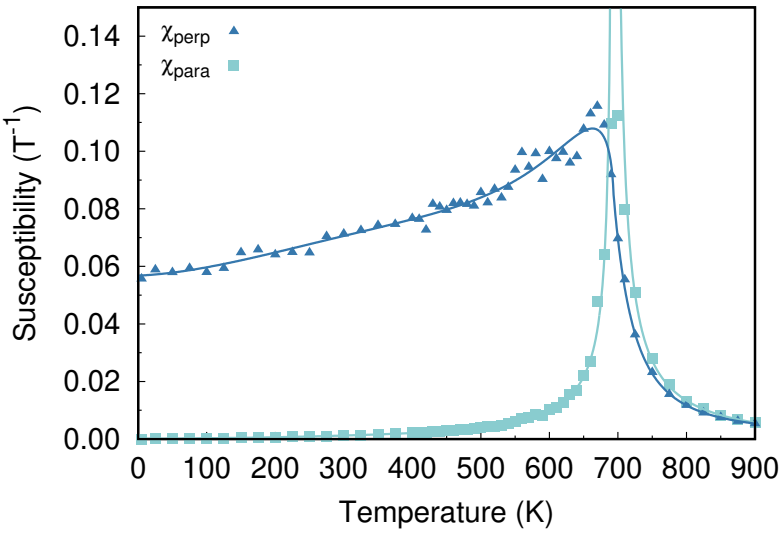

Fig. 3.10 Fit obtained for parallel and perpendicular susceptibility using the inverse method similar to that of Ellis [64]. The Curie point of this system is the temperature at which the parallel susceptibility diverges, which for this data is 685.14 K

and fits obtained from atomistically parameterised FePt, the Curie point of this system is 685.14 K.

Low anisotropy systems and systems of reduced dimensions cannot retain the alignment of the magnetisation along the easy axis up to T_c. In such cases $\tilde{\chi}_{\parallel}$ is a mix of the spatial components and becomes difficult to determine. A workaround is to avoid calculating $\tilde{\chi}_{\parallel}$ directly and to obtain $\tilde{\chi}_{\parallel}$ from $\tilde{\chi}_{l}$, following the discussion presented in [65]. Unfortunately a similar method cannot be used for $\tilde{\chi}_{\perp}$ making it difficult to determine the anisotropy for soft systems when the anisotropy field is given by Eq. 3.7.

Alternatively, if the anisotropy field is described as in Eq. 3.5, the reduced anisotropy is given by Eq. 3.6, as discussed by Callen-Callen [62]. MARS implements both a standard Callen-Callen fitting and an extended version. The extended version utilises three temperature regions each with their own fit parameters such that there are no discontinuities. This extended fitting method enables greater accuracy in the reproduction of the anisotropy as a function of temperature. This approach should provide more useful results in the case of soft materials, where extracting $\tilde{\chi}_{\perp}$ can prove difficult. Figure 3.11 is a comparison of the fits obtained using the standard and extended Callen-Callen fitting methods. Once all these parameters are determined, the granular model is fully parameterised regarding the material properties.

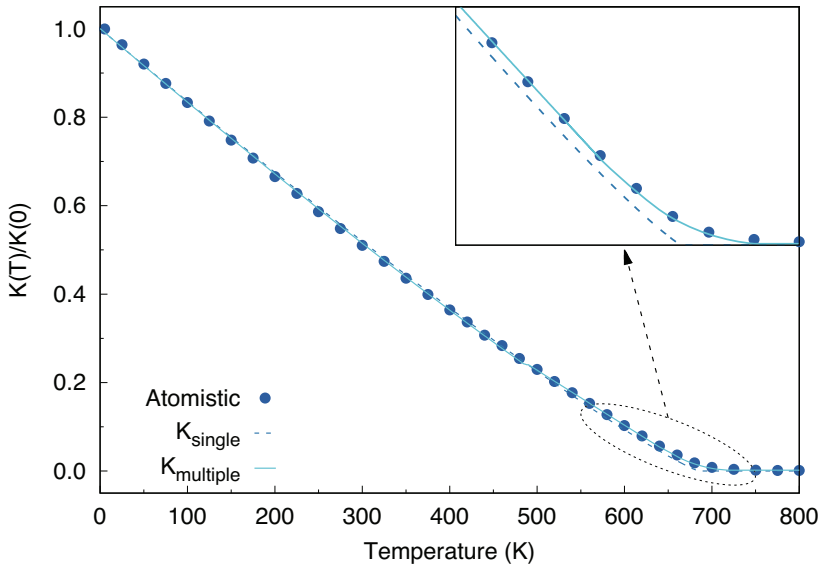

Fig. 3.11 Comparison of the fit achieved via the standard (single) and extended (multiple) Callen-Callen methods. The points represent the atomistic simulation data while the lines show the fits used in MARS. The extended Callen-Callen is able to provide an improved fit overall and especially near the Curie point as shown in the inset.

3.5 Curie temperature dispersion

The HAMR process involves heating through T_c which, as a result, becomes an important material parameter. More particularly, simulations by Li and Jhu [66, 67] have shown that the dispersion of T_c is a serious limitation for the ultimate storage density achievable for HAMR. Here we consider an irreducible contribution to the dispersion of T_c which arises directly from the diameter dispersion. It is well known that finite size effects lead to a reduction of T_c, demonstrated experimentally for FePt by Rong et al. [11]. A theoretical investigation based on an atomistic model by Hovorka et al. [68] showed that the variation $M(T)$ was well described by the finite size scaling law

$$T_c(D) = T_c^{\infty}(1-(d_0/D)^{\psi}) \,, \tag{3.12}$$

where ψ is the so-called phenomenological shift exponent and d_0 is the microscopic length scale close to the dimension of a unit cell of the lattice structure. The exponent ψ is related to the correlation length universal critical exponent ν and it is expected that $\psi = \nu^{-1}$. However, small grains can exhibit departure from universality so we prefer the form of Eq. 3.12 as a functional form to represent the diameter dependence of T_c. Clearly a dispersion of diameter maps onto the dispersion of T_c. Assuming a log-normal distribution of D, with logarithmic

mean D_m and variance σ_D^2 it has been shown [68] that the dispersion of T_c is given by the distribution function

$$f_T(\Delta T_c) = \frac{1}{\sqrt{2\pi}\Delta T_c \sigma_T} \exp\left(-\frac{(\ln \Delta T_c - T_m)^2}{2\sigma_T^2}\right), \tag{3.13}$$

with $\Delta T_c = T_c^{\infty} - T_c$. Eq.(3.13) is a log-normal distribution function with logarithmic mean $T_m = \psi(\ln(d_0(T_c^{\infty})^{1/\psi}) - D_m)$ and variance $\sigma_T^2 = \psi^2 \sigma_D^2$. Through Eq. 3.12, with d_0, ψ and T_c^{∞} determined either from experiment or atomistic model calculations, a T_c value can be assigned to an individual grain and Eq. 3.13 used to calculate the standard deviation of the T_c dispersion.

3.6 Validation

In order for MARS to be capable of simulating novel materials and systems it must first be tested and verified. The process used for testing followed a step-wise manner, whereby the model starts greatly simplified and is then increased in complexity as tests are successfully completed. The first stage of validation begins with testing the underlying numerical integration scheme.

3.6.1 Verification of the Heun scheme

To verify the implementation of the dynamic solver one starts with a simplified deterministic model which can be solved analytically. This model consists of a single isotropic particle, thus removing the preferential directional alignment of the magnetisation, leaving the magnetisation to be influenced only by the external field. By applying an external field of magnitude H, parallel to the z-axis the equation of motion can be solved analytically. For the LLG the resultant solution is:

$$\begin{aligned} M_x(t) &= \operatorname{sech}\left(\frac{\gamma\alpha H}{1+\alpha^2}t\right)\cos\left(\frac{\gamma H}{1+\alpha^2}t\right) \\ M_x(t) &= \operatorname{sech}\left(\frac{\gamma\alpha H}{1+\alpha^2}t\right)\sin\left(\frac{\gamma H}{1+\alpha^2}t\right) \\ M_z(t) &= \tanh\left(\frac{\gamma\alpha H}{1+\alpha^2}t\right). \end{aligned} \tag{3.14}$$

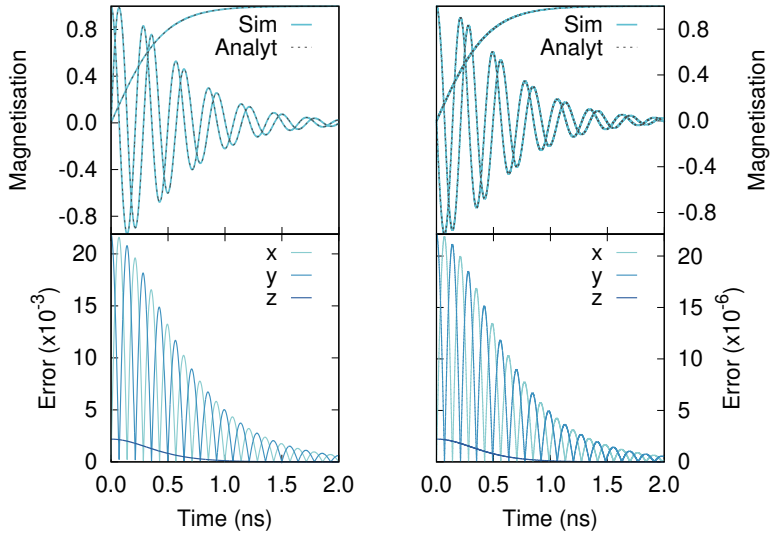

Fig. 3.12 Comparison of the numerical simulation and analytical solution for the LLG (left) and LLB (right) solvers. Both systems are in the presence of a 400π *Oe* field and the timesteps of integration used are $\Delta t = 1$ ps for the LLG and $\Delta t = 1$ fs for the LLB.

The LLB requires a separate derivation which has the resultant form:

$$\begin{aligned} M_x(t) &= \operatorname{sech}\left(\frac{\gamma\alpha_\perp Ht}{m^2}\right)\cos(\gamma\alpha_\perp Ht) \\ M_y(t) &= \operatorname{sech}\left(\frac{\gamma\alpha_\perp Ht}{m^2}\right)\sin(\gamma\alpha_\perp Ht) \\ M_z(t) &= \tanh\left(\frac{\gamma\alpha_\perp Ht}{m^2}\right). \end{aligned} \tag{3.15}$$

The time evolution for the LLG and LLB along with the obtained errors are shown in Fig. 3.12. The maximum error obtained for the LLG is of the order 10^{-2}, while for the LLB it is of the order 10^{-5}. The difference in the magnitudes of the errors arises due to the different required minimum timesteps. The LLB requires a minimum timestep of 1 fs while the LLG can utilise up to 1 ps. The form of these errors is characteristic of a correctly implemented Heun integration scheme.

3.6.2 Angular dependence of the coercivity

Verification of the implementation of the uniaxial anisotropy for all solvers is performed via a simple test which makes use of the Stoner-Wohlfarth model. Here, the Stoner-Wohlfarth particle describes the behaviour of a single grain at zero Kelvin under the influence of an

applied field. The angular dependence of the coercivity is very well known [37] and thus makes a very useful property for comparison and verification of a code. This test verifies the deterministic behaviour of the LLG and LLB by ensuring the easy axis profile provides a coercivity of $H_k = \frac{2K_u}{M_s}$ as is known analytically.

The grain is initially magnetised along the z-axis and the applied field strength is varied from $H = 1.5H_k$ to $H = -1.5H_k$ and back, in steps of $0.005H_k$. This process is repeated for a range of field directions ranging from 90° to 0°. The projection of the magnetisation on the field direction is then plotted as a function of the applied field strength as shown in Fig. 3.13 for the LLG, LLB and kMC solvers. As expected the same profiles are obtained irrespective of which of the three solvers are used and these profiles also agree exactly with those of Stoner and Wohlfarth's solution.

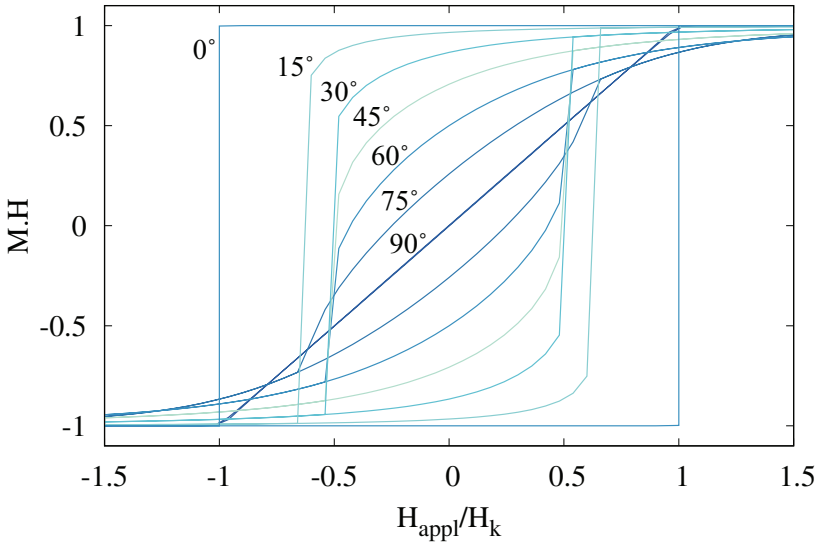

Fig. 3.13 Alignment magnetisation for a single grain under an applied field for various angles from the easy axis. The 0° and 90° profiles are simulated with a small deviation from the labelled value. This is done as at perfect alignment, in the absence of thermal noise, there is zero torque which prevents any change in the magnetisation alignment.

3.6.3 Boltzmann distributions for an ensemble of non-interacting grains

To verify the stochastic behaviour of the LLG and LLB solvers a test which utilises thermal effects is required. The most simple test available is the reproduction of the Boltzmann distribution for an ensemble of non-interacting grains, with uniaxial anisotropy in the absence of an applied field. The Boltzmann distribution for magnetisation as a function of polar angle

Table 3.1 Parameters used for the anisotropy temperature dependence for the LLG Boltzmann test.

	Low temperature region	Middle temperature region	High temperature region
Temperature range (K)	$T < 475$	$475 < T < 650$	$T > 650$
η	3.07	2.44	1.87
Pre-factor	0.997	0.749	0.379

for the LLG is simple to obtain and is given by:

$$P(\theta_m) = \frac{\sin(\theta_m)\exp\left(-\frac{K_u V \sin(\theta_M)^2}{k_B T}\right)}{\int_0^{\pi/2}\sin(\theta_m)\exp\left(-\frac{K_u V \sin(\theta_m)^2}{k_B T}\right)d\theta_m}, \tag{3.16}$$

where θ_m is the angle of magnetisation with respect to the easy axis. The ensemble is first allowed to equilibrate over 1 ns after which the ensemble is evolved over time for 10^6 steps with the angle of magnetisation recorded at each step. The results obtained by the LLG and the analytical solution are shown in Fig. 3.14 for an initial magnetisation direction parallel to the easy axis direction. The grains were all identical with a volume of $108 \cdot 10^{-21}$ cm^3 and a zero Kelvin uniaxial anisotropy energy density of $9.23 \cdot 10^7$ erg/cm^3. The anisotropy temperature scaling was modelled using multi-range Callen-Callen scaling with the parameters listed in Table 3.1. There is excellent agreement between these results, showing correct implementation of thermal effects in the LLG.

For the LLB equation the free energy of the system is defined as [69, 34]:

$$\frac{F}{M_S^0 V} = \begin{cases} \dfrac{m_x^2 + m_y^2}{2\tilde{\chi}_\perp} + \dfrac{(m^2 - m_e^2)^2}{8\tilde{\chi}_\parallel m_e^2}, & \text{if } T \leq T_c \\ \dfrac{m_x^2 + m_y^2}{2\tilde{\chi}_\perp} + \dfrac{3}{20\tilde{\chi}_\parallel}\dfrac{T_c}{T - T_c}\left(m^2 + \dfrac{5}{3}\dfrac{T - T_c}{T_c}\right)^2, & \text{otherwise} \end{cases} \tag{3.17}$$

where the first term provides uniaxial anisotropy and the second controls the magnetisation length. The expected Boltzmann distribution is of the form:

$$P(|m|) \propto m^2 \exp\left(-\frac{F}{k_B T}\right). \tag{3.18}$$

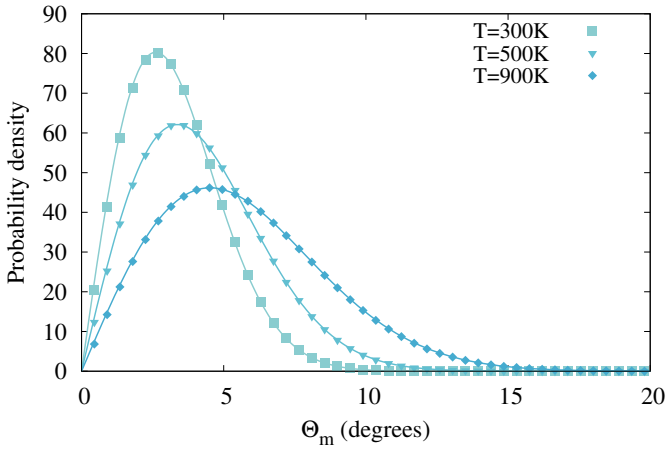

Fig. 3.14 Angular probability distributions for a non-interacting ensemble of grains with uniaxial anisotropy for 300 K, 500 K and 900 K. The analytical Boltzmann distributions are represented by the solid lines, the simulated data is represented by points.

Probability distributions along m_z and m_x for different temperatures along with the corresponding analytical solutions are plotted in Fig. 3.15, all results show strong agreement with the analytical solutions. The simulated system has an initially uniformly distributed magnetisation, a Curie point of 685.14 K, a grain volume of $108 \cdot 10^{-21}$ cm^3 and an anisotropy energy density at zero Kelvin of $9.23 \cdot 10^7$ erg/cm^3. The temperature dependence of the anisotropy is described via the perpendicular susceptibility via Eq. 3.7 with the susceptibility fitting parameters used in Eq. 3.11 given in Table 3.2. The system was evolved over time for 1 ns (10^6 steps). The results show the ability of the implemented LLB solver to describe the loss of ferromagnetic behaviour as the temperature approaches and exceeds the Curie point, indicated by the formation of a single peak once the temperature exceeds the Curie point.

3.6.4 Determination of the Curie temperature

The LLG conserves magnetisation length, assuming unity for all temperatures, thus the model starts to break down at temperatures approaching T_c. The LLB allows for variable magnetisation lengths enabling it to simulate systems at and beyond their Curie points. This test was devised to verify the treatment of the magnetisation length by the LLB. The temperature dependence of the magnetisation is determined via parameterisation obtained using atomistic simulations. While the temperature dependence of the magnetisation is dependent on the Curie point alone, the method used to describe the anisotropy field can affect the magnetisation length.

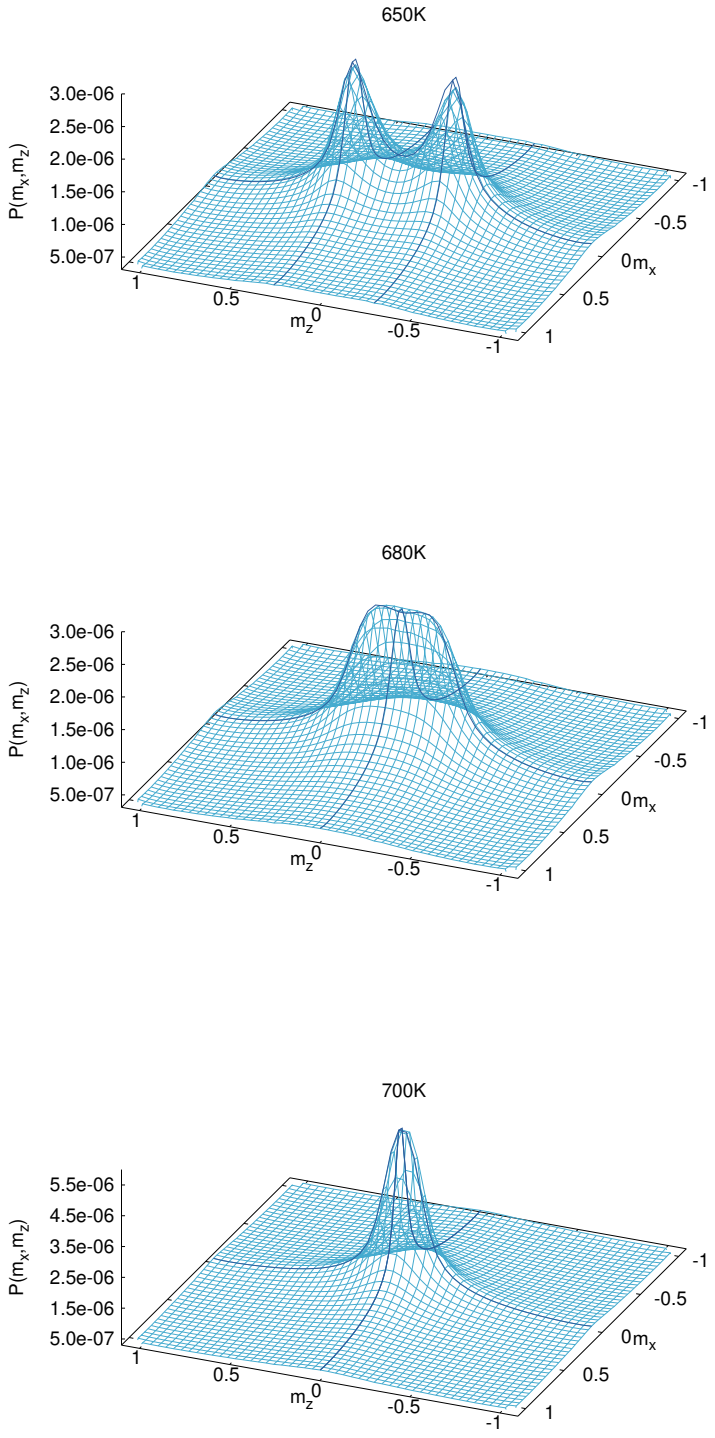

Fig. 3.15 Anisotropic distributions of magnetisation as functions of m_x and m_z (light blue grid) compared to analytical solutions for slices of m_y (dark blue lines) for 650 K, 680 K and 700 K.

Table 3.2 Fitting parameters for the parallel and perpendicular susceptibilities and magnetisation used for the LLB Boltzmann test.

	m	$1/\tilde{\chi}_{\parallel}(T)$	$1/\tilde{\chi}_{\perp}(T)$
c_0	0.1876	0.0	14.211
c_1	4.044	165.98	-106.96
c_2	-16.73	3631.6	2374.8
c_3	57.63	-10003	-17844
c_4	-130.8	15553	71355
c_5	183.6	-5713.5	-16675
c_6	-146.5	0.0	234979
c_7	51.37	0.0	-196703
c_8	3.971	0.0	90149
c_9	-5.585	0.0	-17439
$c_{1/2}$	-0.1918	43.892	-16.575
d_0		0.0	14.359
d_1	87.66	494.78	162.86
d_2	-72.19	-1637.8	3014.6
d_3		12815	-8814.1
d_4		-21393	10732

As explained in Section 3.3.3 the Callen-Callen scaling produces a fictitious longitudinal component of the magnetisation at temperatures exceeding the Curie point. This fictitious component reduces the criticality of the magnetisation length resulting in disagreement with atomistic simulations. The use of the perpendicular susceptibility described by Eq. 3.7 does not introduce a fictitious component and thus correctly produces the magnetisation length. As a result the susceptibility method should be preferred over Callen-Callen scaling for simulations near a system's Curie point. However, obtaining the susceptibility of soft magnetic materials is not trivial [65] and thus the Callen-Callen method provides some ability to model soft magnetic materials in the absence of a well defined perpendicular susceptibility. To verify the treatment of the magnetisation length for both methods of modelling the anisotropy temperature dependence, two systems were simulated, one hard and the other soft. The hard was modelled using the perpendicular susceptibility, while the soft material was modelled using Callen-Callen scaling. The systems are heated from 0 K to above the highest Curie point of the materials. At each temperature the system is simulated until an equilibrium is reached at which point the magnetisation is recorded and the temperature increased. Figure 3.16 shows the results obtained for the hard and soft materials via LLB simulation compared to those obtained by atomistic simulation. There is excellent agreement between the results, showing that MARS is capable of reproducing the correct behaviour

of the magnetisation length and also that the Callen-Callen scaling method is applicable at temperatures near the Curie point for soft materials.

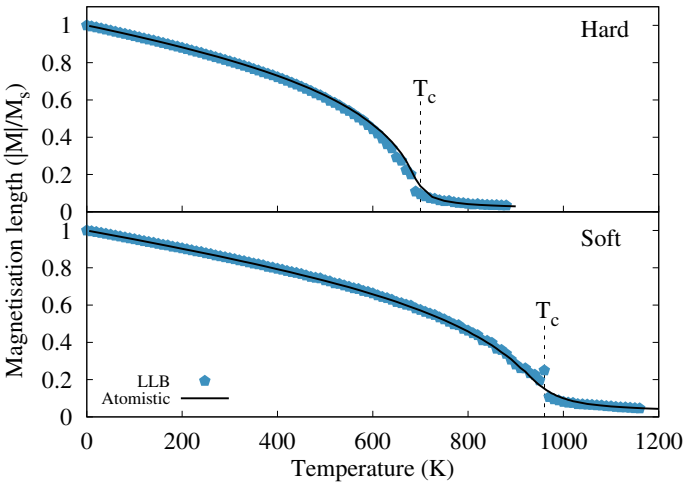

Fig. 3.16 Magnetisation as a function of temperature for the hard and soft materials performed using LLB solver.

3.6.5 Longitudinal relaxation

A system of non-interacting identical grains is initially aligned at 30° from the z-axis, placing it in a non-equilibrium state. The system is then allowed to thermally relax, in the absence of an applied field, for a range of system temperatures and the magnetisation length is recorded at each step. Figure 3.17 shows the comparison of the results obtained via MARS and atomistic simulations. The results show excellent agreement. As expected there is a small discrepancy for very short timescales where the rate of relaxation is greatest [69], however, both results show identical equilibrium lengths within only 5 ps.

3.6.6 Coercivity as a function of sweep rate

In the presence of thermal effects the coercivity depends on the applied field sweep rate. The coercivity as a function of the sweep rate was determined empirically by Sharrock [70] and then derived theoretically by Chantrell [71] under the assumption of constant attempt frequency and an easy axis parallel to the applied field. A simple test for the kMC solver consists of the simulation of hysteresis profiles for a range of sweep rates. Figure 3.18 shows the comparison between the simulated results and the theoretical prediction. The results agree strongly with the theory verifying the implementation of the kMC for thermal systems.

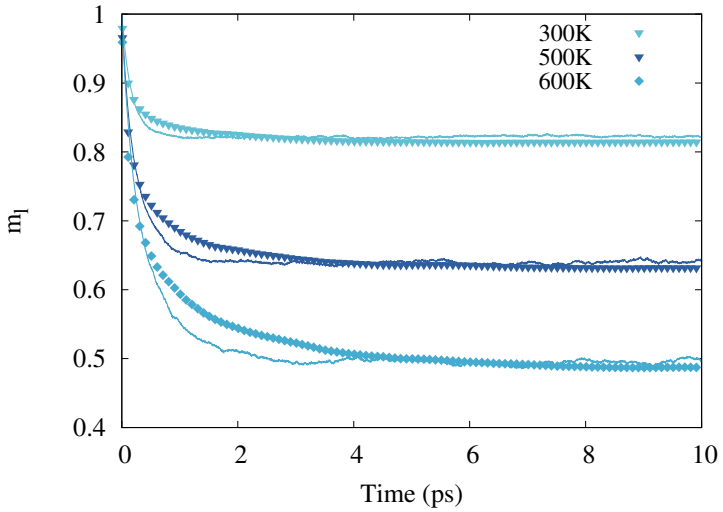

Fig. 3.17 Comparison of micromagnetic (lines) and atomistic (dots) results of the magnetisation length as a function of time, for a system undergoing thermal relaxation. The Curie temperature of the simulated system is 680K.

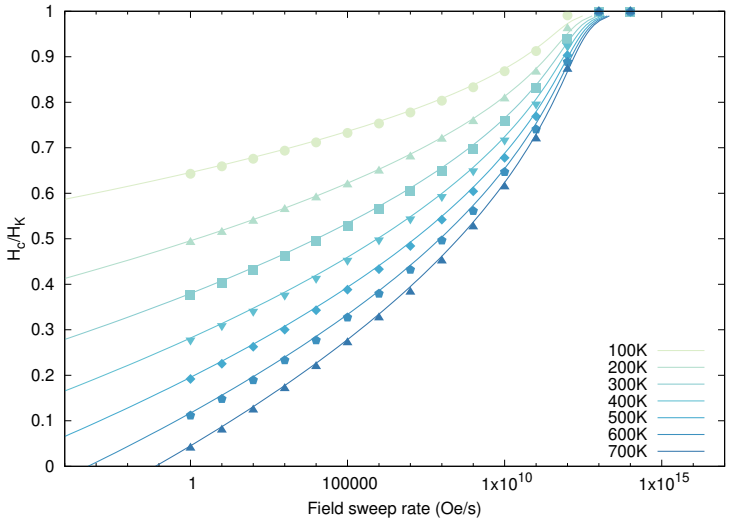

Fig. 3.18 Coercivity as function of applied field sweep rate for the easy axis aligned with the field for various temperatures $100K$ to $700K$. The simulation results (dots) show good agreement with the theoretical prediction (lines).

3.6.7 HAMR dynamics

The final test of the MARS code is the simulation and comparison of HAMR dynamics obtained with MARS and atomistic simulation. A detailed description of the parameterisation, methodology and further results can be found in [72]. For this test a single $5 \times 5 \times 10\,\mathrm{nm}^3$ FePt grain was simulated for a range of peak pulse temperatures, T_{peak}, and pulse lengths, t_{pulse}, for an applied field strength of 500 Oe and 1,000 Oe. Each simulation was repeated one hundred times to ensure a large enough statistical ensemble. The integration steps used for the atomistic simulations were 0.1 fs to ensure convergence of the results. The micromagnetic LLB simulations used 1 fs integration steps.

While the atomistic simulations were performed for a single grain each, the micromagnetic simulations were performed for a single system of one hundred non-interacting grains. Furthermore the micromagnetic simulations were around fifteen times faster than the single grain atomistic simulations. Overall the micromagnetic simulations provide a hundred times greater performance than the atomistic simulations for this system. Figure 3.19 shows the obtained phase plots for the switching probability as a function of both pulse peak temperature and pulse length. The peak temperature and pulse times were varied in steps of 12.5 K and 50 ps respectively. Both sets of results show excellent agreement between the micromagnetic and atomistic results, verifying the ability to model HAMR systems with LLB dynamics.

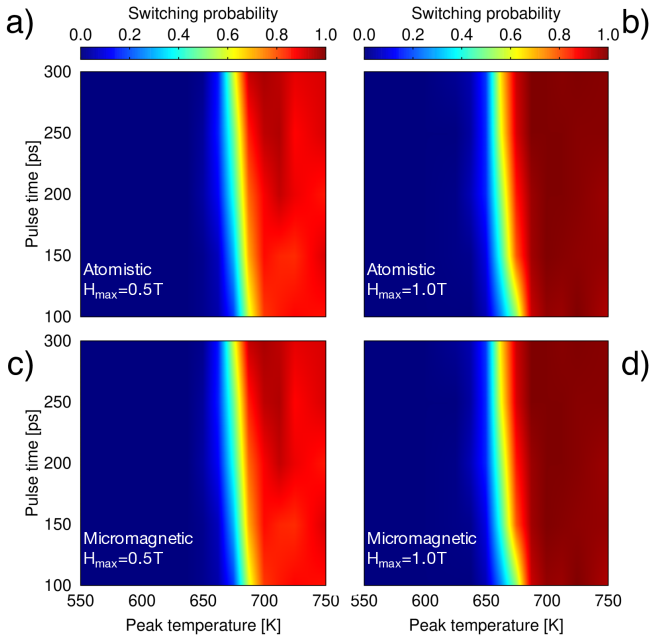

Fig. 3.19 Plot of the switching probability for a single $5 \times 5 \times 10\,\mathrm{nm}^3$ hexagonal grain of FePt as a function of pulse duration and pulse peak temperature for 500 Oe (a and c) and 1,000 Oe (b and d) applied fields for atomistic (a and b) and micromagnetic (c and d).

3.7 Summary

An open-source multi-scale multi-timescale micromagnetic code (called MARS) for simulating granular thin films has been developed. The primary focus of the MARS code is to enable detailed modelling and simulation of state of the art and future magnetic recording technologies, covering both the short timescale writing/reading processes and long timescale data storage. A custom method for generating granular structures via a Laguerre-Voronoi tessellation has been developed and implemented for MARS. This implemented method has been shown to greatly improve the accuracy of the generated granular structures with an almost total removal of the unrealistic highly angular grains which are common with standard Voronoi tessellations. Furthermore the implemented method has been shown to be highly capable of generating log-normally distributed grain sizes. The key functionality of MARS is provided via the development and inclusion of three micromagnetic solvers: the Landau-Lifshitz-Gilbert, Landau-Lifshitz-Bloch and kinetic Monte Carlo. Short timescale simulations are possible via the LLG and LLB dynamic solvers, with long timescale simulations performed via the kMC solver. The inclusion of the LLB solver enables simulation of systems at and exceeding their Curie points, a crucial feature for simulating advanced recording systems such as HAMR. The presence of three micromagnetic solvers has also been utilised to enable automatic solver selection and dynamic switching based on the system's time scale and temperature.

The multi-scale nature of MARS is achieved via material parameterisation. While the parameterisation can be obtained from experimentation the recommended method is via atomistic simulation. A detailed description of the parameters obtained via atomistic parameterisation has been given. Descriptions of the numerous fitting functions employed for the various temperature dependent parameters along with their specific use cases have also been provided. Finally extensive testing of the MARS code has been performed. The importance of these tests has been explained along with the specific functionality they validate. As a result every aspect of MARS has been verified with the final test showing MARS producing excellent agreement with atomistic simulations while also greatly outperforming the atomistic simulations for a HAMR like write process for an ensemble of grains.

4

Semi-analytical model of switching probabilities for the determination of Curie point distributions

HAMR takes advantage of the thermal dependence of magnetic properties by applying heat pulses near to the material's Curie point in order to enable data writing to high coercivity materials. As a result of this the Curie point dispersion is a key parameter in the development and optimisation of HAMR technology [73, 74, 66]. The ability to demagnetise grains is directly related to the grain temperature and Curie point and any variations in either can result in reduced performance [75]. A clear example of the importance of Curie point distributions can be seen in the presence of transition jitter. Transition jitter is a measure of the accuracy of the placement of the bit transitions. Variations in the anisotropy, Curie point or grain temperature can result in different switching probabilities which lead to variations in the sharpness of the bit transitions, creating transition jitter. Broadening of the bit transitions severely impacts the linear density of HAMR technologies [67] hindering the progression of the technology towards to development of high density drives with areal densities exceeding $2\,\mathrm{TB/in^2}$. Wang et al. derived an expression to determine transition jitter which shows a strong dependence on the Curie point dispersion [76].

The cause of the transition shift arising from Curie point distributions is the same as that arising from grain-to-grain temperature variations. The transition is expected to occur when the grains reach the recording temperature. HAMR devices are designed such that this recording temperature is reached within a specific range of the near-field transducer (NFT). The write field is then located such that the grains are magnetised as the material cools ensuring that the desired magnetisation is locked in once the temperature falls below the recording temperature. The recording performance is highly dependent on the switching time window, the time during which the material can be magnetised [43]. A shift in the recording temperature of a grain results in the grain being able to switch at a different distance from the

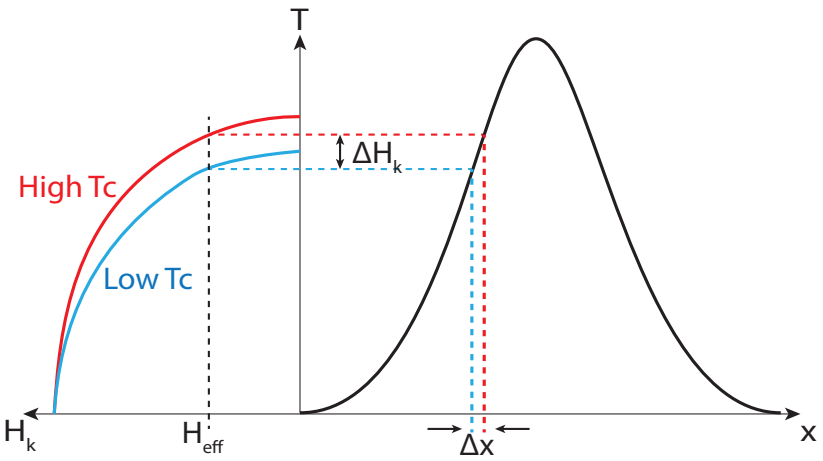

Fig. 4.1 Illustration of transition position shift due to Curie point variations. The left side shows the variation of coercivity as a function of temperature. The right side shows the temperature profile along the down track direction. At the write field, H_{eff}, the coercivity is different between the grains due to the Curie point difference. This difference in coercivity translates to a shift in transition position based on the temperature profile of the system as shown on the right hand side. Reproduced from [43].

NFT, resulting in a different switching time window. Figure 4.1 illustrates how a variation in Curie point can create a difference in the recording temperature leading to a shift the transition position.

There have been numerous methods proposed to determine Curie point distributions [77–80]. Chernyshov et al. have proposed a method to utilise thermo-remanence measurements in order to observe anisotropy field and Curie point distributions via magnetisation erasure experiments [78]. Thermo-remanence refers to the process of magnetising/demagnetising a system via the application of heat with the magnetisation measured once the system has returned to room temperature. Unfortunately it is not possible to obtain the Curie point distributions via these experiments alone. A computational model is required to act as a fitting function to extract the parameter distributions from the obtained experimental results. This chapter details the development of a semi-analytical model to act as a fitting function for a thermo-remanence experimental procedure which follows more closely to the HAMR process than that used by Chernyshov et al. with the aim of extracting Curie point distributions from experimental data. This chapter covers the simulation of thermo-remanence via the MARS code, followed by the development of a semi-analytical model which has then been used to determine Curie point distributions via a grid search combined with a χ^2 goodness of fit measurement.

4.1 Simulation methodology

The experimental procedure these simulations are designed to model is as follows. The magnetically saturated recording medium is placed on a spin stand with a laser positioned to allow for a small area of the material to be heated. The size of the heated spot is sufficient to make the influence of grains outside of the spot, due to interactions, negligible. As the material is rotated the laser is pulsed at different peak temperatures and a magnetic field is applied. The magnetic field is set anti-parallel to the initial magnetisation of the system with the aim of switching the grains within the heated spot. The total duration for which the spot is heated is around 10 ms. The magnetisation of each heated spot of the material is measured once the spot has returned to its initial temperature.

To simplify the simulation process the entire granular structure is heated uniformly while the external field is applied. The heating process is simulated via the LLB solver, however due to the long time scales used in the experiments it is not feasible to perform the entire simulation with the LLB alone. By utilising the multiple micromagnetic solvers implemented in MARS it is possible to simulate the laser application for the entire experimental duration. This is achieved by performing the heating process via the LLB solver and then switching to the kMC solver once the system reaches the peak temperature. The kMC solver is used only when the total pulse application time exceeds 1 μs, for shorter pulses the LLB solver is used throughout. The timestep for the kMC is set such that one-hundred steps are required to simulate the pulse application. The solver is then switched back to the LLB to model the cooling process. Once the cooling process is completed the total magnetisation of the system is determined. Figure 4.2 shows the laser and field applications as a function of time for the thermo-remanence simulations.

This simulation must be performed for each pulse peak temperature, thus making the simulation process computationally expensive. This is especially true when parameter distributions are introduced as the simulated system must contain a sufficiently large number of grains to accurately describe the distributions. In general the number of simulations required to model a known system can range into the hundreds. The process of extracting distributions from experimental data requires numerous systems to be simulated and compared to the experimental results until a match is found within the specified confidence level. At this point it becomes unfeasible to use MARS as a fitting tool to extract parameters from experimental results. To overcome this issue a semi-analytical model has been developed. This model has a massively reduced computational cost enabling simulations to be performed significantly faster.

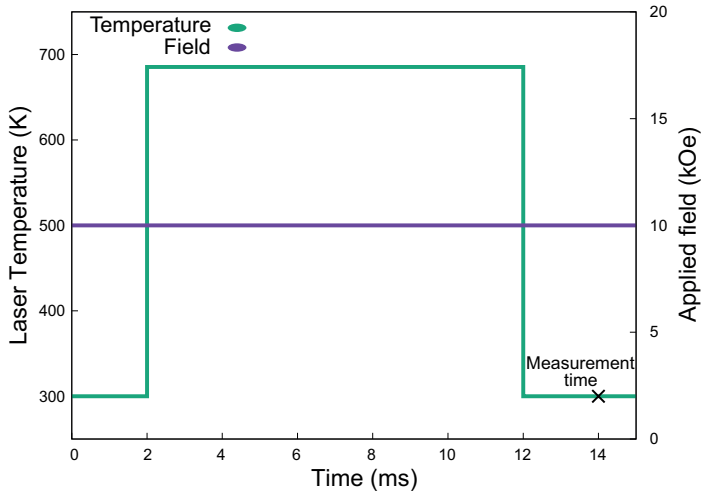

Fig. 4.2 Thermo-remanence temperature and field functions over time. The point at which the magnetisation is measured is indicated by the cross labelled measurement time.

4.2 Semi-analytical model

The analytical model is based on the probability of the magnetisation switching from one energy minimum to the other. The temperature dependencies of the saturation magnetisation and anisotropy are accounted for using Eq. 3.8 and Eq. 4.1.

$$K(T) = K_u(0)\left(\frac{M_s(T)}{M_s(0)}\right)^{\eta}, \tag{4.1}$$

where η is the Callen-Callen scaling power, $M_s(0)$ and $K_u(0)$ are the values of the M_s and K_u at zero Kelvin and T_c is the Curie temperature of the system.

In order to determine the probability for a reversal to occur one must first determine the energies required to overcome the energy barriers of the energy landscape. The energy landscape consists of two minima corresponding to the magnetisation lying parallel and anti-parallel to the applied field, these states are defined as 1 and 2 respectively. An illustration of the energy landscape is given in Fig. 2.2. The energy required to escape the initial minima, and reach the other is described by Eq. 2.34. The probability for reversal also depends on the time over which the reversal can occur. This is accounted for by the relaxation time τ which is determined via Eq. 2.36. The probability for reversal towards the applied field direction is given by Eq. 4.2, with Eq. 4.3 giving the probability for reversal away from the applied field.

$$P_{in}(t) = \frac{1.0 - exp[-t/\tau]}{1 + exp[-\frac{E_1 - E_2}{K_b T}]} \tag{4.2}$$

$$P_{out}(t) = \frac{1.0 - exp[-t/\tau]}{1 + exp[-\frac{E_2 - E_1}{K_b T}]} \tag{4.3}$$

When the system reaches the Curie temperature, T_c, the magnetisation becomes zero, as a result Eq. 4.2 and Eq. 4.3 equal 0.5 for $T > T_c$ as there is equal chance for the magnetisation to reside in either state. This behaviour creates a significant issue with determining the switching probability for pulse temperatures exceeding T_c as the final result will always be 50%. To overcome this issue the system must undergo a cooling phase, whereby the probability of reversal is calculated step-wise for the system, cooling from $T = T_c$ to $T = 300K$. This cooling is achieved by utilising Eq. 4.2 and Eq. 4.3 for each step with $t = \Delta t$ and temperature reduction of ΔT at each step. Evaluation of these equations needs to be performed only when $T < T_c$ as until this condition is met $P = 0.5$. For each step the probability of switching towards and against the field is determined, from these results the total probability for switching towards and against the field is obtained. The inclusion of this 'back-switching' is crucial as without this process the populations of the minimum will not satisfy the Boltzmann distribution. Detailed information about this requirement can be found in [41]. Figure 4.3 illustrates the cooling process as implemented in the semi-analytical model.

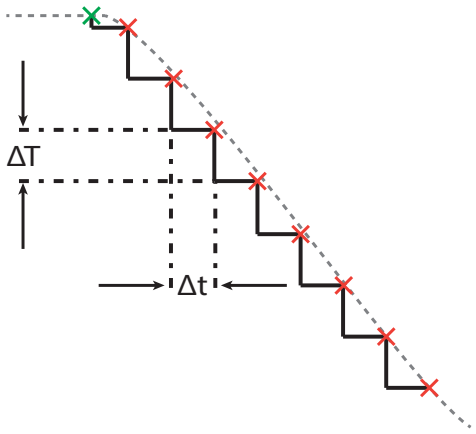

Fig. 4.3 Implementation of the cooling process in the semi-analytical model. The green cross is the initial calculation, for peak temperatures greater then the Curie point, the calculated probability will be 50%. The red crosses represent the subsequent calculations performed following the step-wise decrease of the system temperature. At this point the probability is determined and the cumulative switching probability is updated until the cooling is completed. The dotted grey line represented the real world temperature profile.

During the cooling process grains can switch into and out of the field direction at each step. First the switching probability is determined using Eq. 4.2 and Eq. 4.3 for the in field and out of field directions respectively. The initial probability is determined at the end of the

heat pulse prior to the cooling phase, this is indicated by the green cross in Fig. 4.3. This switching probability is used to determine the populations of the in field, B^0_{in}, and out of field, B^0_{out}, states. Each cooling step then includes three parts. First the switching probabilities are determined with $t = \Delta t$ and T equal to the corresponding pulse temperature at that cooling step, indicated by the red crosses in Fig. 4.3. Second the number of grains switching is determined, it should be noted this will not be equal to the probability due to the different populations of the two states due to the initial heat pulse. Finally the populations of the in field and out of field states are updated to account for the switching due to the current step. Step two and three are determined using Eq. 4.4.

$$\begin{aligned} A^i_{in} &= B^{i-1}_{out} P^i_{in} & A^i_{out} &= B^{i-1}_{in} P^i_{out} \\ B^i_{in} &= B^{i-1}_{in} - A^i_{out} + A^i_{in} & B^i_{out} &= B^{i-1}_{out} - A^i_{in} + A^i_{out} \end{aligned} \tag{4.4}$$

where P is the switching probability for the current cooling step, A is the number of grains switching during the cooling step and B is the population of the two states after the cooling step. The subscript denotes the direction of the magnetisation with respect to the field direction. The superscript indicates the current cooling step which starts at one. The number of grains switching, A, is determined by accounting for the state's population and the switching probability. The state populations are determined by summing the initial populations with the number of grains switching to and out of the respective states. Once the cooling is completed the final switching probability for the entire pulse application is given by B^i_{in} where i is equal to the number of cooling steps performed.

The cooling process involves numerous calculations and as a result contributes significantly to the computational cost of the model. In order to improve the efficiency of the code one can take advantage of the blocking temperature. The blocking temperature is the temperature at which the magnetisation becomes 'frozen in'. Once the system temperature falls below the blocking temperature the thermal energy is insufficient to drive thermally activated reversal and the magnetisation becomes constant. At this point the cooling process will provide no change of the magnetisation meaning that the cooling process can be terminated prior to reaching 300 K thus reducing the computational cost. This is implemented in the model via comparison of the switching probability at each step during the cooling phase. Once the probabilities fall to less than 10^{-6} for a number of consecutive steps the system is deemed to have reached the blocking temperature and the cooling phase is stopped.

Table 4.1 Parameters used for the initial testing of the semi-analytical model via comparison with results obtained via MARS using the LLG and LLB solvers.

Parameter	Value
Ms (emu/cm^3)	1,100.0
$\langle K \rangle$ (erg/cm^3)	$4.5 \cdot 10^7$
$\tilde{\sigma_K}$	0.0
$\langle D \rangle$ (nm)	5.0
$\tilde{\sigma_D}$	0.0
Thickness (nm)	10.0
T_c^{∞} (K)	780.0
H_{appl} (Oe)	4000.0

4.3 Initial verification and limitations

To aid the development of the semi-analytical model simulations were performed using the MARS software package. The results obtained via the semi-analytical model and MARS were compared to ensure a successful description of the system via the semi-analytical model. The parameters used for this initial testing are detailed in Table 4.1, the anisotropy and grain size are log-normally distributed. The pulse application time was set to 100 ns in order to allow for simulation of the entire process via the LLG and LLB solvers with no kMC steps required. Figure 4.4 shows the comparison between the numerical and semi-analytical switching probabilities. There is excellent agreement between the numerical and semi-analytical results for all pulse peak temperatures up to the Curie point of the system. However, once the pulse temperature exceeds the Curie point there is a divergence in switching probability between the LLG and LLB solvers.

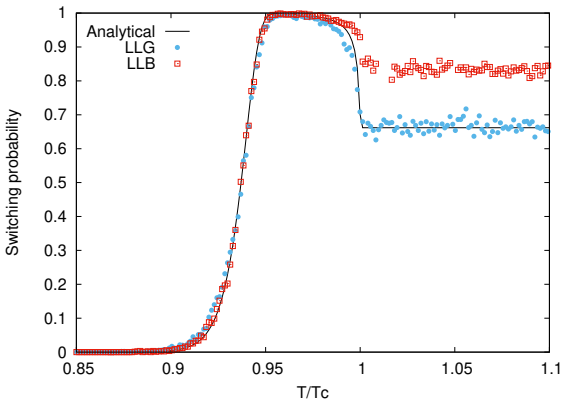

Fig. 4.4 Comparison between analytical model and results obtained via LLG/LLB simulations.

The divergence occurs due to a process called linear reversal. At temperatures close to and exceeding the Curie point the longitudinal relaxation of the magnetisation is sufficient to enable magnetic reversal with almost no transverse component of the magnetisation [64]. The transition between reversal mechanisms is gradual with the reversal process moving from circular to elliptical and then on to linear as temperatures are increased. This transition is driven by the variation of the susceptibilities with temperature. As $1/\tilde{\chi}_{\parallel}$ is proportional to the macroscopic longitudinal field of Eq. 2.30 and $1/\tilde{\chi}_{\perp}$ represents the anisotropy field, the ratio of $\tilde{\chi}_{\parallel}/\tilde{\chi}_{\perp}$ defines the transitions between reversal mechanisms [81]. At low temperatures (where $\tilde{\chi}_{\parallel}/\tilde{\chi}_{\perp} \lesssim 1/3$) the circular mechanism is dominant. When $\tilde{\chi}_{\parallel}/\tilde{\chi}_{\perp} > 1/3$ the elliptical reversal mechanism begins until $\tilde{\chi}_{\parallel}/\tilde{\chi}_{\perp} \approx 1/2$ afterwards linear reversal dominates. Figure 4.5 shows the reversal mechanisms for four different temperatures.

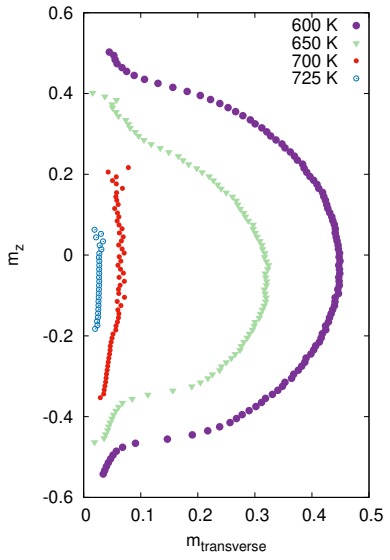

Fig. 4.5 Reversal paths for a system with a Curie point of 702.7 K for various applied temperatures. The change in magnitude of the z-component of the magnetisation between data sets arises due to the longitudinal relaxation of the magnetisation. The 600 K data set shows circular reversal where the magnitude of the magnetisation length is constant, this is the only available reversal mechanism when utilising the LLG solver. As the temperatures are increased the reversal path becomes elliptical until it is completely linear at 725 K.

The LLG solver can only account for circular reversal due to the constraint imposed on the magnetisation length, as previously explained in Chapter 2. The LLB solver is capable of accounting for all reversal types due to the inclusion of longitudinal relaxation. The rate of reversal is greater for linear over circular, thus the reversal mechanism plays a role in determining the final magnetisation of the system. As the system is cooled the magnetisation is still capable of switching, the degree of switching is limited by the time for which the

system temperature exceeds the blocking temperature. An increased rate of reversal is equivalent to an increased time period above the blocking temperature, as switching can occur in a reduced time window. Thus a system undergoing linear reversal is able to switch to a greater degree than one undergoing circular reversal for the same switching time window. It is this dependence which gives rise to the divergence of switching probabilities for peak temperatures exceeding the Curie point between the LLG and LLB solvers.

The semi-analytical model uses the same basis as the LLG and as a result agrees more closely with the LLG results than those of the LLB. However, it is possible to obtain the LLB results using the semi-analytical model by adjusting the timesteps used during the step-wise cooling phase. Greater time steps have the same effect as a reduced cooling rate, which produces the same result as if the magnetisation was able to switch more rapidly, as is the case for linear reversal. It should be noted however that the experimental data range used by this method for the determination of the Curie point distributions does not extend to regions where the peak temperature exceeds that of the average Curie point of the system. As a result of this the specification of the cooling rate is unimportant to the end goal of extracting the Curie point dispersion from experimental data.

4.4 Fitting via the semi-analytical model

The very low computational cost of the semi-analytical model makes fitting via a simple grid search possible. One of the benefits of the grid search method over more complex methods is the lack of a required method used to ensure that the fit does not converge to a local minima. The grid search method iterates over numerous parameters and determines a goodness of fit for each parameter combination, there is no implementation of a cost function used to determine the next optimal parameter set. It should be noted however that the traditional grid search method which utilises specified parameter steps has been shown to be significantly less effective than a randomised grid search [82]. Figure 4.6 illustrates how point grids differ from random point sets in their ability to describe the parameter space.

The semi-analytical model takes advantage of the generation of distributions in order to implement randomness to the grid search method. The model is provided with the parameter range and iteration intervals as is expected in the traditional grid search method. However, the nature of distribution generation typically results in variations in the dispersion from the input parameters. Due to the finite number of grains simulated there is a non-zero probability that the obtained distribution will be slightly different in terms of its mean and dispersion than the input values. This non-zero probability is reduced with an increased number of simulated grains where eventually the obtained distribution will converge to the

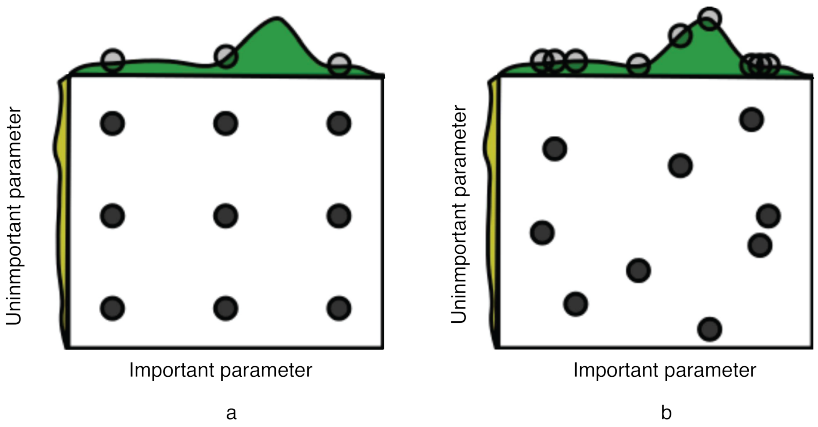

Fig. 4.6 Grid search of nine parameter combinations for describing the parameters space. (a) shows the traditional grid layout method, while (b) shows the random layout for the grid search method. The random layout has a greater ability to identify variations in the parameter space over the grid layout. [82]

desired values. However, greatly increasing the number of grains comes with additional computational cost. As the semi-analytical model must be highly efficient to enable large numbers of simulations to be performed in short periods of time it is not practicable to greatly increase the grain count in the simulations. Instead the obtained distribution parameters are determined and then used as the parameters for the grid search. The method keeps the computational cost of the simulations down and also introduces the desired randomness to the grid search method.

The goodness of fit metric used by the semi-analytical model is the χ^2, which is determined by

$$\chi^2 = \sum \frac{(O_i - E_i)^2}{\sigma_i} \tag{4.5}$$

where O_i is the simulated value, E_i is the expected value and σ_i is the weighting for data point E_i. The weighting value for experimental data typically relates to the associated uncertainty of the measurements. The value of χ^2 is minimised with better agreement between data due to the limit $\chi^2 \xrightarrow[O_i \to E_i]{} 0$, thus smaller values of χ^2 indicate better fits. To identify valid fits a significance level is decided prior to simulation. This significance level, α_{sig}, is the probability of incorrectly determining that the analytical model fits the data, a value of $\alpha_{sig} = 0.1$ indicates a 10% chance. Using the calculated χ^2 the P-value is obtained, specifically the P-value for χ^2 being less than the obtained value (i.e. $P(X < x)$). This P-value indicates the probability of randomly obtaining a smaller χ^2 value. If the obtained P-value is less then the specified significance-level then the fit is determined to be valid.

Figure 4.7 shows how the significance level and χ^2 distribution are used to determine a the validity of a fit.

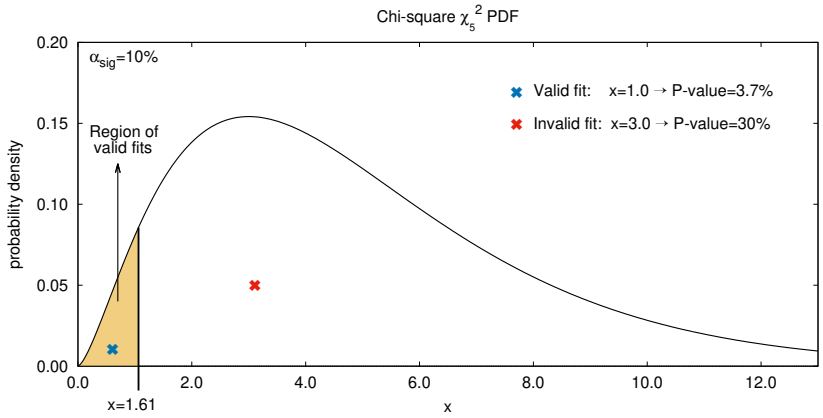

Fig. 4.7 Graphical representation of the method used to determine valid fits via the χ^2 distribution for a distribution with five degrees of freedom. For a significance value of 10% the shaded region indicates the values of χ^2 which relate to valid fits. The blue cross has a $\chi^2 = 1.0$ thus it lies within the region of validity as there is only a 3.7% chance of randomly obtaining a better fit, as indicated by the P-value. The red cross has a $\chi^2 = 3.0$ and thus does not lie within the region of validity due to there being a 30% chance of randomly obtaining a better fit, which greatly exceeds the significance level of 10%.

4.5 Proof of concept

MARS simulations have been performed to generate example experimental data for use as a proof of concept for the semi-analytical model. The Curie point distributions were determined via the grain size distributions as detailed in Section 3.5 and [68], thus only the diameter dispersion is referred to. The parameters used for the MARS simulation are detailed in Table 4.2. The obtained results were fed into the semi-analytical model in order to test and verify the ability of the model to extract the parameter distributions.

4.5.1 Extracting anisotropy dispersion

The semi-analytical model was provided with all variables except for the dispersion of the anisotropy, $\tilde{\sigma}_k$. The grid search method was used to determine the anisotropy dispersion. The range of $\tilde{\sigma}_k$ was set from 0.0% to 20.0% in increments of 0.25%. The obtained results are shown in Fig. 4.8. The P-value for a significant number of simulations lies very close to zero making it difficult to determine a correct value for the anisotropy dispersion. Thus it is clear that it is not possible to extract the anisotropy distribution using the semi-analytical model.

Table 4.2 Parameters used for the MARS simulations for use in the proof of concept simulations for the semi-analytical model.

Parameter	Value
Grains	1000
Ms (emu/cc)	1,100.0
$\langle K \rangle$ (erg/cc)	$4.5 \cdot 10^7$
$\tilde{\sigma_K}$	9.9
$\langle D \rangle$ (nm)	5.0
$\tilde{\sigma_D}$	8.9
Thickness (nm)	10.0
T_c^{∞} (K)	780.0
d_0	0.71
ν	0.79
Critical exponent	0.365
Callen power	2.0
Thermal bath coupling, λ	0.1
H_{appl} (Oe)	4000.0
Background temperature (K)	300.0
Pulse duration (s)	$10 \cdot 10^{-3}$
Rate cooling (K/s)	$4.0 \cdot 10^{11}$

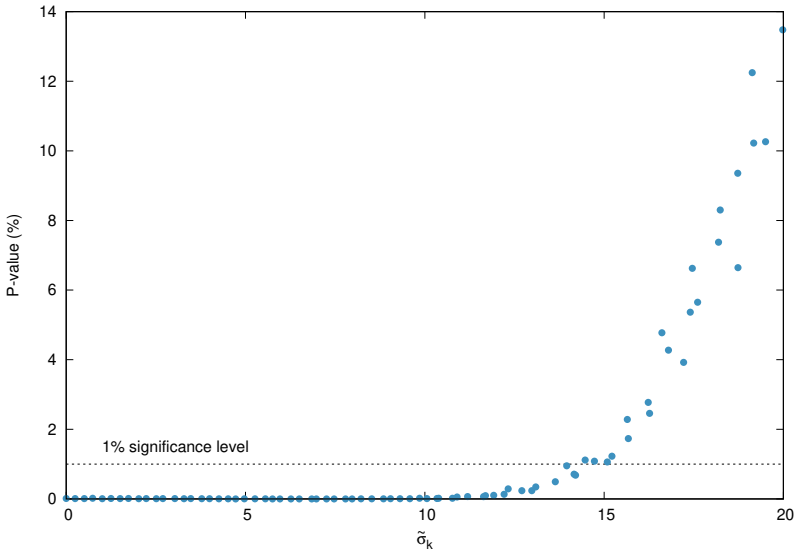

Fig. 4.8 P-value as a function of anisotropy dispersion. The known anisotropy dispersion is 10%. It is clear from this data that the model is highly invariant to changes in the anisotropy dispersion, shown by the almost constant P-value for anisotropy dispersion ranging from 0% to over 10%. Thus is is not possible to extract the anisotropy dispersion from the input data using this model.

4.5.2 Extracting grain size dispersion

Here the grain size dispersion was set as the only unknown parameter. The range used for the grain size dispersion was 0.00% to 20.0% in steps of 0.25%. The results are shown in Fig. 4.9. The model predicted a grain size dispersion of 8.8% with a significance level of 1%. This results in a percentage difference of only 1.1%, verifying the models ability to extract grain size distributions and as a result Curie point distributions from experimental data.

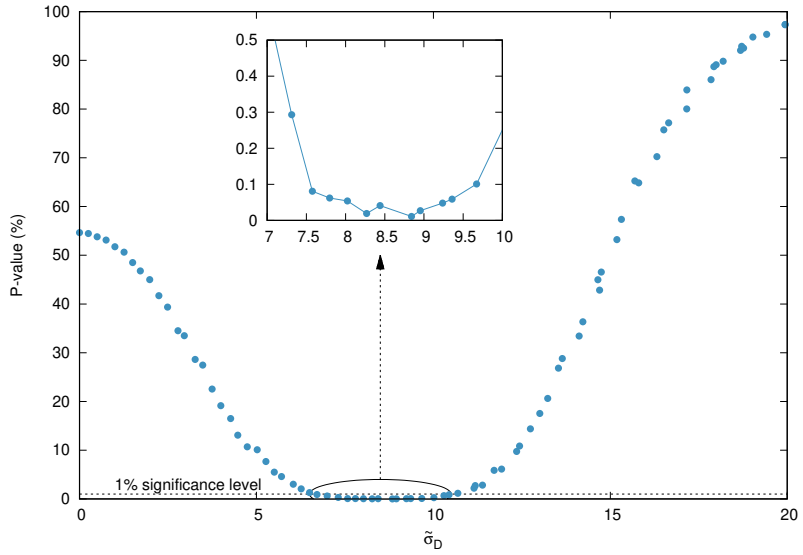

Fig. 4.9 P-value as a function of grain size dispersion. The known diameter dispersion is 8.9%. These results show that there is a significant dependence on the switching field distributions for the grain size distribution. The extracted value of the dispersion was 8.8% resulting in a percentage difference of only 1.1%.

4.5.3 Extracting both grain size and anisotropy dispersion

The semi-analytical model was used to perform a grid search over the diameter and anisotropy dispersion parameters. The ranges used for each parameter were the same as in the previous sections. The results are shown in Fig. 4.10. The significance level used was again 1%. The obtained results provide valid fits centred around the known value of 8.9% especially at the limit of a zero anisotropy dispersion. The results show a slight relationship between the two distributions, this suggests that in order to simplify the extraction of the grain size dispersion, and as a result the Curie point dispersion, it would be best to first obtain the anisotropy distribution via other experimental measurements.

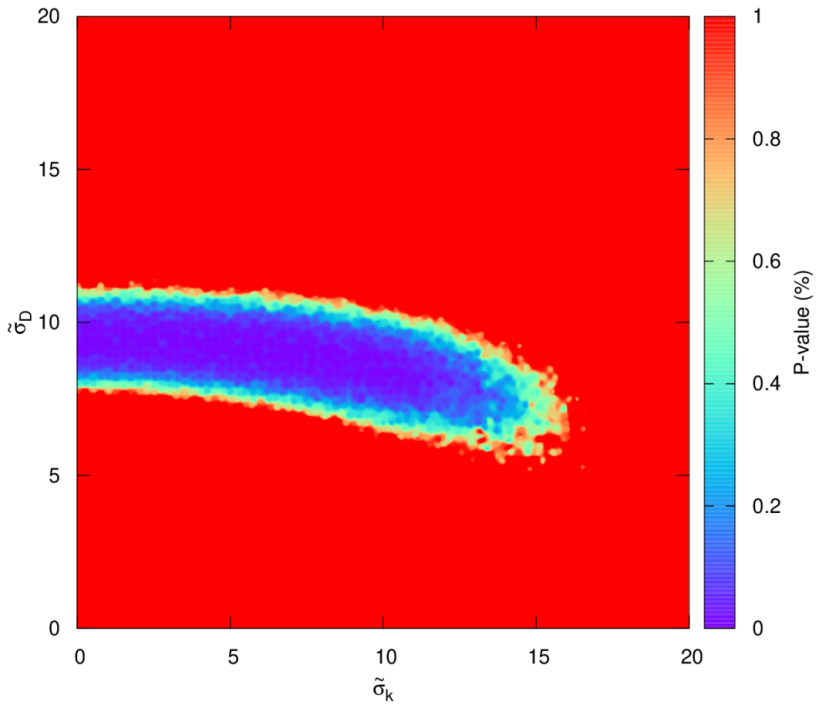

Fig. 4.10 Grid search for anisotropy and diameter dispersion parameters. The known distributions are 8.9% and 10% for the grain size and anisotropy respectively.

4.6 Extracting Curie point dispersion from experimental data

The semi-analytical model has been used to extract the Curie point dispersion from experimental data obtained by Seagate for a bi-layer system. The experimental procedure used was the same as described in Section 4.1 with multiple experiments performed, each with a different applied field strength ranging from 1,500 Oe to 6,900 Oe. For the initial extraction the 6,900 Oe results were used. To generate the Curie point distribution the relationship detailed in Section 3.5 and [68] was used. Figure 4.11 shows the comparison between the experimental data and best fit simulated results. The corresponding fit parameters are provided in Table 4.3. The obtained Curie point distribution has a dispersion of $\frac{\sigma Tc}{\langle Tc \rangle} = 1.3\%$. While the true value of the Curie point dispersion of the media is unknown it is similar in magnitude to values obtained in other works [77, 78].

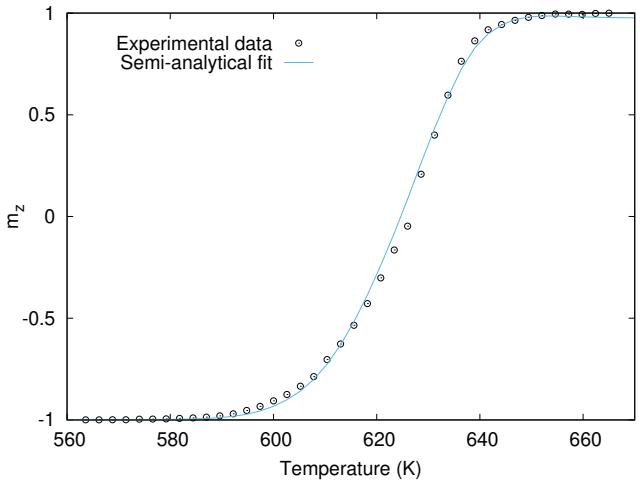

Fig. 4.11 Comparison of obtained fit (line) and input experimental data (points) for the 6,900 Oe applied field strength experiment.

Table 4.3 Best fit parameters for the 6,900 Oe experimental data.

Parameter	Value
Grains	4000
Ms (emu/cc)	1,100.0
$\langle K \rangle$ (erg/cc)	$9.3 \cdot 10^7$
$\tilde{\sigma_K}$	0.07
$\langle D \rangle$ (nm)	5.0
$\tilde{\sigma_D}$	0.1
Thickness (nm)	10.0
T_c^{∞} (K)	735.0
d_0	0.72
ν	0.85
Critical exponent	0.365
Callen power	2.0
H_{appl} (Oe)	6900.0
Background temperature (K)	300.0
Pulse duration (s)	$20 \cdot 10^{-3}$
Rate cooling (K/s)	$2.0 \cdot 10^9$
$\langle Tc \rangle$ (K)	659.3
$\tilde{\sigma_{Tc}}$	0.11

Following the extraction of the Curie point dispersion for the 6,900 Oe results the best fit parameters were used to simulate the thermoremanence for the other applied field strengths. The comparisons between the experimental data and simulation results are shown in Fig. 4.12.

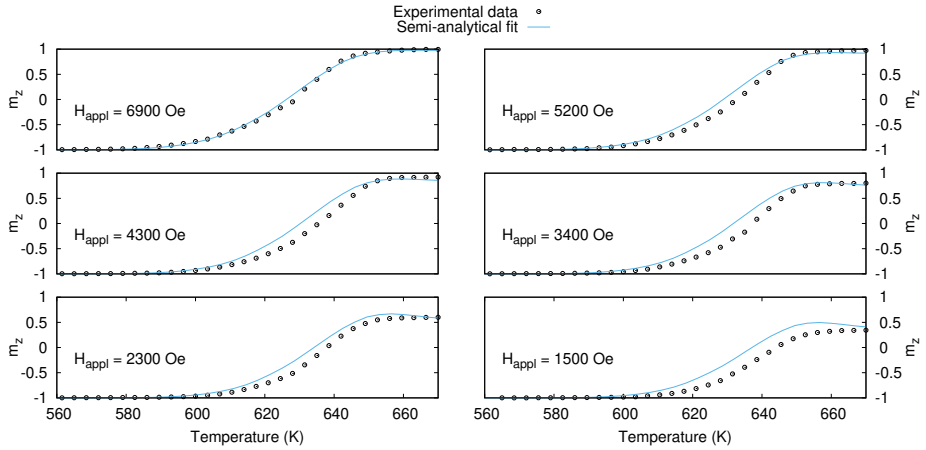

Fig. 4.12 Comparison between experimental data and simulated results for various applied field strengths. The parameters used for simulation were those obtained via fitting to the 6,900 Oe data.

It is clear from this figure that the simulated system does not follow the correct behaviour as the applied field strength is varied. The inability to correctly describe the thermoremanence for different applied field strengths arises from the bi-layer structure of the experimental system. For bi-layer systems the Stoner-Wohlfarth description of the energy is no longer sufficient and thus the semi-analytical model is incapable of describing these systems. It is, however, possible to implement a description of the energy barrier for bi-layer systems. The energy barrier variation as a function of field strength can be modelled via [83]:

$$\Delta E = \Delta E_0 \left(1 - \left(\frac{H}{H_{cr}}\right)^{\alpha}\right)^{\beta}, \tag{4.6}$$

where ΔE_0 is the zero field energy barrier, α and β are fitting parameters and H_{cr} is the critical field which would be equal to the anisotropy field for the purposes of this model. Using this function P. Gavriloaea was able to accurately describe the energy barriers of bi-layer systems [83]. Thus it stands to reason that implementation of this method for describing the energy barrier field dependence will enable the developed semi-analytical model to correctly describe bi-layer systems and as a result extract the effect Curie point dispersion from such systems.

4.7 Summary

A semi-analytical model to determine Curie point distributions via thermo-remanence has been developed. This model greatly reduces the computational cost of thermo-remanence simulations. Performing a grid-search using this semi-analytical model allows the grain size dispersion to be successfully extracted from input thermo-remanence data. The computational efficiency of the developed model is such that it is possible to perform hyper-parameter grid-searches by running the model in parallel. However the model has been shown to be unresponsive to small variations in the anisotropy dispersion. Thus an experimental procedure to obtain the anisotropy dispersion prior to using the developed model is required. A suggested method for this would be first-order reversal curves (FORC). A Curie point dispersion was extracted from experimental results provided by Seagate. The obtained Curie point dispersion was 1.3 % which is within the range identified by other works [77, 78]. This provides a strong case for the description of the Curie point distributions via the grain size distribution as determined by Hovorka et al. [68] and further suggests the the Curie point distribution arises solely from the distribution of grain sizes. The model, however, is unable to reproduce the change in thermoremanence as a function of the applied field strength. This is due to the bi-layer structure of the system used in the provided experimental data. P. Gavriloaea has shown it is possible to model the energy landscape of bi-layer systems via Eq. 4.6 [83]. As a result the developed model may be improved via the implementation of Eq. 4.6 enabling the model to describe bi-layer systems and extract their Curie Point distributions.

5

Adjacent track erasure

The primary aim of the magnetic recording industry is to increase storage capacities whilst reducing the overall cost per gigabyte. A large step forward in this endeavour has already been achieved with the development of commercial HAMR drives with a density of $2\,\mathrm{TB/in^2}$. However the road map for recording media technology set by the ASTC details the development of HAMR technologies exceeding this density. To achieve this, data stability must be ensured for the ever decreasing bit lengths and track widths. In general, tracks are tightly packed with no spacing between adjacent tracks in order to maximise track density. As a result adjacent track interference (ATI) is present which arises from two mechanisms. These mechanisms are illustrated in Figure 5.1. Encroachment (also known as adjacent track erasure (ATE)) is the damage done to a data track during the writing process of an adjacent track. Written-in interference is the process whereby stray fields from previously written data interfere with the writing process of the current track. Investigations have shown that the effect of written-in interference is reduced in HAMR over perpendicular magnetic recording (PMR) systems [84] and that it is also less significant than encroachment for HAMR systems [12]. Due to the lower significance of the written-in interference for HAMR systems the work presented here does not account for written-in interference as interactions are ignored. While ATE has existed since PMR [85] the physical mechanisms driving ATE are different for PMR and HAMR. For HAMR systems there is an overlap of thermal gradients generated by the near field transducer which contributes to the ATE.

The signal-to-noise ratio (SNR) is a measure of the quality of stored data. Magnetic recording media is designed to provide data storage for up to ten years [86, 87, 13, 88, 7]. Over time the SNR will decrease due to thermally activated reversals of some grains within the media. Thus, in order to facilitate long term data storage via magnetic recording it is important to produce large initial SNRs to allow for some degradation over time. As ATE has a significant impact on the initial SNR an investigation has been performed to identify the

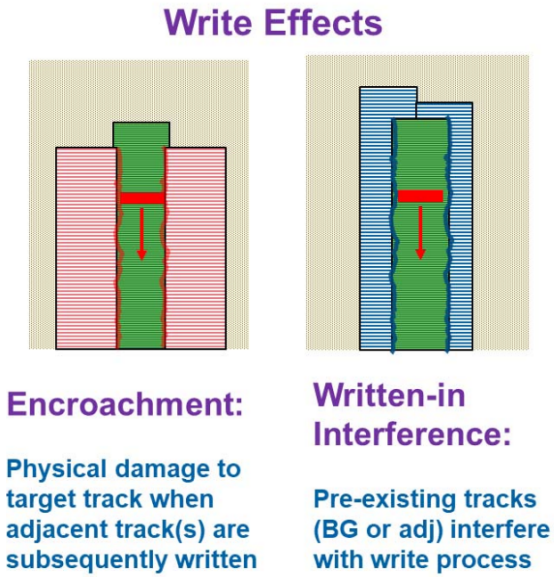

Fig. 5.1 Illustration of physical interference effects present in HAMR. The red rectangle represents the read head placed on the test track (green). Underlying tracks are represented in blue with overlying tracks represented by red. (BG refers to background tracks, adj refers to adjacent tracks). Obtained from [84].

effect of ATE on long term data storage. Using MARS it is possible to simulate the writing process followed by long term data storage and subsequent read back. This chapter details the investigation performed into the effect of ATE on long term data storage. The initial simulations focus on multiple immediate track writes followed by time evolution up to ten years. The investigation is then expanded to cover the process of staggered data writes with the adjacent tracks being written after specified periods of time, allowing for the decay of the data of the initial track prior to the adjacent write.

5.1 Simulation setup

For the simulations two tracks were written, two tracks are sufficient to investigate ATE as for HAMR systems the effect of ATE lies predominately on the immediately adjacent tracks [85]. Figure 5.2 shows the track positions along with the full-width at half maximum (FHWM) of the heated spot for the simulated systems. In order to aid comparison with previous investigations such as those performed by Natekar et al. the initial systems generated were set to match those used in [12]. The system parameters are detailed in Table 5.1. Two materials have been simulated with different average anisotropies. The first system had a uniaxial anisotropy energy density of $7 \cdot 10^7$ erg/cm^3 in line with perfectly ordered $L1_0$ FePt [89, 88].

The second system had a reduced anisotropy of $4 \cdot 10^7$ erg/cm^3 to provide an energy barrier of approximately 80 k_BT at 300 K, which is more than sufficient to successfully store data for ten years [86, 90, 91, 88, 7]. The track spacing was chosen to be 70% the size of the heated spot FWHM as this has been shown to be optimal [92]. The materials used included parameter distributions to account for variation in magnetic properties due to fabrication processes, all distributions were log-normal. In total ten separate granular structures were used for each simulation with the read back signals from each system used to determine the SNR.

Table 5.1 System parameters for ATE simulations

Parameter	Value
System length (nm)	384
System width (nm)	96
Bit length (nm)	20
Track width (nm)	21
Heated spot FWHM (nm)	30
H_{write} (x,y dimension) (nm)	30
Read head velocity (nm/s)	20
$\tilde{\sigma_K}$	0.15
$\langle Tc \rangle$ (K)	692
$\tilde{\sigma_{Tc}}$	0.03
$\langle D \rangle$ (nm)	5.4
$\tilde{\sigma_D}$	0.24

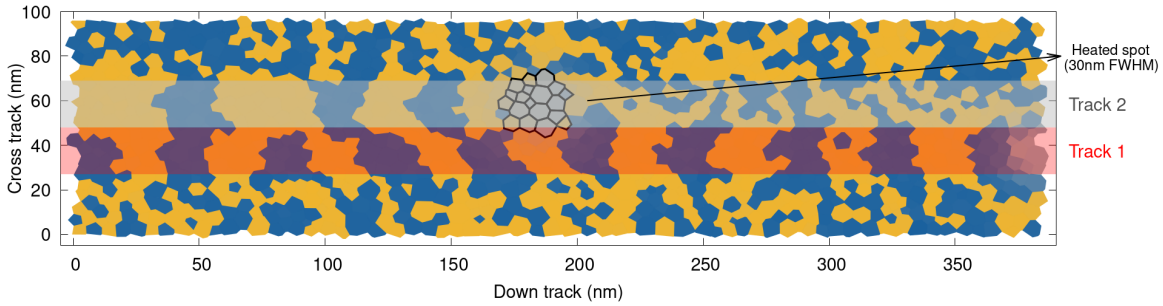

Fig. 5.2 Track placement for ATE simulations where the width of each track is 21 nm. Track 1 is the initially written track with all subsequent simulations writing to track 2. The heated spot has a FWHM of 30 nm.

5.2 Writing process, time evolution and read back

The simulations begin with the recording of a 19-bit square-wave sequence to track one. The write field used throughout the simulations was 10 kOe with zero skew angle and no spacing from the NFT. After the write process for the initial track was complete the adjacent track was written. The adjacent tracks were overwritten multiple times with the same 15-bit pseudorandom binary sequence (PRBS) with two padding bits appended to either end (00100111010111100010). Additional simulations were performed with a different PRBS used for each adjacent track write. These binary sequences were treated as non-return to zero (NRZ) data patterns, thus the zero and one values refer to maximum and minimum magnetisation respectively.

The read back simulation was performed using the kMC solver to model an ideal read head scanning along track one. The assumption of an ideal read head means that all the observed noise arises from the write process only. The use of an ideal read head also means that the read back does not require repetition. The system was first discretised into 1 nm^2 cells and the read head was set on the centre of the desired track. The read head was then moved along the track in single cell increments with the magnetisation determined via the average magnetisation within the read head at each step. In order to reduce noise in the obtained signal a five-step rolling average was also determined.

The time evolution was also performed using the kMC solver. The system was allowed to evolve for up to ten years with read back simulations performed at specified points in time. In order to investigate the physical size of the encroachment on track one the cross track dimension of the read head was varied between 15 nm, 21 nm, 25 nm and 30 nm. Figure 5.3 shows an example of the read back process along with the obtained instantaneous and rolling average signal.

5.3 SNR calculation

The SNR is used to quantify the success of the write process. To calculate the SNR multiple repetitions are required and in order to the reduce computation time the multiple systems were simulated in parallel as opposed to a single system with repetitions simulated serially. The calculation of the SNR follows the ensemble waveform analysis presented by S. Hernandez et al. [93, 94]. The first step required is to sync each of the signals, this is achieved via cross-correlation [95]. A low-pass filter is then applied to each of the signals to remove the high-frequency content [96]. These signals are then averaged to produce a noise-free signal and the spatial noise is then obtained by subtracting the noisy signals from the average signal.

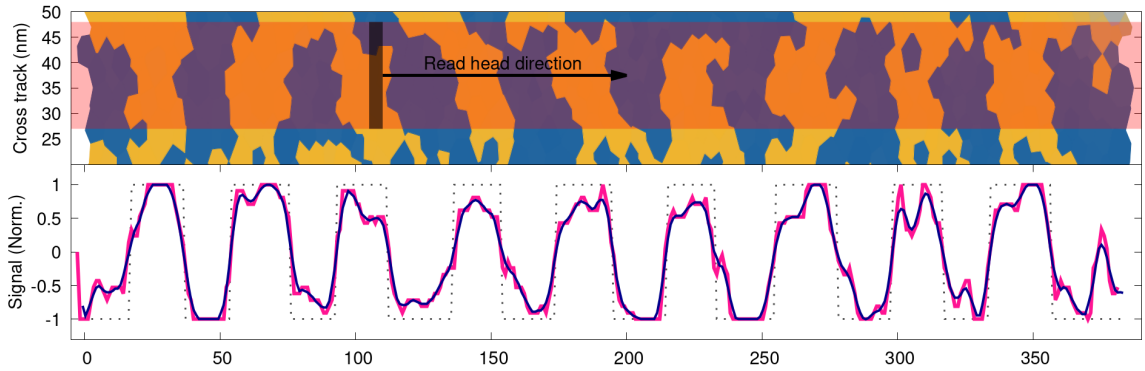

Fig. 5.3 The read head is scanned along the track in 1 nm steps with the magnetisation determined at each iteration. A rolling average of the magnetisation over five steps is also determined. The top part of the figure shows the structure of the read head, track and granular media. The bottom half of the figure shows the signal obtained via the read back process. The blue curve is the magnetisation for each iteration, the red curve is the rolling average of the magnetisation. The grey dashed line represents the signal when converted from analogue to digital.

The process of determining the noise is illustrated in Fig. 5.4. The total SNR is calculated using the power definition given by

$$SNR_{dB} = 10\log_{10}\left(\frac{P_{signal}}{P_{noise}}\right), \tag{5.1}$$

where P_{signal} and P_{noise} are the powers of the signal and noise respectively. The spatial noise represents the total noise consisting of the transition and remanence noises. These noises can be extracted from the spatial noise by applying the appropriate windowing function. The windowing function for the transition noise is non-zero at the transitions and zero elsewhere, while the function for the remanence noise is the opposite. Figure 5.5 shows the regions contributing to the remanence and transition noise terms along with the formation of the spatial noise.

5.4 Characterisation of ATE

The initial results obtained focus on the quantitative characterisation of the ATE. The method used to quantify the ATE is the same as used in [12], with the SNR expressed as a function of adjacent track writes:

$$SNR_{dB} = SNR_1 + \mathrm{A_{ATE}}\ln(\text{Write No.}), \tag{5.2}$$

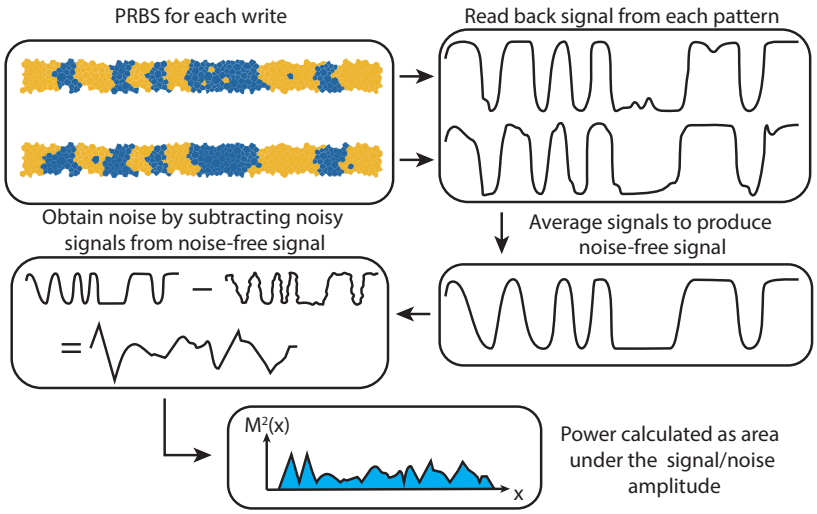

Fig. 5.4 Ensemble waveform analysis process. The PRBS is written multiple times, followed by a read back simulation. A noise-free signal is generated by averaging the signals obtained from each PRBS. The noise is then calculated by subtracting the noisy signal from the average signal. The powers of the signal and noise are then obtained by determining the area under the respective squared magnetisation. Adapted from Hernandez et al. [94].

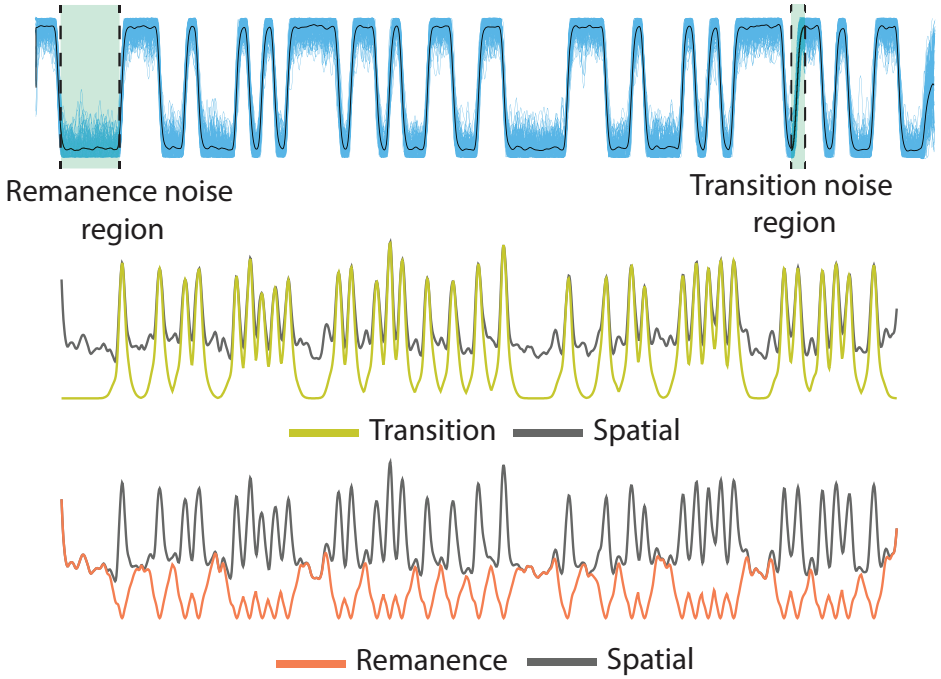

Fig. 5.5 Extraction of the remanence and transition noise from a 57 bit track. The average signal is shown in black. The transition, remanence and spatial noises are shown at the bottom. The spatial noise is a combination of the remanence and transition noises and is the total noise of the system.

where SNR_1 is the SNR after the first adjacent track write and A_{ATE} is the strength of the ATE. The greater the magnitude of A_{ATE} the greater the extent of the ATE. The applied fit does not include the SNR prior to the adjacent track write, SNR_0, as the SNR loss due to the initial adjacent track write is significantly greater than the subsequent adjacent track writes.

Figure 5.6 shows the variation of the transition and remanence SNR for the ideal $L1_0$ FePt system for multiple read head widths for the same and varied adjacent track PRBS. The results are summarised in Table 5.2. All the results show that the SNR for the transition noise is smaller than that for the remanence noise. This difference in SNR indicates that the transition noise is the predominant and therefore limiting factor of the overall SNR and that efforts to improve the system SNR should focus on the transition noise over the remanence noise.

The varied PRBS results show a larger scatter in general compared to those obtained using the same PRBS. This is to be expected, as changing the PRBS each write introduces additional variation in the data written to the encroachment region of track one. The larger scatter creates difficulties in using Eq. 5.2 for characterisation of the ATE as the strength of the ATE can vary based on the specific PRBS written. For example the greatest loss of SNR is expected for an adjacent track data sequence which is exactly opposite to the sequence stored on track one. Additionally if the sequence written to the adjacent track was identical to that currently stored on track one the SNR of track one would be expected to increase due to the encroachment region reinforcing the data already present in track one. The increased difficulty in characterising the ATE for a varied PRBS is shown by the greater uncertainties in the determined values of the ATE. The strength of the ATE for different read head widths is shown in Fig. 5.7. The obtained results show a possible variation of the ATE with read head width which shows the largest strength of the ATE (note this is represented by the lowest values in the figure) when the read head width is equal to the track width. The strength of the ATE appears to reduce as the read head width is increased beyond the track width. This relationship can be explained by considering the region covered by the read head along with the size of the encroachment region, this is illustrated in figure Fig. 5.8. As the read head width is increased from 15 nm to 21 nm the read head becomes large enough to cover a larger proportion of the encroached region increasing the strength of the ATE. As the read head width is extended beyond the track width it begins to cover the unwritten region below track one which add an additional source of noise independent of the ATE reducing the effective strength of the ATE.

All data sets show a change in SNR, prior to an adjacent track write, as a function of read head width, with the greatest SNR obtained for a read head width equal to the track width. These results are provided in Fig. 5.9a. This change in the overall SNR with read

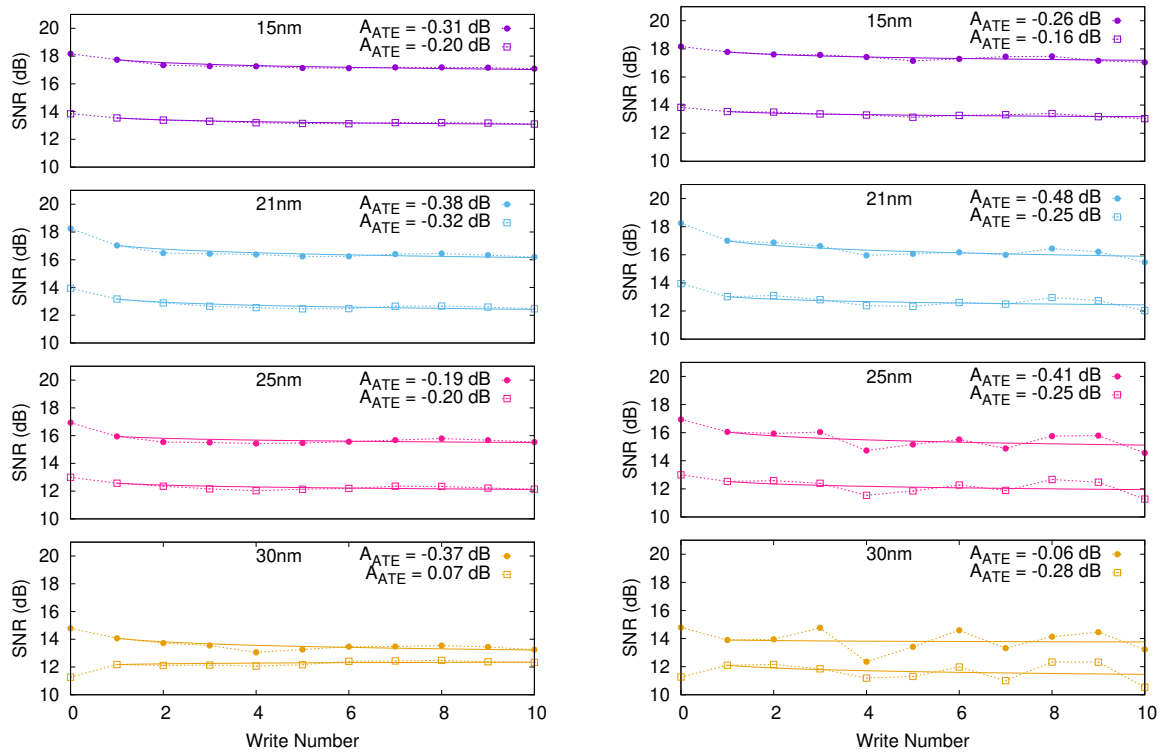

(a) Same PRBS

(b) Varied PRBS

Fig. 5.6 Transition (dashed line with hollow squares) and remanence (dashed line with filled circles) SNR components as a function of adjacent track writes due to ATE for the same PRBS each write (a) and a different PRBS each write (b) for read head widths ranging from 15 nm to 30 nm for the ideal $L1_0$ FePt system. The solid line represents the fit obtained via Eq. 5.2.

Table 5.2 Results obtained from ATE simulations of the ideal $L1_0$ FePt system.

PRBS per write	Read head width (nm)	SNR_0 (dB)		SNR_1 (dB)		A_{ATE} (dB)	
		Remanence	Transition	Remanence	Transition	Remanence	Transition
Same	15	18.2	13.8	17.7	13.5	-0.31	-0.20
	21	18.2	13.9	17.0	13.2	-0.38	-0.32
	25	16.9	13.0	15.9	12.6	-0.19	-0.20
	30	14.8	11.3	14.1	12.2	-0.37	0.07
Varied	15	18.2	13.8	17.8	13.5	-0.26	-0.16
	21	18.2	13.9	17.0	13.0	-0.48	-0.25
	25	16.9	13.0	16.1	12.5	-0.41	-0.25
	30	14.8	11.3	13.9	12.1	-0.06	-0.28

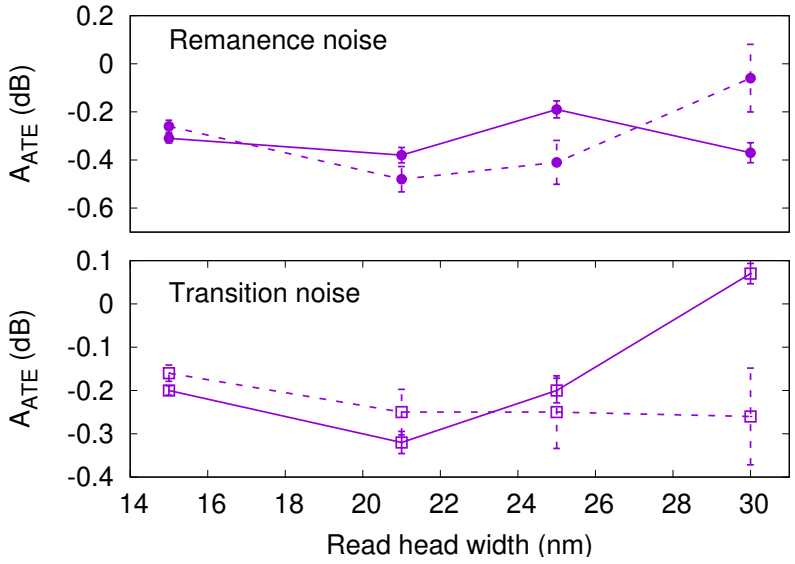

Fig. 5.7 A_{ATE} as a function of read head width for the ideal $L1_0$ FePt system. The same PRBS simulations are represented by the solid lines and the varied PRBS simulations are represented by the dashed lines.

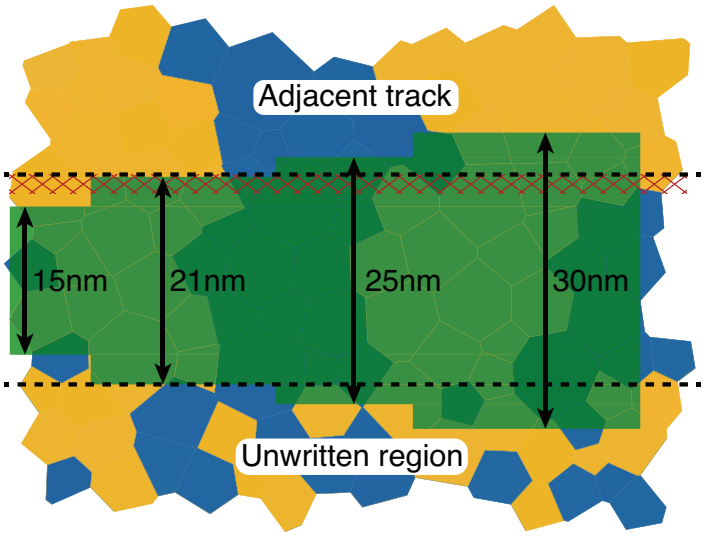

Fig. 5.8 Illustration showing how the variation of the read head width results in different overall SNR and A_{ATE}. The area covered by the read head is shown by the green shading for multiple widths ranging from 15 nm to 30 nm. The boundaries of track one are represented by the dashed lines, while the region damaged by encroachment is represented by the hatching.

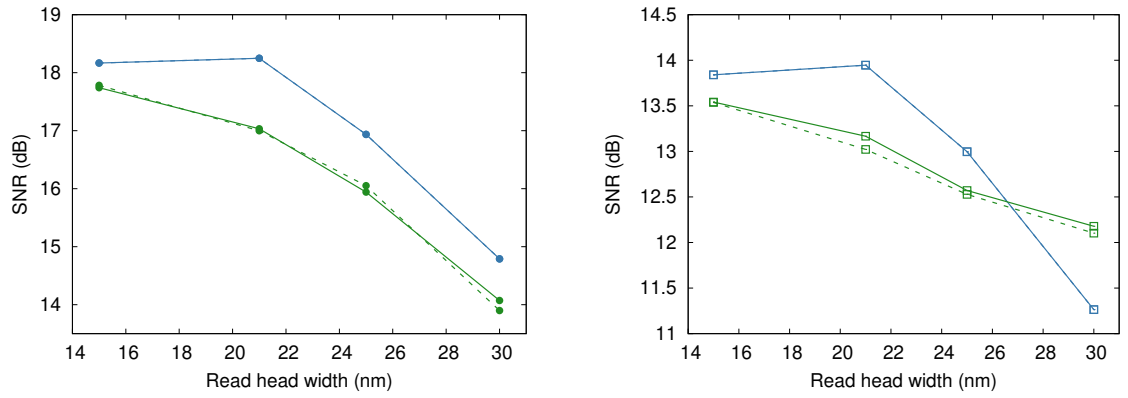

(a) Remanence component (b) Transition component

Fig. 5.9 SNR as a function of read head width for the ideal $L1_0$ FePt system before (blue) and after (green) the initial adjacent track write. The results for both the same PRBS (solid line) and varied PRBS (dashed line) simulations are provided.

head width can be explained in a similar manner to the change in the A_{ATE}. When the read head is smaller than the track width it covers only a small proportion of the total track area increasing the effect of any unswitched grains resulting in a possibly reduced overall SNR. As the read head width is increased the larger area produces a larger SNR, however this difference is very small. Once the read head width begins to extend beyond track one the SNR begins to reduce occurring due to the read head overlapping unwritten areas above and below track one.

After a single adjacent track write has been performed the change of SNR as a function of read head width is significantly different. Here the overall SNR is shown to decrease with increasing read head widths, with the maximum SNR occurring for the 15 nm read head width. The change in behaviour after the initial adjacent track write can be attributed to the now present encroachment region. As the read head width is extended from 15 nm to 21 nm the proportion of the encroachment region covered by the read head increases resulting in a reduction of the overall SNR instead of the observed increase for the systems prior to the adjacent track write. This is further evidenced by the results shown in Fig. 5.7 which show an increased strength of the ATE as the read head is increased from 15 nm to 21 nm. The transition component shows a significantly reduced SNR loss between 25 nm and 30 nm after the initial adjacent track write. This can be attributed to the reduction in the number of transitions present above track one caused by the initial adjacent track write. It should be noted that while these results suggest that the solution to the SNR loss caused by ATE is simply to reduce the read head width in production HAMR devices there must be a separation of the write head and NFT [10]. This separation leads to the requirement for a larger heated

spot FWHM which will produce a greater encroachment region requiring even smaller read head widths to avoid. As such it is not feasible to simply reduce the read head width to avoid the encroachment region.

Figure 5.10 shows the SNR variation for multiple read head widths for the reduced anisotropy system. These results are summarised in Table 5.3. The obtained results show a larger scatter in the strength of the ATE, as a result it is difficult to determine a relationship between the strength of the ATE with the read head width. These results are shown in Fig. 5.11, comparison with Fig. 5.7 reveals a similar behaviour, however, the correlation between the two sets of results appears low.

The SNR values obtained before and after the initial adjacent track write are shown in Fig. 5.12a. These results show that prior to the initial adjacent track write there is a greater change in the SNR for different read head widths with a larger difference occurring between 15 nm and 21 nm than observed for the higher anisotropy ideal $L1_0$ FePt system. Furthermore the obtained SNR for read head widths greater than the track width are larger than for the ideal $L1_0$ FePt system.

The results obtained after the initial track write show that a substantial change in the system has occurred with the greatest effect shown in the remanence component. The effect of the adjacent track write appears greater than for the ideal $L1_0$ FePt system due to the larger decrease in the observed SNR. These results also show a noticeable difference between the same PRBS and varied PRBS simulations. This further suggests that the sequence written to the adjacent track has a significant influence on the strength of the ATE which has also been shown by the increased scatter of the results shown in Fig. 5.10 and Fig. 5.6. Unlike the previous higher anisotropy system, here the ATE has caused a larger area of damage to the initially written track causing significant SNR loss even for the 15 nm read head width. This observation further supports the notion that simply reducing the read head width will be insufficient in mitigating the affects of ATE.

All of the above observed differences between the behaviour of the reduced anisotropy system compared to the ideal $L1_0$ FePt system can be attributed to the reduced coercivity of the granular media. The reduction of the granular media will result in an effective increase of the switchable region created by the application of the heated spot. This manifests as a shift in the switching position of the grains in a similar manner to the per grain variation of the Curie point as explained in the introduction of Chapter 4. The change in the switching position will enable a larger region of grains to be switched towards the write field direction increasing the initial system SNR. However, this increased switchable region also results in a larger encroachment region causing a greater reduction in the SNR once the initial adjacent track is written. This also explains the decreased dependence of the ATE on the read head

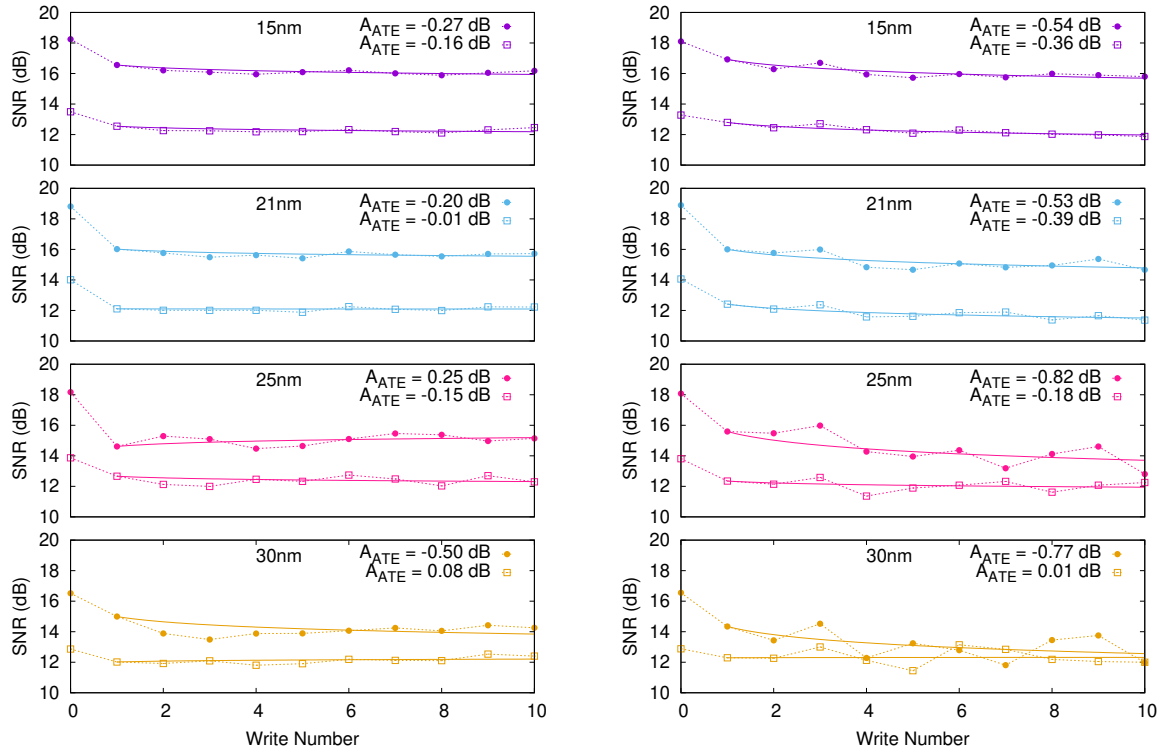

(a) Same PRBS

(b) Varied PRBS

Fig. 5.10 Transition (dashed line with hollow squares) and remanence (dashed line with filled circles) SNR components as a function of adjacent track writes due to ATE for the same PRBS each write (a) and a different PRBS each write (b) for read head widths ranging from 15 nm to 30 nm for the reduced anisotropy system. The solid line represents the fit obtained via Eq. 5.2.

Table 5.3 Results obtained from ATE simulations of the reduced anisotropy system.

PRBS per write	Read head width (nm)	SNR_0 (dB)		SNR_1 (dB)		A_{ATE} (dB)	
		Remanence	Transition	Remanence	Transition	Remanence	Transition
Same	15	18.2	13.5	16.6	12.5	-0.27	-0.16
	21	18.8	14.0	16.0	12.1	-0.20	-0.01
	25	18.2	13.9	14.6	12.7	0.25	-0.15
	30	16.5	12.9	15.0	12.0	-0.50	0.08
Varied	15	18.1	13.3	16.9	12.8	-0.54	-0.36
	21	18.9	14.1	16.0	12.4	-0.53	-0.39
	25	18.1	13.8	15.6	12.3	-0.82	-0.18
	30	16.6	12.9	14.3	12.3	-0.77	0.01

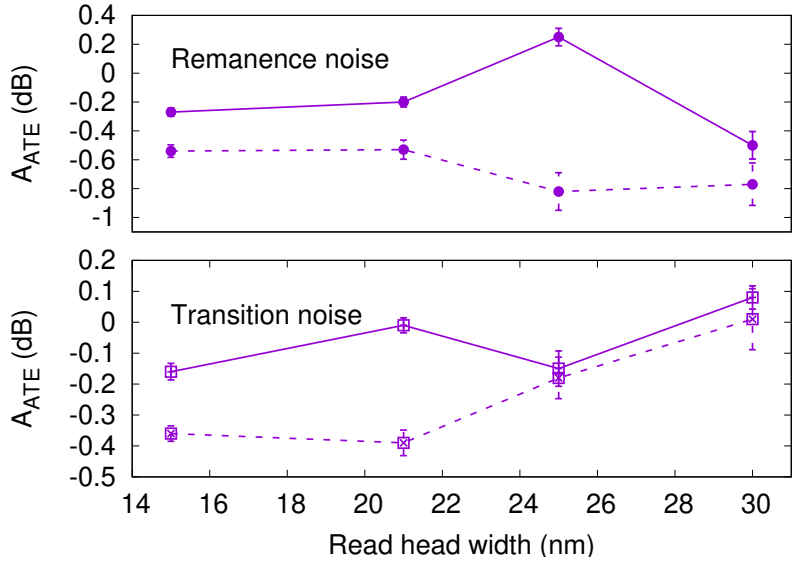

Fig. 5.11 A_{ATE} as a function of read head width for the reduced anisotropy system. The same PRBS simulations are represented by the solid lines and the varied PRBS simulations are represented by the dashed lines.

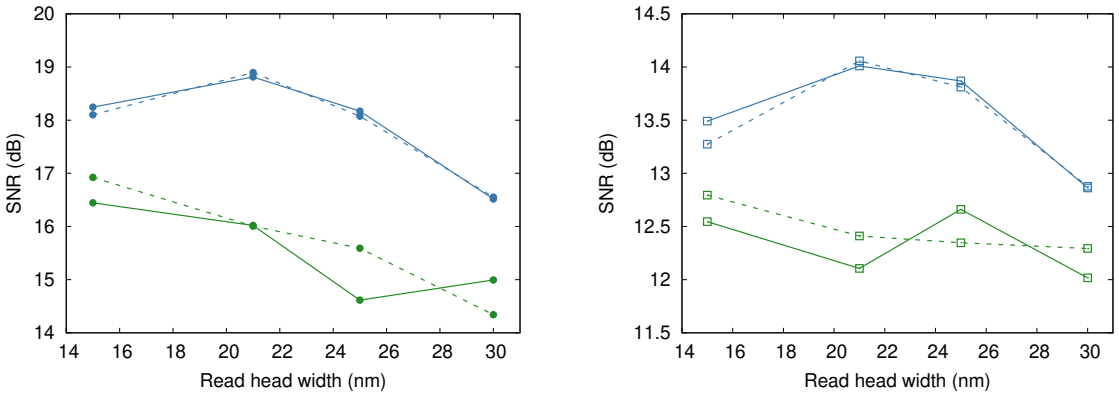

(a) Remanence component

(b) Transition component

Fig. 5.12 SNR as a function of read head width for the reduced anisotropy system before (blue) and after (green) the initial adjacent track write. The results for both the same PRBS (solid line) and varied PRBS (dashed line) simulations are provided.

width as the encroachment region will be greater resulting in a reduced change in strength as the read head is increased from 15 nm to 21 nm since the smaller read head width will now cover a larger proportion of the encroachment region than in the ideal $L1_0$ FePt system.

5.5 Time decay of recorded information

For the initial time decay investigation track one was written and the system was simulated using the kMC solver over a time period up to ten years with an environmental temperature of 300 K. The SNR reduction as a function of time evolution for both the transition and remanence components of the reduced anisotropy system for multiple read head widths is shown in Fig. 5.13. The ideal $L1_0$ FePt has a system average energy barrier at 300 K of approximately 250 k_BT, hence there is no degradation of the recorded information over the ten year time window. Hence only the results for the reduced anisotropy system are provided.

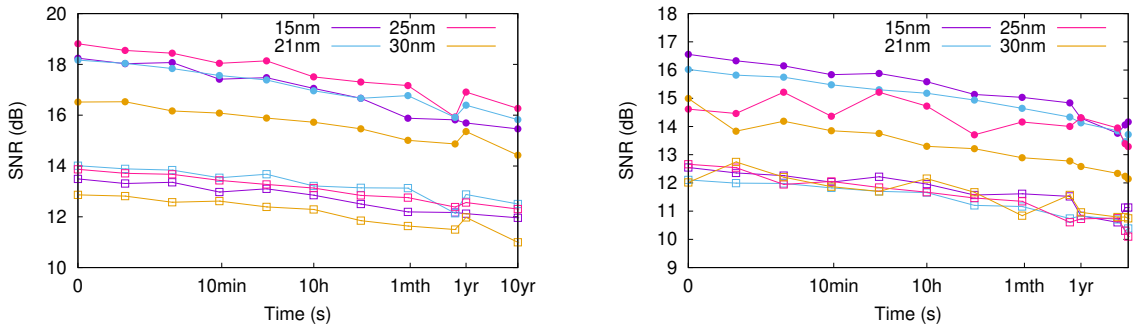

(a) Before adjacent track write

(b) After adjacent track write

Fig. 5.13 Time decay of recorded information after the initial track write for the reduced anisotropy system before (a) and after (b) an adjacent track write for transition (hollow squares) and remanence (filled circles) respectively for read head widths ranging from 15 nm to 30 nm.

These results, shown in Fig. 5.13a, show that the SNR loss due to time evolution is on a par with the SNR loss produced by ATE for both components. This observation alone suggests that the reduction in SNR due to ATE is of the same significance as that of temporal decay. However, as can be clearly seen in Fig. 5.6 and Fig. 5.10 the majority of the SNR loss due to ATE occurs for the initial adjacent track write. This initial drop of the SNR makes the comparison of the strengths of the ATE and temporal decay difficult. To more effectively compare the strengths of the two effects the time evolution of the system after the initial adjacent track write is provided in Fig. 5.13b.

Figure 5.13b shows that the loss of SNR over time is significantly stronger than that due to the ATE. The SNR drops by around 2 dB, with the majority of this occurring within

the first month. Meanwhile the SNR drops by around only 1 dB for nine adjacent track writes with the trend showing a decrease in SNR loss for each subsequent adjacent track write as shown in Fig. 5.10. Similarly to the results shown in Fig. 5.12a and Fig. 5.12b the change of the transition component with read head width is much less significant than that of the remanence component. However both components appear to have similar gradients suggesting that they are equally affected by the time evolution.

5.6 ATE influence on time decay of written data

After each write the system has been copied and allowed to evolve over time. The obtained SNR components for a read head width of 21 nm are provided in Fig. 5.14. As the time decay is performed on a copy of the system the effects of the time decay are not present in the subsequent adjacent track writes. To simplify the plots the data for a reduced number of adjacent track writes are shown. The initial SNR (i.e. no adjacent track write, no time evolution) has been subtracted from each result in order to more clearly show the change due to ATE and time evolution. The obtained results show no significant variation in the loss of SNR, for either component, due to time evolution as a result of the number of adjacent track writes. The results obtained for other read head widths show the same behaviour as expected from the previous results and have therefore been omitted.

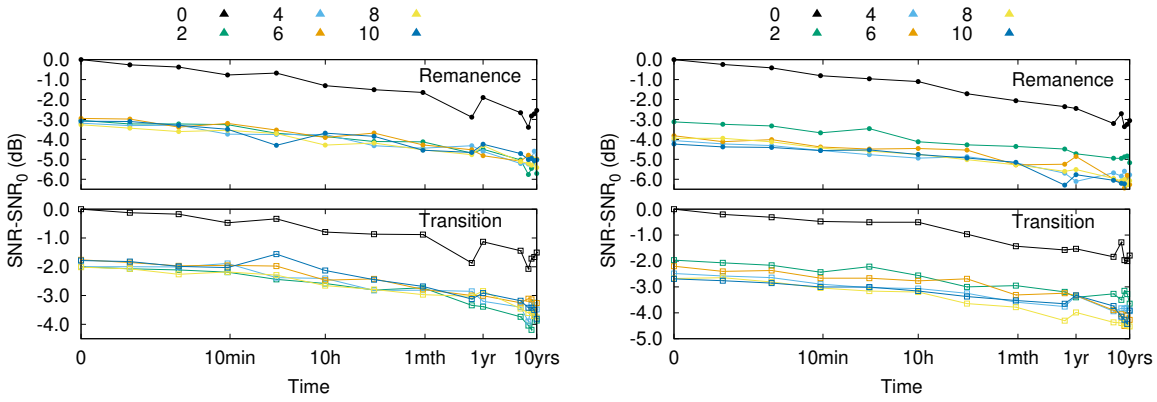

(a) Same PRBS

(b) Varied PRBS

Fig. 5.14 SNR variation due to ATE and time evolution for transition and remanence components for same and different PRBS each write. The SNR has been normalised in order to more clearly show the change due to time evolution. The read head width was set to 21 nm. The different adjacent track writes are indicated by the colours provided in key.

5.7 SNR loss for staggered adjacent track writes

In real world applications storage media will experience the effects a combination of both ATE and time evolution. Typically data will experience adjacent track writes throughout its storage time resulting in the effects of both ATE and time evolution in a combined manner. Here the influence of such scenario on track one is investigated. For these simulations the system was evolved over time for a month or a year followed by an adjacent track write. This process was then repeated for ten iterations producing a system consisting of ten adjacent track writes aged by eleven months or years. The SNR over time for both the remanence and transition noise for monthly and yearly spaced writes are shown in Fig. 5.15.

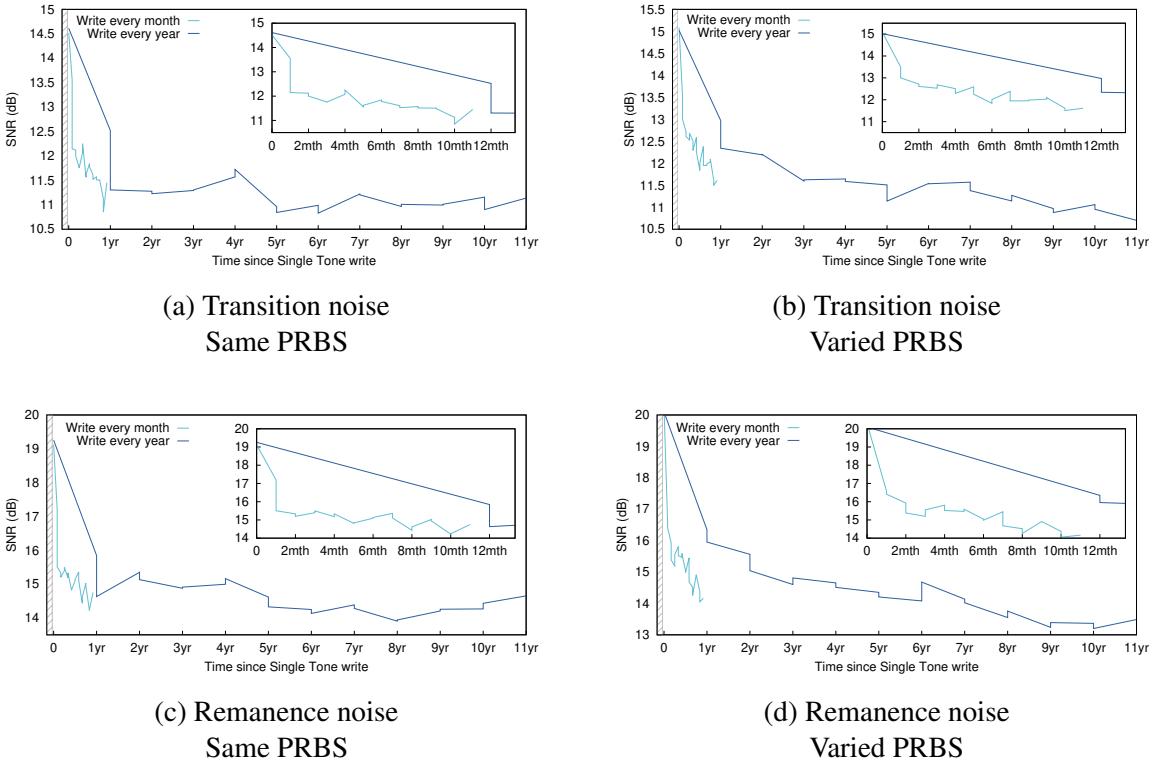

(a) Transition noise
Same PRBS

(b) Transition noise
Varied PRBS

(c) Remanence noise
Same PRBS

(d) Remanence noise
Varied PRBS

Fig. 5.15 Comparison of SNR over time for staggered adjacent track writes for writes performed each month and writes performed each year. The read head width used for these simulations was 21 nm. Results are shown for transition (a and b) and remanence (c and d) noise for the same PRBS each write (a and c) and a different PRBS each write (b and d).

These results show that when the same PRBS is used for each write that the reduction in SNR for both remanence and transition components after ten monthly spaced adjacent track writes is on a level with a single adjacent track write performed one year after track one was written. This result suggests that the effect of the ATE after the initial adjacent track write is

negligible in comparison to the effects of time evolution with a single adjacent track write when the same PRBS is repeatedly written. This is further evidenced by the small reduction of SNR shown for the additional adjacent track writes performed one year apart. Both results for the same PRBS simulations indicate the reduction of SNR with additional adjacent track writes decreases with the number of writes. The reduction in the loss of SNR with multiple adjacent track writes of the same sequence can be explained by considering the magnetisation of the grain within the encroachment region. As the adjacent track is re-written these grains will eventually match the adjacent track PRBS exactly at which point the loss of SNR of the track one will become zero as no further change will be present in the encroachment region.

The strength of the ATE is again shown to be greater when the PRBS is varied for each write rather than being kept constant. This increased ATE appears to create a greater reduction of the SNR for monthly spaced writes which results in the SNR loss being greater over ten monthly spaced writes than a single write performed after one year. For both remanence and transition components the monthly spaced writes produce an SNR drop on a par with three yearly spaced adjacent track writes. Furthermore, unlike the result obtained for the same PRBS the loss of SNR per write does not appear to reduce resulting in both the monthly and yearly spaced data showing a constant decrease with further writes. This can be explained in the opposite manner to the decrease in SNR reduction with subsequent identical PRBS writes as, each time the adjacent write is performed, the data written to the encroachment region will vary resulting in an effect on the SNR of track one.

The observed difference between the same and varied PRBS each adjacent track write indicates that the use of the same PRBS to investigate the strength of the ATE is flawed. The more realistic scenario of a constantly varying PRBS for each adjacent track write includes the significant factor of a constantly varying data sequence being written to the encroachment region. When the PRBS is kept constant for each write the data written is reinforced provided only a small effect on track one which once the adjacent track is perfectly written will become negligible.

Figure 5.16 shows the change in SNR after each adjacent track write for immediate, monthly and yearly spaced writes for each of the simulated read head widths. The results show no difference in behaviour between the immediate and time spaced adjacent track writes indicating that there is no relationship between the strength of the SNR change due to ATE and the time evolution. Additionally these results clearly reveal the reduction of the SNR change for additional adjacent track writes of the same PRBS. Both Fig. 5.16a and Fig. 5.16c show the change in SNR, for all read head widths, tending towards zero. This further supports the previous point that investigating the effect of ATE requires variation in the written PRBS with each write in order to avoid artificially reducing the ATE strength as

more adjacent track writes are performed. The results for the varied PRBS show a greater scatter than when the same PRBS is used as expected. Furthermore these results show very little, if any, noticeable trend with the degree of SNR change appearing to show no change in behaviour with varying read head widths or increased adjacent track writes. This result indicates that the use of a natural logarithm to characterise the ATE may be insufficient once variations of the PRBS each write are taken into account.

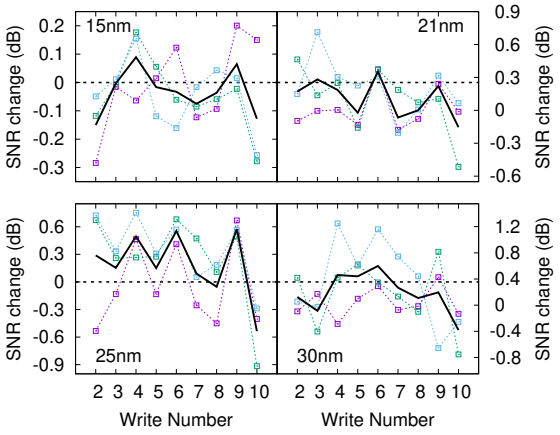

(a) Transition noise
Same PRBS

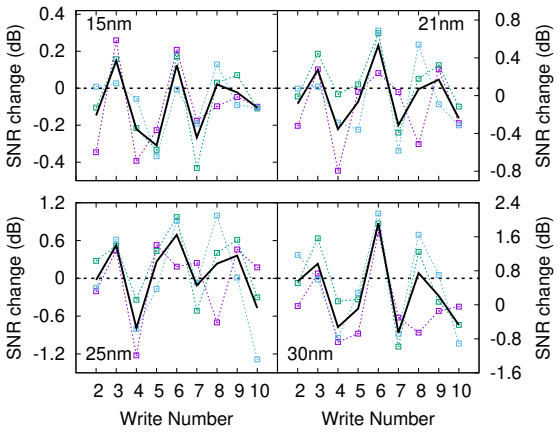

(b) Transition noise
Varied PRBS

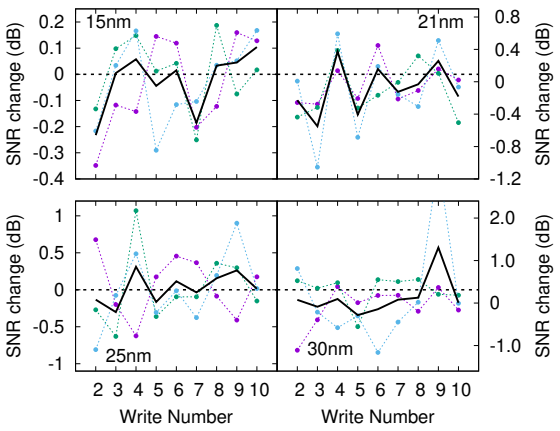

(c) Remanence noise
Same PRBS

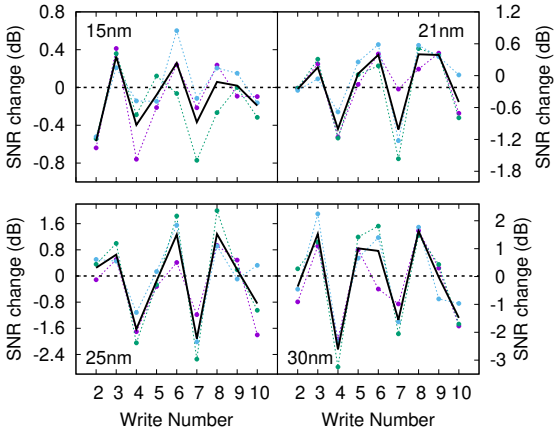

(d) Remanence noise
Varied PRBS

Fig. 5.16 Comparison of the SNR change due to each adjacent track write for immediate (purple), monthly (green) and yearly (blue) spaced writes. The average SNR change is indicated by the solid black line. Zero SNR change is represented by the dashed grey line.

5.8 Summary

The strength and effect of ATE (encroachment) has been investigated for the same PRBS each adjacent track write as well as for a different PRBS each adjacent track write. In order to characterise the effects on the system the signal-to-noise ratio has been used. The SNR has been obtained for both the remanence and transition noise in order to more clearly identify the effects of the ATE. Read back was performed for multiple read head widths in order to investigate the relationship between the read head width and A_{ATE}. The magnitude of A_{ATE} has been shown to be significantly greater for all read head widths when the PRBS is varied between each adjacent track write compared to the same PRBS used for each write. This is to be expected as there is additional variation in the data written to the encroachment area with each adjacent track write. The obtained change of A_{ATE} with varying read head widths has been explained through the overlap of the read head with adjacent tracks and unwritten regions. Additionally the change of overall SNR with different read head widths has been obtained. These results have shown that the SNR reaches a maximum when the read head width is equal to the track width. This result has been explained in a similar manner to those of A_{ATE} via the overlap of the read head on the different regions of the recording media. The loss of SNR due to the initial adjacent track write has been shown to be significantly greater than that of any subsequent adjacent track writes. Thus analysis of the ATE should be performed only after an initial adjacent track write has been performed.

The initial simulations focused on the characterisation of the ATE in line with the work performed by Natekar et al. [12]. The energy barrier for this system was $250\,k_BT$ and thus in order to expand the investigation into the effects of ATE in comparison to time decay a second system was simulated with an energy barrier of $80\,k_BT$. The comparison between the SNRs for these two systems showed that the decreased anisotropy resulted in an overall reduced SNR possibly arising from increased area of switchable grains for the same heated spot FWHM due to decreased coercivity. The increased region of switchable grains also appeared to reduce the strength of the relationship between the read head width and the magnitude of A_{ATE}. Additionally the reduced anisotropy system was shown to present a much stronger variation of the overall SNR for different read head widths as well as much greater SNR losses due to the initial adjacent track write compared to the ideal $L1_0$ FePt.

Time evolution simulations were performed with the SNR loss arising due to time decay compared to that due to ATE. For the reduced anisotropy system with an energy barrier of approximately $80\,k_BT$ these results suggest that the strength of time decay after one month is comparable in strength to nine adjacent track writes, when the SNR loss due to the initial adjacent track write is ignored. These results were then extended to show the loss of SNR

over time after various adjacent track writes in order to investigate any relationship between the stability of the data over time and the number of adjacent track writes. The results obtained show no apparent relationship between long term data stability and adjacent track write number with the gradient of the SNR over time remaining constant as the number of adjacent track writes was varied.

In order to further investigate any relationship between data stability and the number of adjacent track writes simulations of staggered writes were performed. In these simulations the system was evolved over time for one month or year before the next write process was performed. The comparison of the SNR between the monthly and yearly spaced writes showed that for the same PRBS each write the effect of the ATE was negligible with the SNR loss being equivalent between the monthly writes and a single write after a single year time evolution. Again the results when the PRBS was varied between writes showed different behaviour with the monthly spaced writes producing similar SNR loss as three yearly-spaced writes. This matches the behaviour seen in the initial results whereby the strength of the ATE is significantly greater when the PRBS is varied between writes. The results when the same PRBS was written revealed a reduction in the change of the SNR each write as additional writes were performed. This result suggests that the effect of writing the same PRBS to the adjacent track multiple times is reduced for each subsequent write due to the system approaching a perfectly written adjacent track as more writes are performed. Thus investigations into the ATE should avoid utilising the same PRBS for each adjacent track write. When the PRBS used for each staggered write was varied there was no noticeable reduction in the change of the SNR each write. The monthly spaced writes produced a significantly reduced SNR compared to the single adjacent track write after a one year time evolution. Thus there is a clear loss of SNR caused solely by the ATE.

6

Temperature dependence of ferromagnetic resonance linewidth

The key working principle of HAMR is the reduction of the recording medium's coercivity due to elevated temperatures. This temperature variation of the coercivity enables writing of high coercivity materials via heating of the granular structure prior to the write process. This then enables the use of much smaller grain sizes as the stability lost due to the reduced volume is compensated for by the greater coercivity. These smaller grain sizes in turn enable a reduction in the bit sizes used to store the data improving the overall areal density of the recording medium. As a result, with HAMR technology the production and release of 20 TB drives has been possible. The variation of the coercivity with temperature does however introduce additional challenges, such as those described in Chapter 4 where Curie point dispersion can result in reduced HAMR performance. A further challenge faced by HAMR resides in the thermal stability of the data, Chapter 5 investigated long term data stability, however, the thermal stability of the grains immediately after writing is also important The writing process in HAMR occurs within a specific range of the NFT in order to ensure that the coercivity is sufficiently low. It would be ineffective to perform the writing process whilst the grains were at or exceeding their Curie point due to their superparamagnetic nature, as such the write head to NFT spacing is set such that the write process occurs during the cooling phase of the grains. Additionally the spacing between the NFT and write head is set to produce optimal NFT efficiency as the proximity of the metallic pole damps the NFT resonance [10]. Furthermore investigations have been performed into the optimal level of heating required with respect to the recording medium's Curie point. Lyberatos and Guslienko have shown that it is specifically the rate at which the medium reaches the blocking temperature that has a major effect on the writing performance of HAMR [97, 88]. In addition to this it has been shown that the damping also plays a significant role in HAMR

performance. The magnitude of the damping has a direct influence on switching time of the magnetisation and as a result influences the degree to which the grains are aligned by the write head prior to reaching the blocking temperature [97, 98]. Lower damping reduces the ability for the grain's magnetisation to align with the write field prior to reaching the blocking temperature, resulting in reduced switching probabilities and, as a result, reduced write performance. Schrefl et al. [99] and Purnama et al. [100] have also shown that the damping has a significant effect on the magnetisation rate. As a result the lower the damping the more difficult it is for the moments to reverse [101]. Additionally decreasing damping also causes the coercivity field to increase [100]. Overall the damping is a key parameter influencing both the writing speeds and bit error rates of the recording medium and overall HAMR effectiveness [97, 102].

Recent experimental results obtained by Richardson et al. [15] have shown a decrease in the linewidth for increasing temperatures which was then related to a possible reduction in damping. This would create significant issues for HAMR due to the previously explained influence of damping on the signal-to-noise ratio and switching time. Richardson et al. proposed the cause for the apparent reduced damping to be a result of competition between two-magnon scattering and spin-flip magnon electron scattering. Strungaru et al. [16] performed a comprehensive investigation into the temperature dependence of damping for $L1_0$ FePt via atomistic spin dynamics. The obtained results showed no reduction in damping with temperature irrespective of grain size. Additionally Strungaru et al. developed a semi-analytical model which takes into account parameter distributions to produce field-swept ferromagnetic resonance (FMR) results. Using this model Strungaru et al. were able to reproduce the experimental results obtained by Richardson et al. showing a reduction in the linewidth as temperatures increased within 40 K of the Curie point. The proposed mechanism for the reduction in linewidth in [16] relies on inhomogeneous line broadening. The decreased linewidth results from the transition of the small grains into the paramagnetic regime at temperatures close to the grain's Curie point. The results obtained in [16] are based on a simplistic semi-analytical model of FMR. This model neglects many aspects such as magnetic interactions between grains; magnetostatic fields; thermal fluctuations. Using MARS it is possible to investigate the reduction of the linewidth that can arise at temperatures close to the Curie point while taking into account the numerous complexities not considered in the work performed by Strungaru et al. This chapter starts with an initial verification of the FMR simulations performed by MARS via an ensemble of identical grains compared to the analytical solution described by the Kittel formula. The inclusion of grain size distributions and its effect on linewidth is then investigated observing the experimental

decrease in linewidth at elevated temperatures. Finally, the significance of thermal noise and magnetostatic interactions, both of which were neglected by Strungaru et al., are investigated.

6.1 Ferromagnetic resonance

The ferromagnetic resonance simulations utilise an out-of-plane constant magnetic field, B, in addition to a sinusoidal oscillating in-plane magnetic field, B_{rf}, to perturb the magnetisation, this process is illustrated for a granular thin film in Fig. 6.1. The oscillating field induces

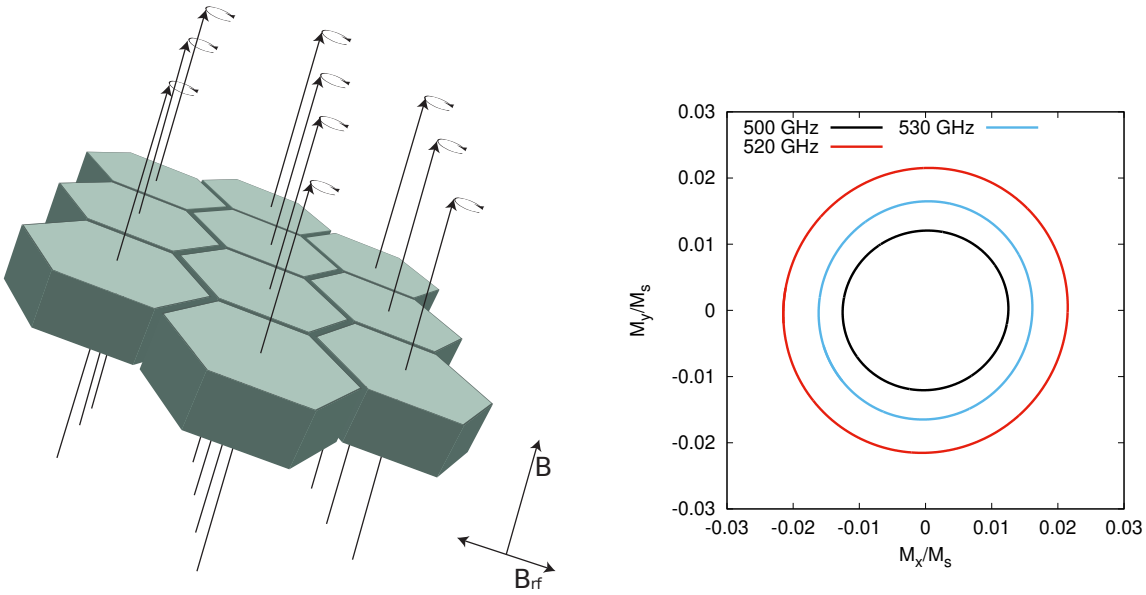

Fig. 6.1 Illustration of the FMR process for a granular thin film. The in-plane sinusoidal oscillating magnetic field induces oscillations in the grain magnetisation. The strength of the overall in-plane magnetisation varies with respect to the in-plane applied field frequency, with a maximum amplitude at the resonance frequency (518 GHz) as shown by the Lissajous figure on the right.

a coherent precession of the grain's magnetisation resulting in an oscillatory behaviour of the in-plane magnetisation. The magnitude of this in-plane magnetisation varies with the frequency of the in-plane applied field as shown by the Lissajous plot in Fig. 6.1. The maximum amplitude occurs at the resonance frequency which, for a known anisotropy, K_u, and magnetisation saturation, M_s, can be determined by the Kittel formula:

$$f_{res} = \frac{\gamma}{2\pi}\left(B + \frac{2K_u}{M_s}\right) \tag{6.1}$$

The power spectrum of the FMR can be obtained via squaring the Fourier transform of the in-plane magnetisation. The power spectrum for a single FePt grain at 0 K is shown in

Fig. 6.2. This spectrum can then be fitted by a Lorentzian curve:

$$L(x) = \frac{A}{\pi} \frac{0.5w}{(x - f_{res})^2 + (0.5w)^2} \tag{6.2}$$

where A is the amplitude, f_{res} is the resonant frequency and w is the full-width at half maximum (FWHM). The effective Gilbert damping can be obtained from the fitted Lorentzian via:

$$\alpha_G = \frac{0.5w}{f_{res}} \tag{6.3}$$

At 0 K the extracted damping should be equal to the input thermal bath coupling as shown in Eq. 2.28. This arises due to the lack of thermal scattering effects at this temperature. Hence the effective damping of the system will be given by the Gilbert damping which is equal to the thermal bath coupling in this case. The damping was successfully recovered via the FMR simulations shown in Fig. 6.2. For this simulation the thermal bath coupling was set to $\lambda = 0.025$. The damping obtained from simulation was within agreement with the input value within a 0.2 % error. The resonance peak should also occur at the frequency determined by the Kittel formula Eq. 6.1. The 0 K anisotropy was $9.21 \cdot 10^7$ erg/cm^3 with a saturation magnetisation of 1,051.65 emu/cm^3 with an out-of-plane field strength of 10 kOe. The resonance frequency obtained from the Kittel formula for these values is 518.4 GHz which agrees with the obtained resonance frequency within a 0.1 % error. The successful extraction of the damping and agreement of the resonance frequency clearly show the validity of the model.

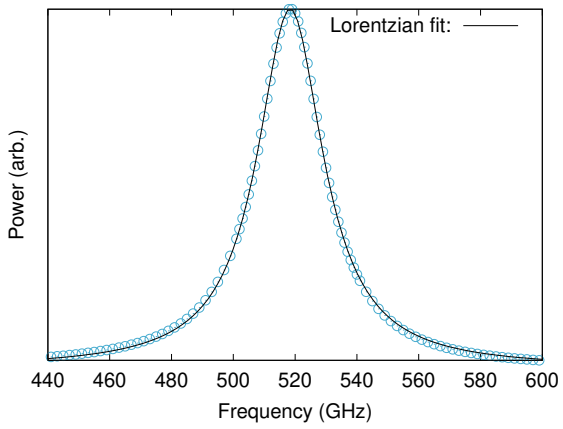

Fig. 6.2 Power spectrum for a single FePt grain at 0 K. The power spectrum is obtained by taking the squared amplitude of the Fourier transform of the in-plane magnetisation for each simulated frequency. The power spectrum is then fitted via a Lorentzian profile to obtain the input damping. The anisotropy can also be extracted via the Kittel formula (Eq. 6.1).

Figure 6.3 shows the change in resonant frequency with increased temperatures. This change in resonance occurs due to the thermal dependence of the anisotropy, magnetisation and damping as detailed in Chapter 2 and Chapter 3. With increasing temperatures the resonance frequency decreases, this is a result of the reduction in the anisotropy. Additionally the amplitude of the power spectrum also decreases with increasing temperatures, this is due to the reduction in the magnitude of the magnetisation which is captured by the LLB via the longitudinal relaxation of the magnetisation vector. The obtained spectra are in agreement with those obtained by Ostler at al. [103]. As a final verification for the model Figure 6.4 shows the obtained resonant frequencies and effective damping for an FePt system consisting of an ensemble of non-interacting identical grains for a range of temperatures. The obtained results show good agreement with the analytically predicted values. As the system temperature approaches the Curie point the difference between the obtained and expected value increases, this is due to the increased noise present in the system. The effects of this increased noise can be reduced by simulating a larger number of grains in order to average out the noise.

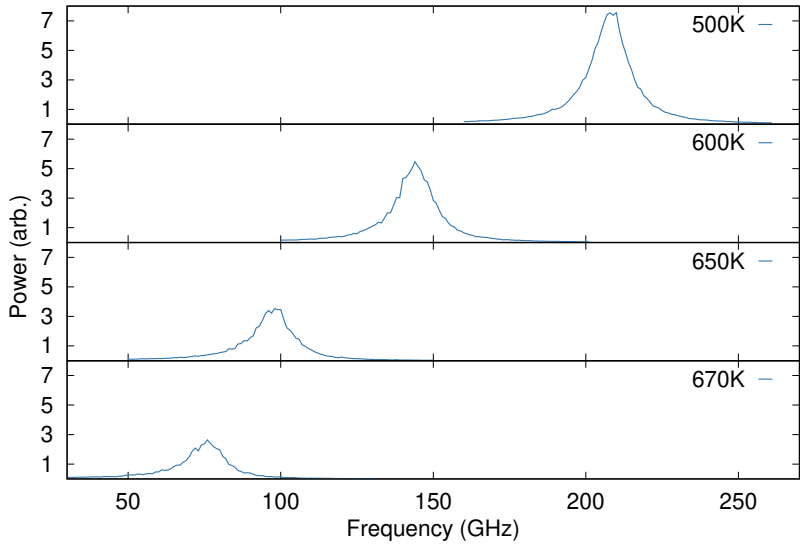

Fig. 6.3 Power spectrum for a single FePt grain at multiple temperatures. As the temperature is increased the resonance frequency is reduced this is due to the reduction in the anisotropy. The amplitude also falls with increasing temperature due to the reduction in the magnitude of the magnetisation.

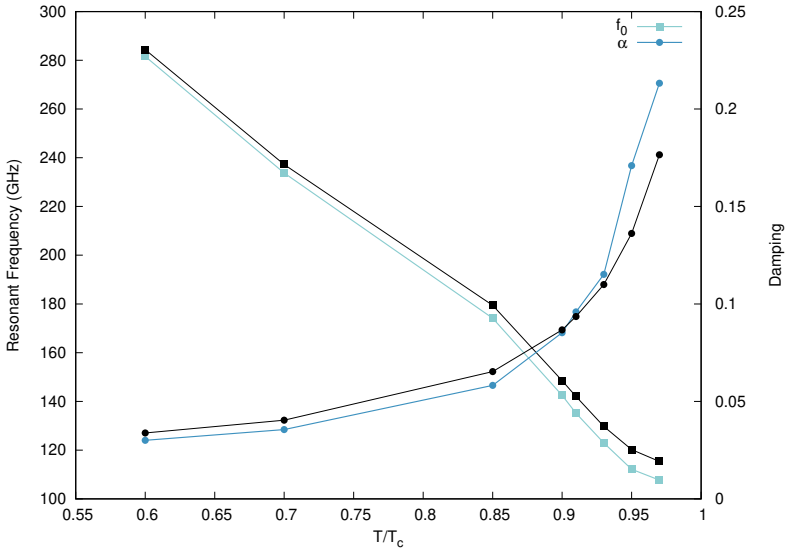

Fig. 6.4 Damping and resonance frequency as a function of temperature obtained via simulation (blue) for an ensemble of identical grains compared to analytically expected behaviour (black) for an input thermal bath coupling of 0.025.

6.2 Parameter distributions

The phenomenon of inhomogeneous line broadening appears in a system with a distribution of parameters which are present when dealing with granular recording media systems. Hence it is necessary to calculate the FMR spectrum in the presence of parameter distributions. Here a log-normal diameter distribution is included shown in Fig. 6.5a. The Curie point is described in the same manner as used in Chapter 4 via the relationship determined by Hovorka et al. [68] and detailed in Section 3.5. The obtained Curie point distribution is shown in Fig. 6.5b.

The concomitant Curie point distribution induces further parameter distributions in the system. A distribution of the magnetisation is induced via Eq. 3.8 or Eq. 3.9, while an anisotropy distribution is induced via the perpendicular susceptibilities dependence on the Curie point Eq. 3.11. Unlike the diameter and Curie point distribution the anisotropy distribution is temperature dependent. The anisotropy distribution is shown for multiple temperatures in Fig. 6.6. It is clear from this figure that as the system temperature begins to overlap with the Curie point distribution the anisotropy of the system approaches zero as is expected from the loss of magnetic order expected at the Curie point. It is this change in the anisotropy distribution which is proposed by Strungaru et al. to drive the reduction in the linewidth for temperatures close to the Curie point.

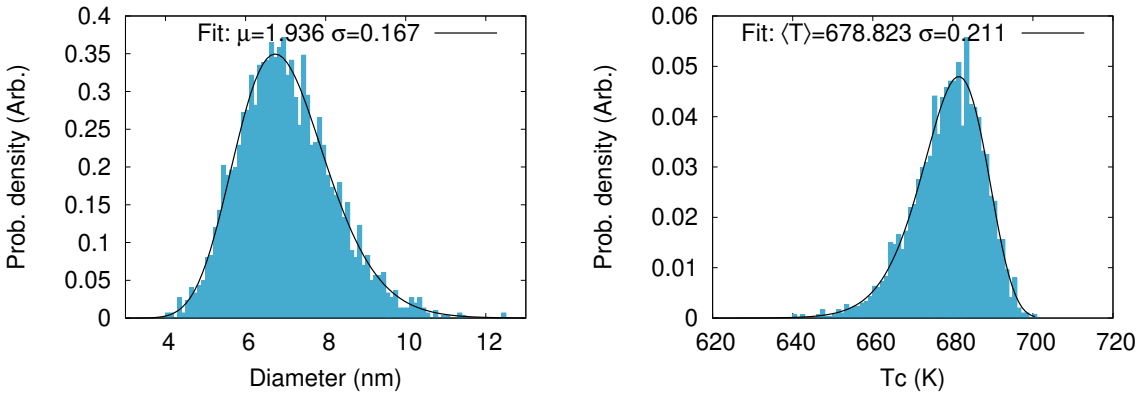

(a) Diameter distribution

(b) Curie point distribution

Fig. 6.5 Input grain size distribution (a) used to generate inhomogeneous line broadening in FMR simulations. The resultant Curie point distribution (b) is obtained via the relationship described in Section 3.5. Log-normal fits (black line) have been used to verify the population parameters.

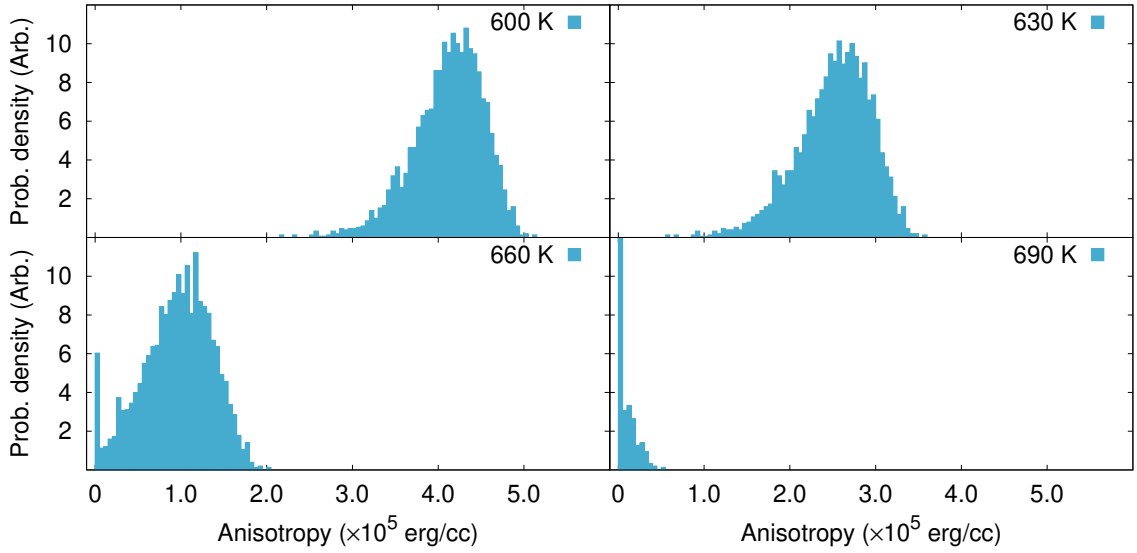

Fig. 6.6 Anisotropy distribution arising from Curie point distribution for various system temperatures.

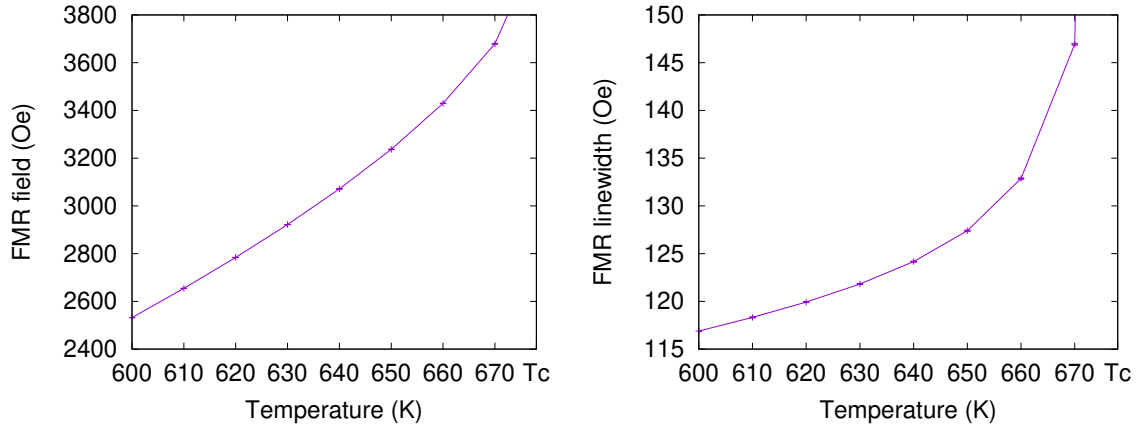

Fig. 6.7 Resonant field and linewidth for a system of identical grains for a range of temperatures in the absence of thermal noise.

6.3 Initial results

To investigate the presence and effect of inhomogeneous line broadening multiple field-swept FMR simulations were performed at different system temperatures. Prior to introducing parameter distributions, simulations were performed for a system of identical grains in order to verify the expected system behaviour. To extract the system's behaviour more easily at elevated temperatures these initial simulations were performed without thermal noise. The resonant field and linewidth as a function of system temperature are shown in Fig. 6.7. These results show the expected behaviour with the resonant field increasing with temperature due to the reduction in the anisotropy field. The system damping has been modelled via Eq. 2.28 and as such an increase in damping with temperature is expected, this is verified by the increasing linewidth shown in the results.

To investigate the effect of inhomogeneous line broadening the system of grains was changed to include a grain size distribution. The temperature range used for simulations was also set to range from 600 K to 690 K in order to cover the entire range of the concomitant Curie point distribution. The system parameters are provided in Table 6.1. The in-plane magnetisation of each grain was averaged and the fast Fourier transform (FFT) was performed on this average magnetisation. As the temperature was increased some grains would become superparamagnetic as the temperature exceeded their Curie point. Any grains whose Curie point was less than or equal to the system temperature were removed from the average magnetisation as superparamagnetic grains will not contribute to the resonance. The obtained power spectra for various system temperatures are provided in Fig. 6.8.

Table 6.1 Material parameters used for the FMR simulations performed within this chapter.

$\langle D \rangle$ (nm)	7.0		
σ_D	0.167		
ν	0.79		
d_0	0.71		
T_c^{∞} (K)	720.0		
$\langle T_c \rangle$ (K)	678.823		
Ms (emu/cc)	1051.65		
Critical exponent	0.3286		
α	0.01		
Susceptibility fit	Inverse susceptibility		
$1/\tilde{\chi}_{\parallel}$ (T)	$a_0 = 0.678382$	$a_{1/2} = -0.886067$	$a_1 = 22.8654$
	$a_2 = 94.9147$	$a_3 = -204.446$	$a_4 = 292.056$
	$a_5 = 0$	$a_6 = 0$	$a_7 = 0$
	$a_8 = 0$	$a_9 = 0$	
	$b_0 = 0.678382$	$b_1 = -17.4995$	$b_2 = 903.533$
	$b_3 = -10003$	$b_4 = 37119.6$	
$1/\tilde{\chi}_{\perp}$ (T)	$a_0 = 0.0917613$	$a_{1/2} = 0.310647$	$a_1 = 1.97732$
	$a_2 = -11.9930$	$a_3 = 48.1736$	$a_4 = -119.875$
	$a_5 = 183.095$	$a_6 = -165.796$	$a_7 = 80.0317$
	$a_8 = -14.2428$	$a_9 = -1.10490$	
	$b_0 = 0.0917613$	$b_1 = -1.771147$	$b_2 = 0$
	$b_3 = 0$	$b_4 = 0$	
Frequency (GHz)	12.0		
B_{rf} (Oe)	50.0		
B (kOe)	10.0		

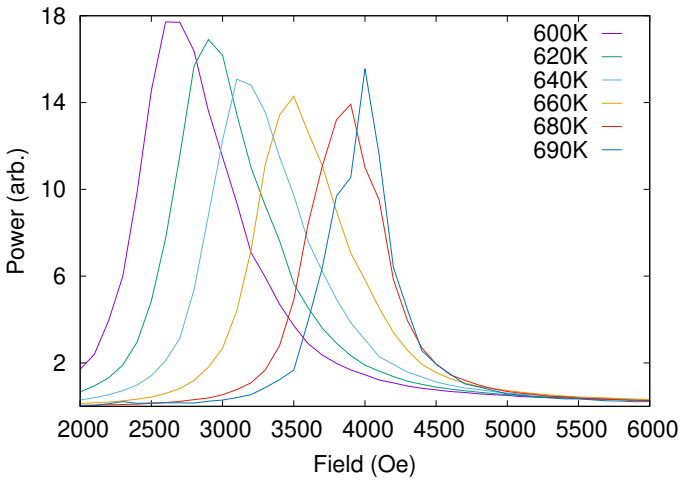

Fig. 6.8 Obtained power spectra obtained from field-swept FMR of an inhomogeneous system for different system temperatures.

The obtained results show the expected decrease of the resonance peak as the temperature is increased in agreement with the result obtained for the system of identical grains. The expected reduction in power with increasing temperature is also obtained as expected due to the reduction in the magnetisation length as the temperature is increased. The FMR field and linewidth are provided in Fig. 6.9. The obtained results show a significant deviation from those obtained for the system of identical grains. There is a clear reduction in the linewidth as the system temperature is increased. Thus these results show that the reduction in linewidth obtained within 40 K as observed by Richardson et al. arises due to the presence of inhomogeneous line broadening in agreement with the work performed by Strungaru et al. using the semi-analytical model.

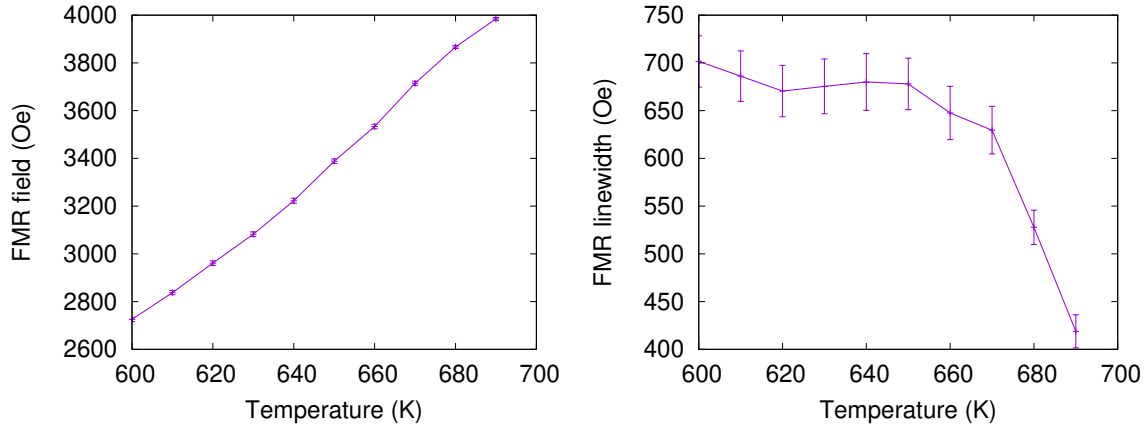

Fig. 6.9 Extracted resonance field (left) and linewidth (right) as a function of system temperature.

The linewidth has been shown to begin decreasing once the temperature is within 40 K of the Curie temperature. It should be noted that due to the dispersion of the Curie point there is no single value which can describe the Curie temperature of the entire system. Thus for a system of distributed Curie points the Gaussian average, $\langle Tc \rangle$, is referred to as the system's Curie temperature. For the simulated system this value was $\langle Tc \rangle = 678.8$ K as is shown in Fig. 6.5b. The obtained results show an almost constant linewidth between 600 K and 650 K. As the linewidth is expected to increase with damping and therefore temperature this result may suggest that prior to resulting in a decrease in linewidth the inhomogeneous line broadening may act against the the increased linewidth due to damping resulting in a quasi-static linewidth as a function temperature.

6.4 Effects of grain size

The concomitant Curie point distribution which arises due to the dependence of the Curie point on the grain diameter narrows as the average grain size is increased. Thus, for sufficiently large grains, the reduction of the linewidth at temperatures close to Tc due to inhomogeneous line broadening should vanish. To verify this, and also provide further evidence for the role of inhomogeneous line broadening as the driving factor for the linewidth reduction, a system of large grains has been simulated. The grain size and Curie point distributions are shown in Fig. 6.10a and Fig. 6.10b.

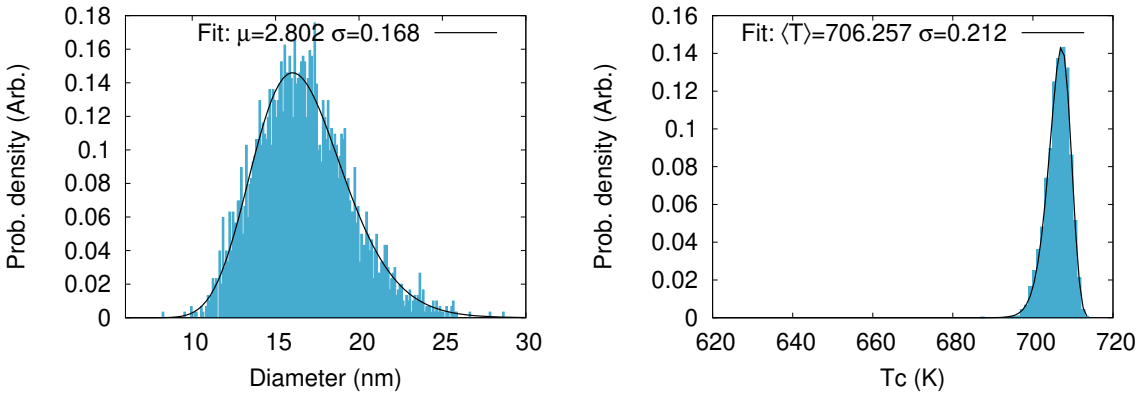

(a) Diameter distribution

(b) Curie point distribution

Fig. 6.10 Input grain size distribution (a) used to generate inhomogeneous line broadening in FMR simulations to investigate the effect of larger grains on linewidth reduction near Tc. The resultant Curie point distribution (b) is obtained via the relationship described in Section 3.5. Log-normal fits (black line) have been used to verify the population parameters.

It is clear that the width of the Curie point distribution is much smaller for the system with an average grain diameter of 15 nm than for the 7 nm system. The anisotropy distributions are shown for multiple different temperatures in Fig. 6.11. There is a significant reduction in the range of temperatures at which the anisotropy distribution includes superparamagnetic grains suggesting that there will be no observed reduction of the linewidth at temperatures close to the Curie temperature.

The FMR field and linewidth as a function of temperature are shown in Fig. 6.12. The obtained results show no decrease in linewidth at temperatures close to the Curie temperature of the system. In fact the result show the more expected behaviour with the linewidth increasing as the temperature approaches the Curie temperature which will be due to the sharp increase in the individual grain damping as described by Eq. 2.28

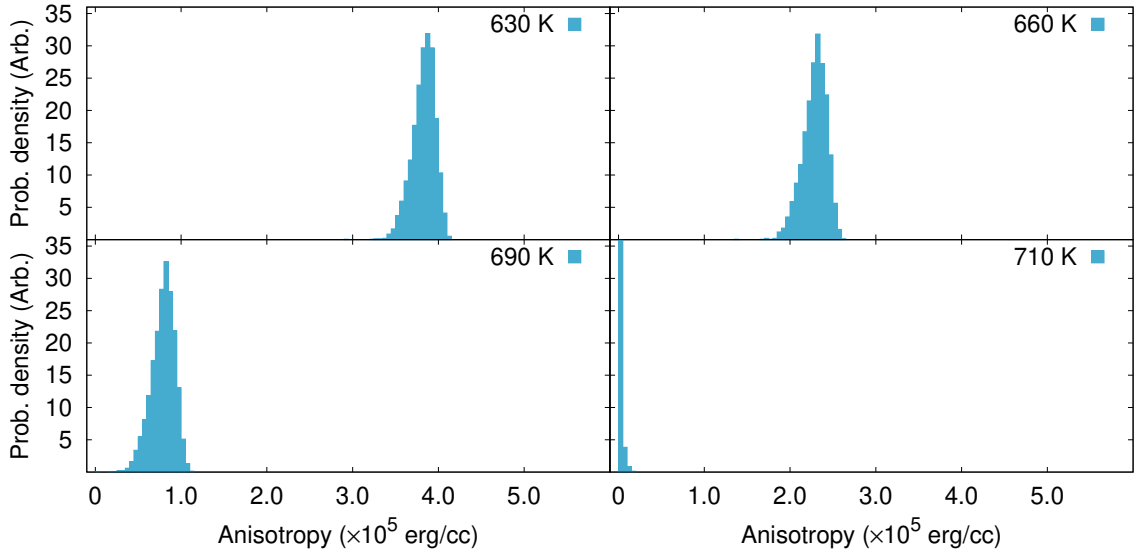

Fig. 6.11 Anisotropy distribution arising from Curie point distribution for various system temperatures.

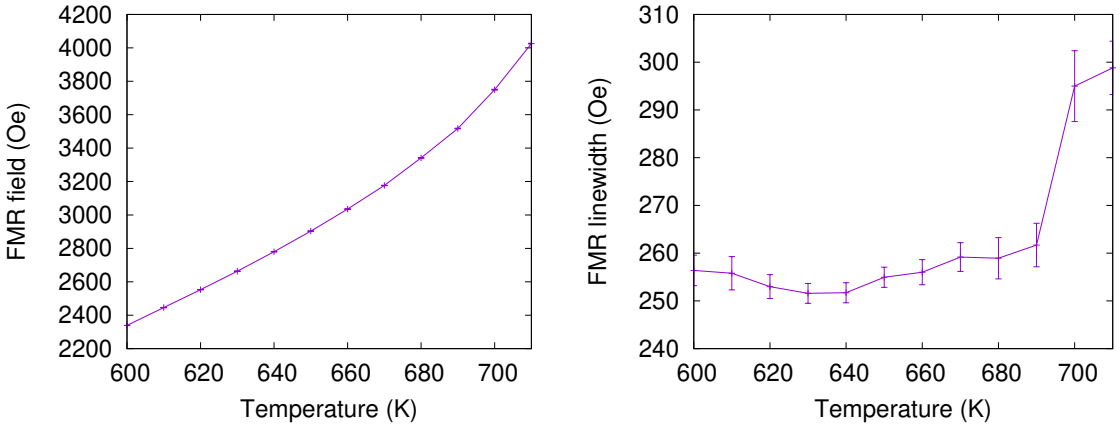

Fig. 6.12 Extracted resonance field (left) and linewidth (right) as a function of system temperature.

6.5 Effects of thermal noise

To simplify the simulated system in order to more clearly extract the driving factors of the change in linewidth the simulations have been repeated with the thermal noise terms described in Eq. 2.27 set to zero. Again grains whose Curie point is less than the system temperature are excluded from the average magnetisation and as a result the power spectra. The obtained power spectra are shown in Fig. 6.13.

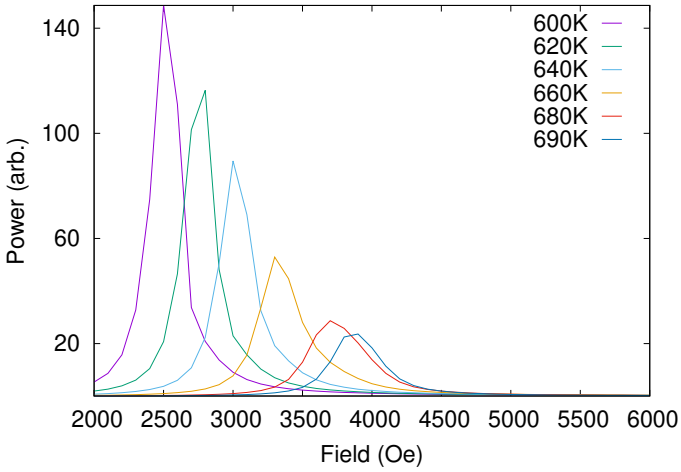

Fig. 6.13 Obtained power spectra obtained from field-swept FMR of an inhomogeneous system for different system temperatures with thermal noise removed.

These results show a much stronger reduction in the power with temperature than the previous results. This can be expected due to the absence of longitudinal fluctuations of the magnetisation leading to the reduction of the magnetisation with temperature matching the exactly that described by Eq. 3.8. The FMR field and linewidth obtained for each simulated temperature are provided in Fig. 6.14.

The FMR field shows the same gradient, however, the noiseless results show consistently smaller FMR fields. The behaviour of the linewidth with temperature shows a significant difference when the noise terms are neglected. Here there is a clear increase in the linewidth up until 680 K at which point the linewidth begins to sharply decrease. From this we can interpret that the effect of inhomogeneous line broadening becomes dominant over the increase in damping once the temperature reaches the Gaussian average of the Curie point distribution.

The overall linewidth obtained from the noiseless simulations reaches a maximum of around 420 Oe. This is on a par with the minimum linewidth obtained for the system with noise, showing that the thermal noise plays a significant role in the magnitude of the linewidth.

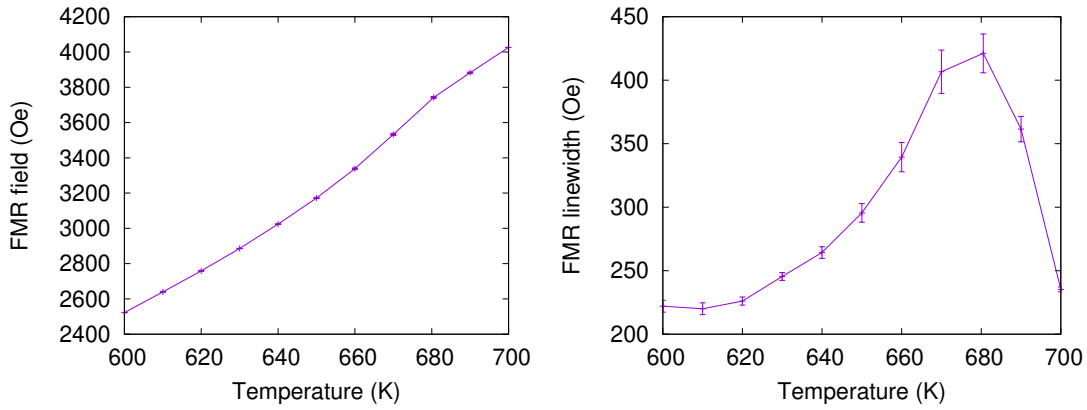

Fig. 6.14 Extracted resonance field (left) and linewidth (right) as a function of system temperature when thermal noise is excluded.

This thermal broadening arises from thermal fluctuations of the anisotropy [104]. These fluctuations result in an effective distribution of the anisotropy which in turn leads to an increased linewidth in a similar manner to that of inhomogeneous line broadening.

The anisotropy fluctuations are the result of fluctuations of the longitudinal component of the magnetisation. To verify that it is the longitudinal component that drives the thermal broadening the simulations have been repeated with only the longitudinal noise component of Eq. 2.26 included. The comparison of the results between the three simulated systems are provided in Fig. 6.15. The strong agreement between the results with and without the transverse noise components shows that the thermal broadening is driven by the longitudinal component of the noise.

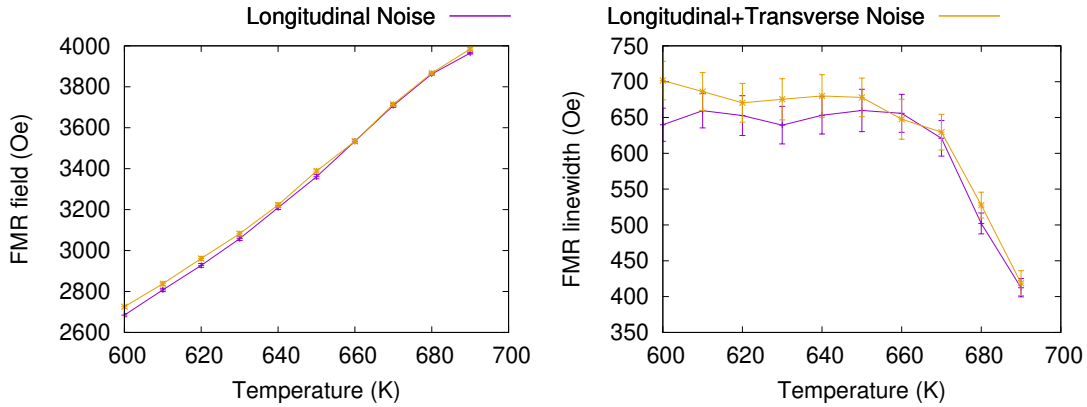

Fig. 6.15 Comparison of the FMR field and linewidth when transverse noise is accounted (yellow) for and when it is neglected (purple). The results show very similar behaviour indicated that it is indeed the longitudinal fluctuations which result in thermal broadening.

6.6 Effects of magnetostatic interactions

For thin film granular media each of the magnetic grains will experience magnetostatic interactions from their neighbouring grains. Depending on the strength of the magnetostatic interactions in relation to the applied field strengths there may be a change in the observed ferromagnetic resonance. For a system of identical grains the magnetostatic interactions will simply provide a constant additional force, increasing the coherent motion of the grains and thus increasing the strength of resonance. However, for an inhomogeneous system where there are multiple grain specific resonance frequencies and fields the presence of magnetostatic interactions may have a significant effect on the overall behaviour of the system.

To investigate the effects of the magnetostatic interactions the previous simulations have been repeated with the same system this time accounting for magnetostatic interactions via the dipole approximation. The obtained results are shown in Fig. 6.16. It is clear from these results that the magnetostatic interaction influences both the resonant field and also the linewidth, with both values showing increased values when interactions are accounted for. However, the results appear to converge as the system temperature is increased. This may arise due to the reduction in the number of ferromagnetic grains present as the system temperature increases. The superparamagnetic grains will have no effect on the FMR so increasing the system temperature effectively reduces the number of grains contributing to the resonance. As this number reduces so too does the strength of the interactions. Eventually the interactions become negligible at which point both systems produce identical results. The results appear to converge at 680 K which is around the Gaussian average of the Curie point distribution.

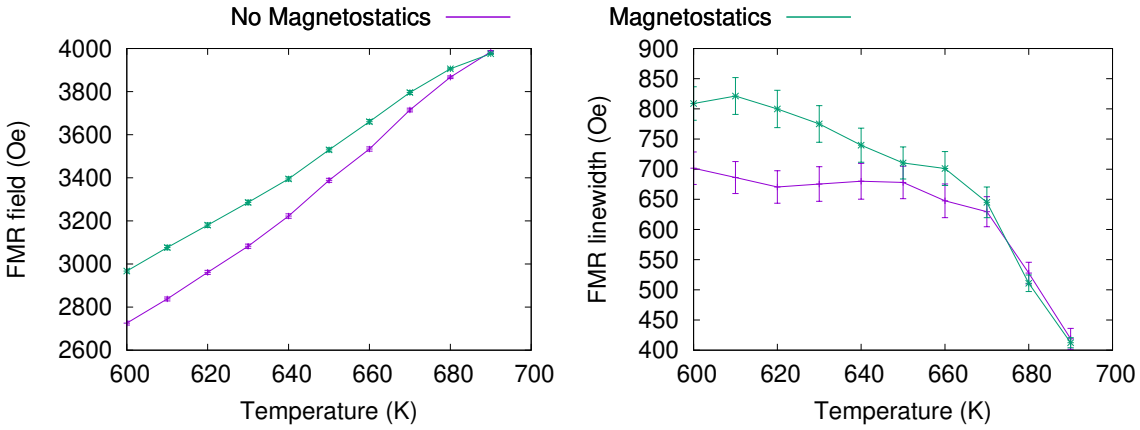

Fig. 6.16 Comparison of the temperature dependent FMR field and linewidth when magnetostatic interactions are accounted for.

6.7 Summary

Experimental results obtained by Richardson et al. have shown a decrease in the FMR power spectra linewidth at temperatures within 40 K of the systems Curie point [15]. The decrease in linewidth was attributed to a possible reduction in damping driven by the competition between two-magnon scattering and spin-flip magnon electron scattering. A simple semi-analytical model was developed by Strungaru et al. to investigate the reduction in linewidth close the Curie point [16]. The results obtained indicated that the reduction in linewidth was in fact driven by inhomogeneous line broadening and not due to the competition between magnon scattering types. Specifically, the presence of a Curie point distribution results in grains transitioning to the paramagnetic regime at a different temperatures. These paramagnetic grains do not contribute to the FMR causing the reduction in linewidth. Using MARS a more complex model of FMR with parameter distributions has been developed. This model can account for multiple parameter distribution as well as thermal fluctuations, magnetostatics and exchange interactions.

The results obtained by Strungaru et al. have been used to initially verify the performed FMR simulations. The simulated system consisted of a log-normal grain size distribution with the Curie point modelled via the relationship described by Hovorka et al. [68] and detailed in Section 3.5. The initial results show that a reduction of the linewidth occurs within 40 K of the Gaussian average of the Curie point distribution in agreement with the work of Richardson et al. and Strungaru et al. However, the results also show an increase in the individual grain damping as described by the LLB model specifically Eq. 2.28. This observation is in line with that of Strungaru et al. indicating that the reduction in the linewidth is driven by inhomogeneous line broadening. If inhomogeneous line broadening was the driving factor for the reduction of linewidth then a sufficient decrease in the width of the Curie point distribution should result in the loss of the observed decrease. Results obtained for a system of grains with an average grain diameter of 15 nm instead of the previous 7 nm show a complete loss of a reduction in the linewidth at temperatures close to the Curie point of the system. The results strengthen the evidence that the reduction is solely driven by inhomogeneous line broadening as proposed by Strungaru et al.

Due to the simple nature of the model developed by Strungaru et al. the effects of thermal fluctuations could not be investigated. The simulations performed for this work included the removal of all noise terms, followed by the removal on on the transverse noise terms. When all noise terms were removed the linewidth as a function of temperature showed a significantly different behaviour with the linewidth increasing from 600 K until 680 K followed by the previously observed decrease as temperatures increase. The observed initial

increase is attributed to the increase of the individual grain damping which can be observed for these simulations due to the absence of thermal broadening. Thermal noise has been shown to cause fluctuation in the grain's anisotropy [104]. It is these fluctuations in the anisotropy which give rise to the thermal broadening, which are driven by the fluctuations of the longitudinal magnetisation. The results obtained in the absence of transverse noise provide very close agreement to the results obtained when all noise terms are accounted for providing strong evidence that it is the fluctuation of the longitudinal magnetisation which gives rise to the thermal broadening.

Finally the influence of magnetostatic interactions on the temperature dependent FMR has been investigated. The obtained results show that the interactions act to increase both the resonant field and linewidth. However, the effect caused by the interactions has been shown to decrease as the system temperature increases. This behaviour arises due to the reduction of ferromagnetic grains present in the system as the temperature is increased. The fewer the number of ferromagnetic grains the smaller the strength of the magnetostatic interactions. The effect of the magnetostatic interactions becomes negligible at around 680 K which is the point at which most of the grains have become superparamagnetic. Overall while the presence of magnetostatic interactions generates increased FMR fields and linewidths it has no effect on the observed decrease of the linewidth with increasing temperatures due to inhomogeneous line broadening.

7

Conclusions

This chapter summarises the main conclusions of each of the previous results chapters. Following this, possible areas for expansion and future work are detailed.

MARS model development and validation

An open-source multi-scale multi-timescale micromagnetic code (called Models of Advanced Recording System (acronym MARS)) for simulating granular thin films has been developed. The MARS code is designed to model and simulate state of the art recording technologies, like HAMR, in addition to possible future recording media technologies such as heated dot magnetic recording. The key feature of the code is the inclusion of three micromagnetic solvers (Landau-Lifshitz-Gilbert, Landau-Lifshitz-Bloch and kinetic Monte Carlo) into a single C++ class. This implementation enables automatic transition between solvers based on the simulation requirements and system characteristics. Additionally the inclusion of the Landau-Lifshitz-Bloch enables the simulations of materials at and beyond their Curie points. Thus MARS is capable of performing multi-scale simulations such as a HAMR write process followed by long term data storage with read back performed at specified time intervals during storage. Such a simulation requires the use of the Landau-Lifshitz-Bloch due to the significance of thermal variation in HAMR as well as the kinetic Monte Carlo in order to obtain long timescale system evolution. Numerous tests have been performed for each of the included solvers in order to verify the code.

Semi-analytical model of switching probabilities for the determination of Curie point distributions

A semi-analytical model to determine Curie point distributions via thermo-remanence has been developed. A combination of the developed model and a grid-search based fitting procedure has been shown to successfully extract the Curie point distribution from input

thermo-remanence data provided by Seagate. The obtained results provide a strong case for the description of the Curie point distribution via the grain size distribution as determined by Hovorka et al. [68]. Additionally these results suggest that the magnitude of the Curie point dispersion obtained by the grains size distribution is of the correct order indicating that there is no significant additional source contributing to the Curie point dispersion. Thus, efforts to control and minimise the Curie point distribution should focus on the fabrication process of the recording medium with the specific aim of minimising the variation in grain sizes.

Adjacent track erasure

Using MARS the effect of adjacent track erasure and time decay on the SNR of a central track has been investigated. The initial simulations focused on the characterisation of the ATE in line with the work performed by Natekar et al. [12]. The obtained results revealed the importance of accounting for variations in the written PRBS. Writing the same PRBS for each adjacent write results in a reduction of SNR loss each write process as the adjacent track and encroachment region tends towards a perfectly written case. Thus future investigations into the importance of adjacent track erasure must utilise variations in the adjacent track PRBS for each adjacent track write.

The effect of time decay was investigated via kMC based time evolution simulations. After each write simulation the system was evolved over time for up to ten years. The obtained results showed no change in the rate of SNR loss over time due to the number of adjacent track writes. Furthermore the obtained results suggest that the SNR loss due to time evolution over one month was equivalent to nine adjacent track writes for a system with an energy barrier of approximately $80\,k_BT$.

Finally staggered adjacent track writes were simulated in order to investigate the SNR loss of a system which experiences both adjacent track erasure and time decay. The obtained results further support the necessity to vary the PRBS each adjacent track write due to the presence of a decreased reduction in SNR after each write when the same PRBS was used. When the same PRBS was used the effect of ten monthly spaced writes was equivalent to a single yearly spaced write. However, when the PRBS was varied the was a significantly larger reduction in SNR present between a year old system consisting of monthly spaced writes compared to a single yearly spaced write. Thus the effect of adjacent track erasure on the SNR is significant in comparison to time decay.

Temperature dependence of ferromagnetic resonance linewidth

Using MARS the presence of decreased FMR power spectrum linewidth at temperatures close to the Curie point has been investigated. The obtained results agreed with the

experimental results obtained by Richardson et al. [15] as well those obtained via the simple model developed by Strungaru et al. [16]. The performed simulations included a grain size distribution in line with those present in recording media. The Curie point of each grain was determined via the relationship described by Hovorka et al. [68] resulting in a concomitant Curie point distribution which in turn resulted in an anisotropy distribution. The individual grain damping increases with temperature as expected from the description used in the LLB model. Thus the presence of the reduction of the linewidth shows that inhomogeneous line broadening is the driving factor as suggested by Strungaru et al. and that it is not due to the competition between two-magnon scattering and spin-flip magnon electron scattering as suggested by Richardson et al. Furthermore, in support of inhomogeneous line broadening, when the average grain size was increased the presence of a reduction in the linewidth was lost. This result is explained by the more narrow Curie point distribution present reducing the temperature range at which the grains transition from the ferromagnetic to paramagnetic regime.

Owing to the much more complex model used in this work compared to the simple model developed by Strungaru et al. it was possible to investigate the presence and effect of thermal broadening. The obtained results revealed that thermal fluctuations result in increased linewidths. Further simulations involving the removal of the transverse noise terms showed that it is the fluctuations of the longitudinal magnetisation which drive the thermal line broadening. The importance of the longitudinal fluctuations is due to the induced fluctuations in the anisotropy [104].

The influence of magnetostatic interactions on the FMR was also investigated. The obtained results showed little to no change in the overall behaviour of the system. The presence of the magnetostatic interactions did result in increased FMR fields and linewidths, however as temperatures were increased the effect of the magnetostatics was reduced. This behaviour is due to the increasing proportion of grains entering the paramagnetic regime and thus not contributing to the FMR.

7.1 Future work

There are numerous aspects which are viable areas for additional research to expand on the work presented within this thesis. This section details the proposed areas of future work.

1) Implement improved magnetostatic model in MARS code

Currently the MARS code uses the tensorial form of the demagnetising field along with the dipole approximation due to its simple implementation. The method for the W-matrix

can be altered with no change to the computational cost of a single integration step due to the implemented tensorial form. As previously detailed the dipole approximation breaks down when the grains become elongated due to the assumption that the magnetisation is concentrated within the centre of the grain. Thus it is possible to improve the modelling of the magnetostatics by implementing a more accurate description of the W-matrix leading to increased computation during the determination of the W-matrix only. A viable improved method for the W-matrix is the surface-surface integral [105, 61]. This method integrates over the xy-surface of the grains in order to account for the shape of the grains.

2) Extend semi-analytical model to account for ECC media

The results obtained in Chapter 4, shown in Fig. 4.12, did not produce the required behaviour as the applied field strength was varied. This has been attributed to the use of ECC media in the experiments while the developed model assumes a single layer material only. The developed model can be expanded implementing a model for the energy barriers of bi-layer systems. The work performed by Paul Gavriloaea [83] showed it was possible to accurately describe the energy barrier of bi-layer systems using Eq. 4.6. Thus incorporating this energy barrier model into the developed semi-analytical model should enable the correct description of the thermoremanence as the applied field strength is varied. As result the semi-analytical model would then be capable of also describing ECC systems.

3) Account for Gaussian noise in read head location for ATE simulations

The results presented in Chapter 5 utilised a perfect read head in order more clearly reveal the noise contribution due to ATE and time evolution. However, in realistic HAMR devices the placement of the read head is not ideal and a Gaussian noise term adjusting the read head position can be used to model a more realistic read back system. Implementing a more realistic read head model would enable the significance of both ATE and time evolution on the obtained SNR to be more clearly defined in a production device. Such an improvement would also enable more direct comparison of the simulated result with those obtained via hardware testing.

4) Implement realistic variation in write field rise and fall time

In production HAMR devices the write field is generated via an electromagnetic write pole. Variations present in the formation of the write field when a current is applied to the pole piece results in variations in the rise and fall time of the write field. This variation in the time taken to change the write field will result in jitter due to differences in the expected and achieved bit transitions. Implementation of this noise source will enable investigations

into the comparison of the jitter which arises due to Curie point distributions and that which arises due to the magnetic pole piece.

5) Investigate the role of grain size, magnetostatic and exchange interactions on the ATE

The results obtained in this work focus on a systems with no magnetostatic or exchange interactions. Due to the nature of the HAMR write process the obtained magnetisation as the heated grains cool may be highly influenced by the surrounding grains via interactions. This could result in a significantly different effect of the ATE on the central track. Future work should focus on the effects of magnetostatics and exchange interactions including a varying combinations of both mechanisms. Additionally only one grain size distribution was used in the performed simulations, simulating systems with various grain sizes and distributions would enable more insight into the method by which ATE affects the central track SNR.

References

[1] V. Poulsen. Method of recording and reproducing sounds or signals, U.S. Patent 661,619, Nov. 1900.

[2] https://www.sony.com/en/SonyInfo/News/Press/201404/14-044E/. Accessed: 2021-07-24.

[3] https://insic.org/areal-density-chart/. Accessed: 2021-07-24.

[4] https://www.ibm.com/ibm/history/exhibits/storage/storage_350.html. Accessed: 2021-07-23.

[5] S. Iwasaki and Y. Nakamura. An analysis for the magnetization mode for high density magnetic recording. *IEEE Transactions on Magnetics*, 13(5):1272–1277, 1977.

[6] H. J. Richter, A. Lyberatos, U. Nowak, R. F. L. Evans, and R. W. Chantrell. The thermodynamic limits of magnetic recording. *Journal of Applied Physics*, 111(3):033909, 2012.

[7] K. Matsumoto, A. Inomata, and S. Y. Hasegawa. Thermally assisted magnetic recording. *Fujitsu Scientific and Technical Journal*, 42(1):158–167, 2006.

[8] https://blog.seagate.com/business/seagate-continues-to-lead-as-hamr-technology-advances/. Accessed: 2021-07-20.

[9] A. Datta and X. Xu. Infrared near-field transducer for heat-assisted magnetic recording. *IEEE Transactions on Magnetics*, 53(12):1–5, 2017.

[10] W. A. Challener, C. Peng, A. V. Itagi, D. Karns, W. Peng, Y. Peng, X. Yang, X. Zhu, N. J. Gokemeijer, Y. T. Hsia, G. Ju, R. E. Rottmayer, M. A. Seigler, and E. C. Gage. Heat-assisted magnetic recording by a near-field transducer with efficient optical energy transfer. *Nature Photonics*, 3(4):220–224, 2009.

[11] C. B. Rong, D. Li, V. Nandwana, N. Poudyal, Y. Ding, Z. L. Wang, H. Zeng, and J. P. Liu. Size-dependent chemical and magnetic ordering in $L1_0$-FePt nanoparticles. *Advanced Materials*, 18(22):2984–2988, 2006.

[12] N. A. Natekar and R. H. Victora. Analysis of adjacent track erasure in the HAMR media. *IEEE Transactions on Magnetics*, 57(3), 2020.

[13] D. Weller and A. Moser. Thermal effect limits in ultrahigh-density magnetic recording. *IEEE Transactions on Magnetics*, 35(6):4423–4439, 1999.

[14] R. F. L. Evans, W. J. Fan, P. Chureemart, T. A. Ostler, M. O. A. Ellis, and R. W. Chantrell. Atomistic spin model simulations of magnetic nanomaterials. *Journal of Physics: Condensed Matter*, 26(10):103202, Feb 2014.

[15] D. Richardson, S. Katz, J. Wang, Y. K. Takahashi, K. Srinivasan, A. Kalitsov, K. Hono, A. Ajan, and M. Mingzhong. Near-Tc ferromagnetic resonance and damping in FePt-based heat-assisted magnetic recording media. *Physical Review Applied*, 10(5):54046, 2018.

[16] M. Strungaru, S. Ruta, R. F. L. Evans, and R. W. Chantrell. Model of magnetic damping and anisotropy at elevated temperatures: Application to granular FePt films. *Physical Review Applied*, 14(1):1, 2020.

[17] V. Blum, R. Gehrke, F. Hanke, P. Havu, V. Havu, X. Ren, K. Reuter, and M. Scheffler. Ab initio molecular simulations with numeric atom-centered orbitals. *Computer Physics Communications*, 180(11):2175–2196, 2009.

[18] W. F. Brown. *Micromagnetics*. Interscience Tracts of Physics and Astronomy 18. Interscience Publishers (Wiley & Sons), 1963.

[19] W. Heisenberg. On the theory of ferromagnetism. *Zeitschrift für Physik*, 49:619–636, 1928.

[20] M. J. Donahue and D. G. Porter. OOMMF user's guide version 1.0. Technical Report nteragency Report NISTIR 6376, National Institute of Standards and Technology, Gaithersburg, MD, Sept 1999.

[21] A. Vansteenkiste, J. Leliaert, M. Dvornik, M. Helsen, F. Garcia-Sanchez, and B. Van Waeyenberge. The design and verification of mumax3. *AIP Advances*, 4(10):107133, 2014.

[22] http://www.suessco.com/simulations/magnum-fe/. Accessed: 2021-09-04.

[23] https://nmag-project.github.io/index.html. Accessed: 2021-09-04.

[24] http://magnetism.eu/43-software.html. Accessed: 2021-09-04.

[25] J. Leliaert, M. Dvornik, J. Mulkers, J. De Clercq, M. V. Milošević, and B. Van Waeyenberge. Fast micromagnetic simulations on GPU - recent advances made with mumax3. *Journal of Physics D: Applied Physics*, 51(12):123002, 2018.

[26] T. L. Gilbert. *Formulation, Foundations and Applications of the Phenomenological Theory of Ferromagnetism.* PhD thesis, Illinois Institute of Technology, June 1956.

[27] D. A. Garanin. Fokker-Planck and Landau-Lifshitz-Bloch equations for classical ferromagnets. *Physical Review B*, 55:3050–3057, Feb 1997.

[28] U. Atxitia, O. Chubykalo-Fesenko, N. Kazantseva, D. Hinzke, U. Nowak, and R. W. Chantrell. Micromagnetic modeling of laser-induced magnetization dynamics using the Landau-Lifshitz-Bloch equation. *Applied Physics Letters*, 91(23):232507, Dec 2007.

[29] A. H. Morrish. *The Physical Principles of Magnetism*. Wiley-IEEE Press, 1st edition, 2001.

[30] T. L. Gilbert and J. M. Kelly. Anomalous rotational damping in ferromagnetic sheets. In *Conference on Magnetism and Magnetic Materials*, Pittsburgh, PA, 1955.

[31] W. M. Saslow. Landau–Lifshitz or Gilbert damping? That is the question. *Journal of Applied Physics*, 105(7):07D315, 2009.

[32] P. Curie. *Propriétés magnétiques des corps a diverses températures*. Gauthier-Villars et fils, 1895.

[33] D. A. Garanin and O. Chubykalo-Fesenko. Thermal fluctuations and longitudinal relaxation of single-domain magnetic particles at elevated temperatures. *Physical Review B - Condensed Matter and Materials Physics*, 70(21):1–4, 2004.

[34] O. Chubykalo-Fesenko, U. Nowak, R. W. Chantrell, and D. Garanin. Dynamic approach for micromagnetics close to the Curie temperature. *Physical Review B*, 74:094436, Sept 2006.

[35] F. Bloch. Nuclear induction. *Physical Review*, 70:460–474, Oct 1946.

[36] R. F. L. Evans, D. Hinzke, U. Atxitia, U. Nowak, R. W. Chantrell, and O. Chubykalo-Fesenko. Stochastic form of the Landau-Lifshitz-Bloch equation. *Physical Review B*, 85:014433, Jan 2012.

[37] E. C. Stoner and E. P. Wohlfarth. A mechanism of magnetic hysteresis in heterogeneous alloys. *Philosophical Transactions of the Royal Society A*, 240(826):599–642, 1948.

[38] H. Pfeiffer. Determination of anisotropy field distribution in particle assemblies taking into account thermal fluctuations. *Physica Status Solidi (A) Applications and Materials Science*, 118(1):295–306, 1990.

[39] W. F. Brown. Thermal fluctuations of a single-domain particle. *Physical Review*, 130(5):1677–1686, Apr 1963.

[40] L. Néel. Théorie du traînage magnétique des ferromagnétiques en grains fins avec applications aux terres cuites. *Annals of Geophysics*, 5:99–136, 1949.

[41] R. W. Chantrell, N. Walmsley, J. Gore, and M. Maylin. Calculations of the susceptibility of interacting superparamagnetic particles. *Physical Review B*, 63(2):024410, 2001.

[42] H. Li and J.-G.Zhu. Understanding the impact of T_c and H_k variation on signal-to-noise ratio in heat-assisted magnetic recording. *Journal of Applied Physics*, 115(17):17B744, 2014.

[43] J.-G. Zhu and H. Li. Understanding signal and noise in heat assisted magnetic recording. *IEEE Transactions on Magnetics*, 49(2):765–772, 2013.

[44] K. Eason, H. T. Wang, M. R. Elidrissi, B. Xu, Z. Yuan, and K. S. Chan. Recording performance and comparison of graded-T_c and - K_u hamr systems. *IEEE Transactions on Magnetics*, 50(3):107–113, 2014.

[45] R. H. Victora and P.-W. Huang. Simulation of heat-assisted magnetic recording using renormalized media cells. *IEEE Transactions on Magnetics*, 49(2):751–757, 2013.

[46] H. X. Zhu, S. M. Thorpe, and A. H. Windle. The geometrical properties of irregular two-dimensional Voronoi tessellations. *Philosophical Magazine A: Physics of Condensed Matter, Structure, Defects and Mechanical Properties*, 81(12):2765–2783, 2001.

[47] J. L. Grenestedt and K. Tanaka. Influence of cell shape variations on elastic stiffness of closed cell cellular solids. *Scripta Materialia*, 40(1):71–77, 1998.

[48] S. Lloyd. Least squares quantization in PCM. *IEEE Transactions on Information Theory*, 28(2):129–137, 1982.

[49] Y. Liu, W. Wang, B. Lévy, F. Sun, D.-M. Yan, L. Lu, and C. Yang. On centroidal Voronoi tessellation—energy smoothness and fast computation. *ACM Transactions on Graphics*, 28(4), Sept 2009.

[50] A. Fazekas, R. Dendievel, L. Salvo, and Y. Bréchet. Effect of microstructural topology upon the stiffness and strength of 2D cellular structures. *International Journal of Mechanical Sciences*, 44(10):2047–2066, 2002.

[51] A. Gervois, L. Oger, P. Richard, and J. P. Troadec. Voronoi and radical tessellations of packings of spheres. In Peter M. A. Sloot, Alfons G. Hoekstra, C. J. Kenneth Tan, and Jack J. Dongarra, editors, *Computational Science — ICCS 2002*, pages 95–104, Berlin, Heidelberg, 2002.

[52] S.-P. Yu, Y.-H. Liu, A.-C. Sun, and J.-H. Hsu. Determining the size distribution of magnetic nanoparticles based on analysis of magnetization curves. *Journal of Applied Physics*, 106(10):103905, 2009.

[53] D. Weller, G. Parker, O. Mosendz, E. Champion, B. Stipe, X. Wang, T. Klemmer, G. Ju, and A. Ajan. A HAMR media technology roadmap to an areal density of $4\,Tb/in^2$. *IEEE Transactions on Magnetics*, 50:1–8, 2014.

[54] G. Ju, H. Zhou, R. W. Chantrell, B. Lu, and D. Weller. Direct probe of anisotropy field dispersion in perpendicular media. *Journal of Applied Physics*, 99(8):083902, 2006.

[55] J. Alsayednoor and P. Harrison. Evaluating the performance of microstructure generation algorithms for 2-d foam-like representative volume elements. *Mechanics of Materials*, 98:44–58, 2016.

[56] C. H. Rycroft. VORO++: A three-dimensional voronoi cell library in C++. *Chaos*, 19(4):041111, 2009.

[57] D. Weller, G. Parker, O. Mosendz, A. Lyberatos, D. Mitin, N. Y. Safonova, and M. Albrecht. Review article: FePt heat assisted magnetic recording media. *Journal of Vacuum Science & Technology B, Nanotechnology and Microelectronics: Materials, Processing, Measurement, and Phenomena*, 34(6):060801, 2016.

[58] Y. Peng, X. W. Wu, J. Pressesky, G. P. Ju, W. Scholz, and R. W. Chantrell. Cluster size and exchange dispersion in perpendicular magnetic media. *Journal of Applied Physics*, 109(12):123907, 2011.

[59] V. Sokalski, D. E. Laughlin, and J.-G. Zhu. Experimental modeling of intergranular exchange coupling for perpendicular thin film media. *Applied Physics Letters*, 95(10):102507, 2009.

[60] M. O. A. Ellis, R. V. Ababei, R. Wood, R. F. L. Evans, and R. W. Chantrell. Manifestation of higher-order inter-granular exchange in magnetic recording media. *Applied Physics Letters*, 111(8):082405, 2017.

[61] S. I. Ruta. *Study of interaction effects in magnetic granular systems for recording media application*. PhD thesis, University of York, Sept 2017.

[62] H. B. Callen and E. Callen. The present status of the temperature dependence of magnetocrystalline anisotropy, and the l (l + 1) 2 power law. *Journal of Physics and Chemistry of Solids*, 27(8):1271–1285, 1966.

[63] O. N. Mryasov, U. Nowak, K. Y. Guslienko, and R. W. Chantrell. Temperature-dependent magnetic properties of FePt: Effective spin hamiltonian model. *Europhysics Letters*, 69(5):805–811, 2005.

[64] M. O. A. Ellis. *Simulations of magnetic reversal in granular recording media*. PhD thesis, University of York, Sept 2015.

[65] C. Vogler, C. Abert, F. Bruckner, and D. Suess. Landau-Lifshitz-Bloch equation for exchange-coupled grains. *Physical Review B*, 90:214431, Dec 2014.

[66] H. Li and J. Zhu. The role of media property distribution in HAMR SNR. *IEEE Transactions on Magnetics*, 49(7):3568–3571, 2013.

[67] J.-G. (Jimmy) Zhu and H. Li. Signal-to-noise ratio impact of grain-to-grain heating variation in heat assisted magnetic recording. *Journal of Applied Physics*, 115(17):17B747, 2014.

[68] O. Hovorka, S. Devos, Q. Coopman, W. J. Fan, C. J. Aas, R. F. L. Evans, X. Chen, G. Ju, and R. W. Chantrell. The curie temperature distribution of FePt granular magnetic recording media. *Applied Physics Letters*, 101(5):052406, 2012.

[69] N. Kazantseva, D. Hinzke, U. Nowak, R. W. Chantrell, U. Atxitia, and O. Chubykalo-Fesenko. Towards multiscale modeling of magnetic materials: Simulations of FePt. *Physical Review B*, 77:184428, May 2008.

[70] P. J. Flanders and M. P. Sharrock. An analysis of time-dependent magnetization and coercivity and of their relationship to print-through in recording tapes. *Journal of Applied Physics*, 62(7):2918–2928, 1987.

[71] R. W. Chantrell, G. N. Coverdale, and K. O'Grady. Time dependence and rate dependence of the coercivity of particulate recording media. *Journal of Physics D: Applied Physics*, 21(9):1469–1471, Sept 1988.

[72] A. Meo, W. Pantasri, W. Daeng-Am, S. E. Rannala, S. I. Ruta, R. W. Chantrell, P. Chureemart, and J. Chureemart. Magnetization dynamics of granular heat-assisted magnetic recording media by means of a multiscale model. *Physical Review B*, 102(17):174419, 2020.

[73] G. Ju, Y. Peng, E. K. C. Changa, Y. Ding, A. Q. Wu, X. Zhu, Y. Kubota, T. J. Klemmer, H. Amini, L. Gao, Z. Fan, T. Rausch, P. Subedi, M. Ma, S. Kalarickal, C. J. Rea, D. V. Dimitrov, P.-W. Huang, K. Wang, X. Chen, C. Peng, W. Chen, J. W. Dykes, M. A. Seigler, E. C. Gage, R. W. Chantrell, and J. U. Thiele. High density heat-assisted magnetic recording media and advanced characterization - progress and challenges. *IEEE Transactions on Magnetics*, 51(11), 2015.

[74] K. Hono, Y. K. Takahashi, G. Ju, J. U. Thiele, A. Ajan, X. M. Yang, R. Ruiz, and L. Wan. Heat-assisted magnetic recording media materials. *MRS Bulletin*, 43(2):93–99, 2018.

[75] Y. Kubota, Y. Peng, Y. Ding, E. K. C. Chang, L. Gao, F. Zavaliche, T. J. Klemmer, S. Zhu, X. Zhu, P.-W. Huang, A. Q. Wu, H. Amini, S. Granz, T. Rausch, C. J. Rea, J. Qiu, H. Yin, M. A. Seigler, Y. Chen, G. Ju, and J. U. Thiele. Heat-assisted magnetic recording's extensibility to high linear and areal density. *IEEE Transactions on Magnetics*, 54(11):0–5, 2018.

[76] X. Wang, K. Z. Gao, J. Hohlfeld, and M. Seigler. Switching field distribution and transition width in energy assisted magnetic recording. *Applied Physics Letters*, 97(10):102502, 2010.

[77] S. Pisana, S. Jain, J. W. Reiner, G. J. Parker, C. C. Poon, O. Hellwig, and B. C. Stipe. Measurement of the Curie temperature distribution in FePt granular magnetic media. *Applied Physics Letters*, 104(16):162407, 2014.

[78] A. Chernyshov, T. Le, B. Livshitz, O. Mryasov, C. Miller, R. Acharya, and D. Treves. Measurement of Curie temperature distribution relevant to heat assisted magnetic recording. *Journal of Applied Physics*, 117(17):17–111, 2015.

[79] A. F. Manchón-Gordón, L. M. Moreno-Ramírez, J. J. Ipus, J. S. Blázquez, C. F. Conde, V. Franco, and A. Conde. A procedure to obtain the parameters of Curie temperature distribution from thermomagnetic and magnetocaloric data. *Journal of Non-Crystalline Solids*, 520:119460, Sept 2019.

[80] J. Waters, A. Berger, D. Kramer, H. Fangohr, and O. Hovorka. Identification of Curie temperature distributions in magnetic particulate systems. *Journal of Physics D: Applied Physics*, 50(35):35–36, 2017.

[81] N. Kazantseva, D. Hinzke, R. W. Chantrell, and U. Nowak. Linear and elliptical magnetization reversal close to the curie temperature. *EPL*, 86(2):27006, May 2009.

[82] J. Bergstra and Y. Bengio. Random search for hyper-parameter optimization. *Journal of Machine Learning Research*, 13:281–305, 2012.

[83] P. I. Gavriloaea. Minimum energy paths in spin chain systems. Master's thesis, University of York, Dec 2020.

[84] C. Rea, P. Czoschke, P. Krivosik, V. Sapozhnikov, S. Granz, J. Zhu, Y. Peng, J. U. Thiele, G. Ju, and M. Seigler. High track pitch density for HAMR recording: 1M TPI. *IEEE Transactions on Magnetics*, 55(3), 2019.

[85] S. Kalarickal, A. Tsoukatos, S. Hernandez, C. Hardie, and E. Gage. Adjacent track interference in heat-assisted magnetic recording: Impact and implications. *IEEE Transactions on Magnetics*, 55(7):2019–2022, 2019.

[86] B. S. D. Ch. S. Varaprasad, Y. K. Takahashi, and K. Hono. Microstructure control of $L1_0$-ordered FePt granular film for heat-assisted magnetic recording (HAMR) media. *JOM*, 65(7):853–861, 2013.

[87] D. Weller, A. Moser, L. Folks, M. E. Best, W. Lee, M. F. Toney, and M. Schwickert. High K_u materials approach to 100 $Gbits/in^2$. *IEEE Transactions on Magnetics*, 36(1 PART 1):10–15, 2000.

[88] M. H. Kryder, E. C. Gage, T. W. McDaniel, W. A. Challener, R. E. Rottmayer, G. Ju, Y.-T. Hsia, and M. F. Erden. Heat assisted magnetic recording. *Proceedings of the IEEE*, 96(11):1810–1835, 2008.

[89] D. Weller, O. Mosendz, G. Parker, S. Pisana, and T. S. Santos. $L1_0$ FePtX-Y media for heat-assisted magnetic recording. *Physica Status Solidi (A) Applications and Materials Science*, 210(7):1245–1260, 2013.

[90] N. H. Bertram, H. Zhou, and R. Gustafson. Signal to noise ratio scaling and density limit estimates in longitudinal magnetic recording. *IEEE Transactions on Magnetics*, 34(4 PART 1):1845–1847, 1998.

[91] T. W. McDaniel. Ultimate limits to thermally assisted magnetic recording. *Journal of Physics: Condensed Matter*, 17(7):R315–R332, 2005.

[92] Z. Liu, Y. Jiao, and R. H. Victora. Composite media for high density heat assisted magnetic recording. *Applied Physics Letters*, 108(23), 2016.

[93] S. Hernández, S. Granz, P. Krivosik P.-W. Huang, W. Eppler, T. Rausch, and E. Gage. Data rate effects on transition and remanence noise in a modeled heat-assisted magnetic recording system. *IEEE Transactions on Magnetics*, 53(11):1–4, 2017.

[94] S. Hernández, P.-L. Lu, S. Granz, P. Krivosik, P.-W. Huang, W. Eppler, T. Rausch, and E. Gage. Using ensemble waveform analysis to compare heat assisted magnetic recording characteristics of modeled and measured signals. *IEEE Transactions on Magnetics*, 53(2):1–6, 2017.

[95] J. Semmlow. *Signals and Systems for Bioengineers, Second Edition: A MATLAB-Based Introduction (Biomedical Engineering)*. Academic Press, 2nd edition, 2011.

[96] S. Hernández, Z. Liu, P. Jin, S. D. Granz, P. Krivosik, R. Venkataramani, W. Radich, T. Rausch, J. Dykes, and E. C. Gage. Geometrical scaling limits of heat-assisted magnetic recording. *IEEE Transactions on Magnetics*, 57(3):0–4, 2021.

[97] A. Lyberatos and K. Y. Guslienko. Thermal stability of the magnetization following thermomagnetic writing in perpendicular media. *Journal of Applied Physics*, 94(2):1119–1129, 2003.

[98] X. Wang, K. Gao, H. Zhou, A. Itagi, M. Seigler, and E. Gage. HAMR recording limitations and extendibility. *IEEE Transactions on Magnetics*, 49(2):686–692, 2013.

[99] T. Schrefl, H. Forster, D. Suess, W. Scholz, V. Tsiantos, and J. Fidler. *Micromagnetic Simulation of Switching Events*, pages 623–635. Springer Berlin Heidelberg, Berlin, Heidelberg, 2001.

[100] B. Purnama, I. Ismail, and S. Suharyana. Kajian Simulasi Mikromagnetik: Ketergantungan Medan Koersif dengan Besaran Intrinsik Nano-Dot Magnetik dengan Anisotropi Tegak Lurus. *Jurnal Fisika dan Aplikasinya*, 9(1):30, 2013.

[101] N. A. Herianto, F. S. Rondonuwu, and N. A. Wibowo. Damping dependence of reversal magnetic field on Co-based nano-ferromagnetic with thermal activation. *Smart Science*, 3(1):16–20, 2015.

[102] T. Kobayashi, Y. Nakatani, and Y. Fujiwara. Impact of Curie temperature variation on bit error rate in heat-assisted magnetic recording. *Journal of the Magnetics Society of Japan*, 43(4):70–78, 2019.

[103] T. A. Ostler, M. O. A. Ellis, D. Hinzke, and U. Nowak. Temperature-dependent ferromagnetic resonance via the Landau-Lifshitz-Bloch equation: Application to FePt. *Physical Review B*, 90(9):94402, 2014.

[104] P.-W. Huang, X. Chen, and R. H. Victora. Time dependence of magnetic anisotropy at finite temperature for homogeneous and composite media. *IEEE Transactions on Magnetics*, 48(11):3188–3191, 2012.

[105] A. J. Newell, W. Williams, and D. J. Dunlop. A generalization of the demagnetizing tensor for nonuniform magnetization. *Journal of Geophysical Research: Solid Earth*, 98(B6):9551–9555, 1993.